This manuscript is a preprint that has been submitted for publication in the Journal of Sedimentary Research. Please note that this manuscript has not yet undergone peer-review and is yet to be accepted for publication. Subsequent versions of this manuscript may have slighltly different content. If accepted, the final version of this manuscript will be available via the 'Peer-reviewed Publication DOI' link on the right-hand side of this webpage. Please feel free to contact the authors with any comments, we welcome feedback.

Running Head: SALT-INFLUENCED DEEP-WATER SUCCESSIONS

Title: INTERACTIONS OF DEEP-WATER GRAVITY FLOWS AND ACTIVE SALT TECTONICS

Authors: ZOË A. CUMBERPATCH[1*], IAN A. KANE[1], EUAN L. SOUTTER[1], DAVID M. HODGSON[2], CHRISTOPHER A-L. JACKSON[3], BEN A. KILHAMS[4] AND YOHANN POPRAWSKI[5]

Institutions:

[1]SedRESQ, School of Earth and Environmental Sciences, University of Manchester, Oxford Road, Manchester M13 9PL

[2] The Stratigraphy Group, School of Earth and Environment, University of Leeds, Leeds, LS2 9JT

[3] Basins Research Group (BRG), Department of Earth Science & Engineering, Imperial College, London, SW7 2BP

[4] A/S Norske Shell, 4056 Tanager, Stavanger, Norway

[5] Geologic Diffusion, 73 allée Jean Giono, 33100 Bordeaux, France

Email: zoe.cumberpatch@manchester.ac.uk

Keywords: Confined basin, submarine lobe, topography, salt diapir, halokinesis, deep-water sedimentology, Basque-Cantabrian Basin

ABSTRACT

Sediment gravity flow behaviour is influenced by seafloor topography associated with salt structures, which controls the depositional architecture of deep-water sedimentary systems. Typically, salt-influenced deep-water successions are poorly-imaged in seismic reflection data and exhumed systems are rare, hence the detailed sedimentology and stratigraphic architecture of these systems remains poorly understood.

The exhumed Triassic (Keuper) Bakio and Guernica salt bodies in the Basque-Cantabrian Basin, Spain were active during deep-water sedimentation. The salt diapirs grew reactively, then passively, during the Aptian-Albian, and are flanked by deep-water carbonate (Aptian-earliest Albian Urgonian Group) and siliciclastic (middle Albian-Cenomanian Black Flysch Group) successions. The study compares the deposition in two salt-influenced confined (Sollube basin) and partially-confined (Jata basin) minibasins by actively growing salt diapirs, comparable to salt-influenced minibasins in the subsurface. The presence of a well-exposed halokinetic sequence, beds that pinch out towards topography, soft sediment deformation, variable paleocurrents and intercalated mass transport deposits (MTDs) indicate that salt grew during deposition. Overall, the Black Flysch Group coarsens- and thickens-upwards in response to regional axial progradation, which is modulated by laterally-derived MTDs from halokinetic slopes. The variation in type and number of MTDs within the Sollube and Jata basins indicate the basins had different tectono-stratigraphic histories despite their proximity. In the Sollube basin, the routeing systems were confined between the two salt structures eventually depositing amalgamated sandstones in the basin's axis. Different facies and architectures are observed in the Jata basin due to partial confinement.

The findings show exposed minibasins are individualised and that facies vary both spatially and temporally in agreement with subsurface salt-influenced basins. Salt-related, active topography and

the degree of confinement are shown to be important modifiers of depositional systems, resulting in facies variability, remobilisation of deposits and 'channelisation' of flows. The findings are directly applicable to the exploration and development of subsurface energy reservoirs in salt basins globally, enabling better prediction of depositional architecture in areas where seismic imaging is challenging.

INTRODUCTION

The sedimentology and stratigraphic architecture of deep-water systems in unconfined basins (e.g., Johnson et al., 2001; Baas 2004; Hodgson 2009; Prélat et al. 2009; Hodgson et al. 2011; Spychala et al. 2017), and against static or relatively static, slopes (e.g., Kneller et al. 1991; Haughton 1994; McCaffrey and Kneller 2001; Sinclair and Tomasso 2002; Amy et al. 2004; Soutter et al. 2019) are well-established compared to those in basins influenced by active slopes (e.g., Hodgson and Haughton 2004; Cullen et al. 2019).

Seafloor topography is generated by a variety of geological processes, including relief above mass transport complexes (e.g., Ortiz-Karpf et al. 2015; 2016; Soutter et al. 2018; Cumberpatch et al. in review), syn-depositional tectonic deformation (e.g., Hodgson and Haughton 2004; Kane et al. 2010) and salt diapirism (Fig. 1) (e.g., Hodgson et al. 1992; Kane et al. 2012; Prather et al. 2012; Oluboyo et al. 2014). Salt-tectonic deformation influences over 120 basins globally (e.g., Hudec and Jackson 2007), including some of the world's largest petroleum-producing provinces (e.g., Booth et al. 2003; Oluboyo et al. 2014; Charles and Ryzhikov 2015; Rodriguez et al. 2018; 2020).

Subsurface studies have shown that salt structures deforming the seafloor exert substantial control on the location, pathway and architecture of lobe, channel-fill, levee and mass transport deposits (Fig. 1) (e.g., Mayall et al. 2006; 2010; Jones et al. 2012; Wu et al. 2020). Turbidity currents that were ponded, diverted, deflected and confined by salt structures (Fig. 1) are well-documented in the eastern Mediterranean (e.g., Clark and Cartwright 2009; 2011), offshore Angola (e.g., Gee and Gawthorpe 2006; 2007), the Gulf of Mexico (e.g., Booth et al. 2003) offshore Brazil (e.g., Rodriguez et al. 2018; 2020), the North Sea (e.g., Mannie et al. 2014) and the Precaspian Basin (e.g., Pichel and Jackson 2020). Successions of geneticallyrelated growth strata influenced by near-surface diapiric or extrusive salt form unconformity-bound packages of thinned and folded strata termed halokinetic sequences, which become composite when stacked (Giles and Rowan 2012). The geometry and stacking of composite sequences is dependent on the interplay between sediment accumulation rate and diapir rise rate, and two end-member stacking patterns are recognised, tapered (stacked wedge) or tabular (stacked hook) (Giles and Rowan 2012).

Typically, salt-influenced successions are poorly-imaged in seismic reflection data due to ray path distortion at the salt-sediment interface, steep stratigraphic dips, and deformation associated with salt rise (e.g., Davison et al. 2000; Jones and Davison, 2014). Due to these complexities, subsurface salt-influenced systems benefit from calibration with outcrop analogues (e.g., Lerche and Petersen 1995). Exposed examples are rare, largely due to dissolution of associated halites (Jackson and Hudec 2017). Exhumed systems typically contain shallow-marine (e.g., Giles and Lawton 2002; Giles and Rowan 2012) or non-marine (e.g., Banham and Mountney 2013a; b; 14; Ribes et al. 2015) strata. The Bakio diapir in the Basque-Cantabrian Basin (BCB), northern Spain, provides a rare exhumed example of deep-water strata deposited in a syn-halokinetic setting (Fig. 2, 3) (e.g., Lotze 1953; Robles et al. 1988; Rowan et al. 2012; Ferrer et al. 2014). The overburden displays well-exposed, unconformity-bounded sedimentary wedges that thin towards and upturn against the diapir, supporting the interpretation of syn-halokinetic growth strata (e.g., Poprawski et al. 2014; 2016).

Previous studies in the area have focussed on carbonate halokinetic sequences within the middle Albian overburden (e.g. Poprawski et al. 2014; 2016), hence the salt-influenced deep water succession remains poorly understood. This study aims to use large-scale outcrops exposed along the Bakio-Guernica coastline to study the bed-scale flow-topography interactions and deep-water facies and depositional architecture distribution in salt-controlled minibasins. The objectives of this study are to: 1) reappraise the stratigraphy of the study area using specific deep-water sub-environments; 2) document lateral and vertical changes in deep-water facies and architectures with variable amounts of salt-induced confinement; 3) document the evolution of coeval deep-water axial and MTD-rich lateral depositional systems, and 4) distinguish criteria for the recognition of halokinetically-influenced deep-water systems.

GEOLOGICAL SETTING

Evolution of the Basque-Cantabrian Basin (BCB)

The BCB is peri-cratonic rift basin in Northern Spain, inverted during the Campanian–Eocene western Pyrenean Orogeny (Fig. 2) (e.g., Gómez et al. 2002; Ferrer et al. 2008). The basin is located between the Iberian and Eurasian plates and is associated with hyper-extensive rifting and mantle exhumation during the opening of the North Atlantic and the Bay of Biscay (e.g., Van der Voo 1969; Brunet 1994; Jammes et al. 2009; DeFellipe et al. 2017; Teixell et al. 2018). The stratigraphy of the BCB is mainly Mesozoic to Cenozoic from a punctuated rift system that existed from Permian-Triassic to late Cretaceous times (Cámara 2017).

The Mesozoic evolution of the BCB beginning with the development of a rift system in the Permian-Triassic. During the Carnian-Norian, a thick sequence of mudstones, sabkha evaporites and carbonates accumulated (Keuper Group) (Geluk et al. 2018). The Jurassic to Early Cretaceous was characterised by limited subsidence and shallow water deposition (e.g., Martín-Chivelet et al. 2002; García-Mondéjar et al. 2004). Extensional thin-skinned tectonics, controlled by basement faulting, in the Early Cretaceous initiated reactive diapirism across the basin (e.g., Bodego and Agirrezabala 2013; Teixell et al. 2018). As rifting continued, the Lower Cretaceous succession preferentially accumulated over downthrown blocks, forming a differential load that triggered a transition into passive diapirism (e.g., Agirrezabala and García-Mondéjar 1989; Agirrezabala and López-Horgue 2017). During the Barremian-Albian the flanking minibasins were filled with c. 500 m of mixed carbonates and siliciclastics (García-Mondéjar 1990; 1996). Aptian-Middle Albian shallow-water carbonate platforms of Urgonian limestones (García-Mondéjar et al. 2004) formed on the footwalls of tilted normal fault blocks; these limestones pass abruptly into deeper-water marlstones and mudstones deposited in hanging-wall depocenters (Rosales and Pérez-García 2010). From the late Albian to early Cenomanian, subsidence combined with early Albian global sea level rise (e.g., Vail et al. 1977; Haq et al. 1987 Robles et al. 1988; Haq 2014) led to the development of siliciclastic turbidites and redeposited carbonates of the Black Flysch Group (BFG), which are the focus of this study.

As rifting waned, passive diapirs continued to grow at the paleo-seafloor due to minibasin subsidence (Zamora et al. 2017). During the Late Cretaceous to Early Paleogene, subsidence continued and calci-turbidites were deposited (e.g., Mathey 1987; Pujalte et al. 1994). The lower Paleocene to the Eocene records a gradual transition from mainly calcareous to siliciclastic deposition, with an increase in deposition of siliciclastic turbidites. This change is associated with erosion of the emerging Pyrenean mountain belt (e.g., Crimes 1973; Pujalte et al. 1998). Pyrenean NE-SW-orientated compression in Eocene to Oligocene times reactivated Mesozoic-Cenozoic normal faults (Ábalos 2016) and squeezed pre-existing diapirs (Pujalte et al. 1998).

The Bakio and Guernica salt bodies

The Bakio diapir is a NE-SW trending (~1 km by 4 km) salt wall of Keuper Group evaporites. Partial exposure of the salt wall occurs at Bakio beach; in other locations the evaporites are easily eroded, typically marked by topographic depressions and/or coastal embayments (e.g. the Guernica structure (Fig. 3a), located c. 9 km to the east). At Bakio beach, the Keuper Group consists of red clays, gypsum and carbonate, with occasional Triassic-aged tholeiitic ophitic inclusions (see Robles et al. 1988; Poprawski et al. 2014). From the middle Albian, the Bakio diapir grew rapidly and reactively in response to regional hyper-extension (Teixell et al. 2018). The diapir then grew passively during the late Albian due to sediment loading, at around 500 m Myr^{-1} (Poprawski et al. 2014).

The Guernica structure is poorly understood due to limited exposure, and hence is referred to as a 'salt structure' rather than a salt diapir like Bakio. The Guernica structure has previously been interpreted as a salt-cored anticline (Poprawski and Basile 2018). Vintage onshore seismic reflection data suggests that the Bakio and the Guernica structures are connected at depth (e.g., Robles et al. 1988; Poprawski and Basile 2018) (Fig. 4). The structures were close to the seafloor during the middle Albian creating highs that were capped by isolated carbonate platforms and influenced the deposition of the BFG (e.g., Vicente Bravo and Robles 1991a;b; Pujalte et al. 1986; Cámara 2017). Slope apron facies, deposited at the platform edge, and subsequent stratigraphy formed tapered halokinetic sequences against the west of the Bakio diapir (Fig. 4) (e.g. García-Mondéjar and Robador 1987; Soto et al. 2017).

Bakio Stratigraphy

Anisotropy of Magnetic Susceptibility studies in the Bakio-Guernica area demonstrate a minimal Pyrenean compressional overprint to the stratigraphy (Soto et al. 2017), as the structures acted as buttresses forming shadow areas protected from the compression. Hence the area is used to study syn-halokinetic deposition in the absence of a regional tectonic deformation overprint.

The Aptian-Middle Albian Urgonian stratigraphy (middle Albian Sequence 2 (*H. dentatus* Zone of Agirrezabala and López-Horgue 2017)) comprises the Gaztelugatxe, Bakio Marls, and Bakio Breccias formations (Fig. 3b). The Gaztelugatxe Formation (GZF) is a massive-brecciated limestone, interpreted as a karstified platform carbonate (e.g., García-Mondéjar and Robador 1987; Robles et al. 1988). The Bakio Marls Formation (BMF) (minimum 60 m thick; Poprawski et al. 2016) comprise thin-bedded calci-debrites deposited within a low-energy mud-dominated environment that were intermittently punctuated by catastrophic debris-flows sourced from local, carbonate-capped highs (e.g., García-Mondéjar and Robador 1987; Poprawski et al. 2014). The Bakio Breccias Formation (BBF) is up to 550 m thick and unconformably overlies the BMF (Fig. 3b, 4, and Table 1). The BBF is primarily composed of poorly-sorted, carbonate breccia beds (10's metres thick) (Table 1) (e.g., García-Mondéjar and Robador 1987; Poprawski et al. 2014; 2016) that are interpreted as earliest middle Albian, mass-failures from carbonate platforms (e.g. those developed on top of diapirs (Poprawski et al. 2014)). The abrupt change from carbonate-dominated to siliciclastic-dominated stratigraphy is associated with a middle Albian hiatus (López-Horgue et al. 2009).

The Urgonian section is overlain by the Upper Albian-Early Cenomanian BFG, which has been subdivided into a lower and upper unit (Fig. 3b). The Lower Black Flysch Group (LBF) corresponds to the Upper Albian Sequence 3 (*D. cristatum – M. inflatum* zones; Agirrezabala and López-Horgue 2017), including the Sollube, Punta de Bakio and Jata units (Poprawski et al. 2014). This group consists of thin-bedded siliciclastic turbidites, marls and MTDs and is interpreted as a submarine fan system (e.g., Robles et al. 1988; Vincente Bravo and Robles 1991; 1995; Poprawski et al. 2014). The Upper Black Flysch Group (UBF) corresponds to the Upper Albian–Cenomanian Sequence 4 (M. *fallax* zone; Agirrezabala and López-Horgue

2017), and the Cabo Matxitxako unit of Poprawski et al. (2014), which consists of thick-bedded, coarse-grained, siliciclastic turbidites deposited in a submarine fan system (Robles et al. 1988; 1989). Provenance studies indicate sourcing throughout BFG deposition from the northerly Landes Massif, a ~100 x 40 km granitic basement block, presently located ~10 km offshore in the Bay of Biscay (Fig. 2)) (e.g., García-Mondéjar 1996; Puelles et al. 2014).

METHODS AND DATA

The dataset comprises 28 sedimentary logs (totalling 821 m of stratigraphy) collected along the Bakio-Guernica coastline. The logs were collected at a 1:25 scale, with 1:10 scale used locally to capture additional detail. Halokinesis during BFG deposition (e.g., García-Mondéjar et al. 1996; Poprawski et al. 2014; 2016) generated syn-depositional basin floor relief and the development of sub-(mini)basins (e.g., Vicente Bravo and Robles 1991; 1995; Agirrezabala 1996). As such, correlating stratal surfaces within and between depocenters is difficult and unmanned aerial vehicle (UAV) photography was used to aid stratigraphic correlations (Hodgetts 2013). Paleocurrent, bedding and structural data were collected to determine influence of syn-depositional basin floor relief and to quality-control the pre-existing geological map of Poprawski et al. (2014; 2016). Paleocurrent readings were taken where sedimentary structures were clear enough to permit unambiguous data collection. Sparse biostratigraphic data (Agirrezabala and López-Horgue 2017) hinders correlation across the structures; hence we refer to the LBF and UBF only, to avoid further subdivisions based on geographic location (e.g., Robles et al. 1988; Vincente-Bravo and Robles 1991; 1995; Poprawski et al. 2014).

Basin subdivision

To aid comparison, the study area has been divided into two depocenters; the Jata and Sollube basins (Fig. 3, 4), analogous to subsurface minibasins–relatively small (5-30 km) syn-kinematic depocenters subsiding into thick salt (Hudec and Jackson 2007; Jackson and Hudec 2017). The Jata basin is confined to the east by the Bakio diapir. The Sollube basin is confined on both its western and eastern sides by the Bakio and Guernica structures, respectively (Fig. 3), and hence is more confined than the Jata basin (e.g., Winker 1996; Prather et al. 1998; Sinclair and Tomasso 2002).

LITHOFACIES

This study primarily focusses on the facies variability within the siliciclastic BFG. A description and discussion of the carbonate facies of the BMF and BBF is provided in Poprawski et al. (2016). Here the carbonate facies are tabulated for reference in Table 1 and assigned a gravity flow-focussed interpretation. The BFG lithofacies presented in Table 2 and in Figure 5 represent 'event beds' and are classified based on outcrop observations. 'Mud' is used here as a general term, for mixtures of clay, silt and organic fragments. Where individual facies are heterogeneous, multiple photographs are shown to illustrate this lithological and sedimentological variability (Fig. 5).

INTERPRETATION OF DEPOSITIONAL ELEMENTS

Facies associations (Table 3, Fig. 6) and architectures (Table 4, Fig. 7) combine to support depositional element interpretations. Facies associations are interpreted based on dominant lithofacies (Table 2, Fig. 5) and use lobe (Prélat et al. 2009; Spychala et al. 2017) and channel-levee (Kane and Hodgson 2011; Hubbard et al. 2014) nomenclature that best fit field observations. In agreement with recent work, we use MTD to describe deposits from varied subaqueous mass flows, including a mixture of slides, slumps and debris-flows (e.g., Nardin et al. 1979; Posamentier and Kola 2003; Doughty-Jones et al. 2019; Wu et al. 2020). Facies associations and geometries are described separately, because architecture alone is not diagnostic of the depositional sub-environment, and multiple facies associations can form a similar architecture.

STRATIGRAPHIC EVOLUTION

Extensive exposures permit detailed lithostratigraphic analysis (Fig. 3, 8, 9, 10) allowing investigation of the role of salt-induced relief on depositional patterns (Fig. 11, 12, 13). The following sections describe the exposures from oldest to youngest, first focussing on the flanks of the Sollube and Jata basins (Gaztelugatxe Island and Bakio West Bay respectively) and then the axis of the Sollube basin (Cabo Matxitxako).

Gaztelugatxe Island

The cliff sections to the south of Gaztelugatxe Island provides a semi-continuous section through 120 metres of the BFG, 2 km north-east of the exposed Bakio diapir, and ~9 km north-west of the Guernica structure. The stratigraphy is subdivided into five lithostratigraphic units (GX 1-5).

Description

GX1 is 8 m thick and consists of bioturbated mudstones, calci-debrites, calci-turbidites, thin-bedded turbidites and mud-rich debrites. It shows an overall coarsening- and thickening-upwards from cm to metre-scale interbeds of each facies. GX2 is 10 m thick and dominated by carbonate-clastic debrites, with angular clasts of the Gaztelugatxe Limestone, up to 1 m in diameter. GX2 pinches out downslope forming a triangular geometry (Table 4, Fig. 7E). GX3, has a minimum thickness of 42 m, onlaps GX2 and is recognised as the first purely siliciclastic succession; comprising thin-medium bedded turbidites, debrites, hybrid beds and bioturbated mudstones. GX4 has a minimum thickness of 9 m and its base is marked by a metre-thick slump, overlain by interbeds (cm-10's cm-scale) of turbidites, debrites, MTDs, hybrid beds and mudstones.

GX5 is identified on the western side of Cabo Matxitxako (Fig. 8), having a minimum thickness of 30 m. There is approximately 400 metres of missing stratigraphy between GX4 and 5 (Robles et al. 1988), but GX5 is projected to lie stratigraphically above GX4. GX5 comprises predominantly amalgamated medium- to high-density turbidites showing evidence of soft sediment deformation.

Interpretation

The presence of siliciclastic and calci-turbidite deposits and MTDs in GX1 (Fig. 8) suggests a transition from the upper BBF to the LBF (Fig. 12C) (Poprawski et al. 2014; 2016). The carbonate deposits could have been remobilised from previous BBF deposits or remnant carbonate highs (Poprawski et al. 2014; 2016). GX2 represents a period of increased mass failure, which is interpreted to be halokinetically-driven due to the lentil-shape and diapir-centric distribution of these limestone breccias (Table 4, Fig. 7E) (e.g., McBride et al. 1974; Hunnicutt 1998; Giles and Lawton 2002). The thin-bedded nature and presence of hybrid beds in GX3 suggests early BFG deposition in a proximal lobe fringe environment (e.g., Spychala et al. 2017; Soutter et al. 2019). Thin-bedded debrites are interpreted to be delivered axially based on their association with thin-bedded turbidites that show regional paleocurrents. Thick-bedded, chaotic clast-rich units are interpreted to be halokinetically-driven based on variable, slump axis paleocurrent readings (Poprawski et al. 2014).

At the base of GX4, a metre-scale MTD overlies 30 m of missing section (Fig. 8), which given the low-lying geomorphology is likely mud-rich. The overlying turbidites and MTDs suggest deposition in a lobe off-axis setting (e.g., Prélat et al. 2009; Spychala et al. 2017) where the seafloor was, at least periodically, unstable (Fig. 12E). Metre-thick beds that stack into 30 m-thick packages suggest that GX 5 represents deposition in the axis of a lobe complex (Fig. 12F) (e.g., Prélat et al. 2009; Soutter et al. 2019). The absence of debrites (Fig. 8) suggests minimal halokinetic influence, either due to diapir inactivity or sediment accumulation (due to uplift and erosion from the Landes Massif (e.g., Agirrezabala 1996)) outpacing the rate of seafloor deformation. The presence of amalgamated, laterally extensive medium- and high-density turbidites in GX5 support deposition in a channel-lobe transition zone (e.g., Vincente Bravo and Robles 1991; 1995) or lobe axis setting.

Bakio West Bay

The coastal cliff section at Bakio West Bay (Fig. 9) exposes c. 150 m of the BFG above its basal contact with the BBF (Robles et al. 1988), ~1 km west of the Bakio diapir. This section is divided lithostratigraphically into 3 units (BW1-3), and is further divided by halokinetically-driven unconformities (e.g. BW 3a, b, c) (Fig. 9) (Poprawski et al. 2014).

Description

BW1 is 6 metres thick, consists of calci- and siliciclastic- turbidites, debrites and mudstones, and is overlain by BW2 across an angular unconformity (U2; Poprawski et al. 2014) (Fig. 9A). BW2 is principally siliciclastic, comprising predominantly turbidites, with minor debrites and mudstones. A 10 metre thick package of fine sand- to pebble-grade turbidites with lenticular geometries and scoured-amalgamated bases is observed to overlie a 2 metre thick MTD (Fig. 9A). BW3 consists of interbedded metre-scale siliciclastic turbidites and MTDs (Fig. 9B). U5 and 6 are intra-BW3, and thus BW3 is subdivided into three sub-units (BW3a, b, and c).

At the base of BW3a, BW3b and BW3c, 1-12 metre thick MTDs with variable thickness across the exposure overlies an angular unconformity (Fig. 9). Grain size varies from medium sand to boulder and clasts vary from rounded to angular. A more diverse range of clast rock types than elsewhere in the study area are observed, including limestone, sandstone, mudstone, organics, heterolithics, siderite, mafic material, granite and siderite (Table 3). An undulose contact exists between the MTDs and the 2-4 metre-thick amalgamated turbidites which overly them (Fig. 9). These coarse-grained (medium sand- pebble grade) turbidites are lenticular in geometry, can be divided into metre-scale fining-upwards successions and contain weak inclined stratification (Fig. 9).

Interpretation

The angular unconformities are interpreted to be related to salt diapir movements, and are interpreted as part of a tapered halokinetic sequence (e.g., Giles and Rowan 2012; Poprawski et al. 2014). Unit BW1 marks the transition from BBF to BFG, and in interpreted as representing deposition at the base of slope of the carbonate platform, which was growing on the Bakio diapir (Fig. 12D) (Poprawski et al. 2014). Coarse-grained sandstones with lenticular geometries, scoured bases and normal grading, such as those observed in BW2, indicate deposition in a channelised or scoured setting (Fig. 6F, 9,12E) (e.g., Hubbard et al. 2014; Hofstra et al. 2015). The MTDs capping unconformities could be halokinetically-derived or related to channel margin collapse induced by diapir movement (Rodriguez et al. 2020). The wide range of clast rock types in these MTDs suggest that they are dissimilar to other halokinetically-derived MTDs and could indicate a different set of mass flows sourced up dip of the depositional system (Fig. 9C) (e.g. Doughty-Jones et al. 2019; Wu et al. 2020).

The deepest point of each lenticular geometry in BW3 appears to step eastward towards the Bakio diapir (Fig. 6F, 7A); this could indicate lateral accretion deposits from a meandering submarine channel (e.g., Peakall et al. 2007; Kane et al. 2010; Janocko et al. 2013). The concave-upward geometry of the turbidites and the undulose contact with the MTD below (Fig. 6F, 7B, 9), could represent channel- or scour-fills influenced by previous debrite topography (e.g., Cronin et al. 1998; Jackson and Johnson 2009; Kneller et al. 2016). The thick-beds, concave-upward geometry, and coarse grain size suggests these deposits are channel-fills rather than scour-fills (e.g., Hubbard et al. 2008; Romans et al. 2011; McArthur et al. 2020).

The repeated facies change between pebbly chaotic debrites and channelised turbidites is interpreted to represent periods of rapid diapir growth, evidenced by debrites overlying halokinetic unconformities (e.g., Giles and Rowan 2012). This is suggested to be followed by periods of relative diapir quiescence, which permit submarine channels to infill debrite topography, and migrate around the diapir due to reduced seafloor topography (e.g., Kane et al. 2012).

Cabo Matxitxako

Cabo Matxitxako provides an extensive section (c. 600 m) through the BFG. In this locality, we subdivide the group into eight lithostratigraphic units (CM1-8) (Fig. 10). There is c. 500 m of missing section between Cabo Matxitxako North and South Beach (Fig. 3). Cabo Matxitxako is located within the Sollube basin, ~4.5 km north-east and ~5 km north-west of the Bakio and Guernica salt structures respectively.

Description

CM1 is a 100 m thick package of mudstones, with minor thin-medium bedded siliciclastic turbidites and debrites. CM2 is 60 m thick and is dominated by metre-scale debrites with subordinate thin- to medium-bedded turbidites, hybrid beds, and mudstones (Fig. 10). Slump axes within MTDS, where present, indicate a range of paleoflow directions (forming two clusters: 80°-160° and 280°-320° (Fig. 3)). CM3 is 50 m thick and contains metre-thick packages of stacked medium-thick bedded, dewatered turbidites and metre-10's metre thick debrites containing rafts of thin-bedded turbidites. Two beds of granular sandstone (27 and 19 cm thick) with lenticular geometries are observed at the top of CM3. CM4 is 32 m thick, is separated from CM3 because it is debrite-poor and mostly comprises thick-bedded, amalgamated high-density turbidites that stack into 3-6 metre packages. CM5 is 124 m thick and consists of roughly equal proportions of 1-3 metre-thick, amalgamated turbidites, which are normally graded on a bed-scale, and metre-scale MTDs, that occur every 2-10 m, and contain rafts of thin-bedded turbidites. CM6 has a minimum thickness of 18 m, is observed at the northern part of the South Beach, and is composed of 1-3 m debrites and 1-80 cm turbidites and mudstones (Fig. 3, 10). CM7 has a minimum thickness of 38 m, similar to CM6, however the units are separated by c. 500 m of missing stratigraphy, much of which is assumed to be removed due to Pyrenean deformation and recent landslides (Vicente Bravo and Robles, 1995), so have been separated. CM8 is 40 m thick and consists of predominantly metre-scale, normally-graded thick-bedded turbidites with erosional bases, cross-stratification, amalgamation, mud-clasts and dewatering structures common throughout (Fig. 10).

Interpretation

The Cabo Matxitxako succession (Fig. 10) suggests a broadly basinward-shifting (i.e. progradational) system from CM1-4, followed by a slight back-step (i.e. retrogradational) or lateral shift in CM5-7, and a further basinward shift in CM8 (Fig. 12).

MTDs with clasts of thin- and medium-bedded stratigraphy are present throughout CM2, 3, 5, 6 and 7 suggesting the seafloor was periodically highly unstable, possibly due to relatively high rates of diapir rise and related seafloor deformation. CM1 is dominated by background suspension fallout and dilute low-density turbidites deposits in a lobe complex distal fringe setting (Fig. 12D). CM2 represents higher energy, more proximal lobe conditions compared to CM1, based on facies, hybrid beds, geometry, stacking patterns and thickness and is interpreted as proximal lobe fringe deposition (e.g., Spychala at al. 2017). The depositional sub-environment of CM3 is interpreted as an off-axis lobe complex, based on facies and bed thicknesses, with small distributive channel-fills, evidenced from lenticular granular sandstones (e.g., Normark et al. 1979; Deptuck and Sylvester 2017). CM4 is dominated by stacked, amalgamated, high-density turbidites (Fig. 10) and is interpreted to represent deposition in the axis of a lobe complex (Fig. 12F) (e.g., Prélat et al. 2009; Spychala et al. 2017). CM5 contains similar facies distributions to CM3, so is interpreted to represent lobe complex off-axis deposition with some distributive channel-fills (e.g., Normark et al. 1979; Deptuck and Sylvester 2017). Debrite dominance in CM6 and CM7 suggest remobilisation due to diapir growth throughout deposition (Fig. 12F). These deposits are interpreted to represent proximal fringe – lobe-off axis deposition (Spychala et al. 2017), which is highly modulated by halokinetic MTDs. The coarse grain-size, cross-stratification, thick-beds, and lack of debrites and mudstones (Fig. 6E, 10), suggests that CM8 was deposited in a channel-lobe transition zone (Vincente Bravo and Robles 1995; Brooks et al. 2018). This unit shows little evidence for active topography, suggesting that the sedimentation rate had increased with respect to the diapir rise rate, possibly associated with uplift of the Landes Massif (Rat 1988; Martín-Chivelet et al. 2002), or salt source layer welding. Any remaining seafloor topography was filled by CM8 (Fig. 12G).

Stratigraphic correlation

The BW, GX and CM lithostratigraphic units show different depositional systems despite their close proximity. Combined with poor biostratigraphic calibration (Agirrezabala and López-Horgue 2017), stratigraphic correlations between the areas are challenging. Using lithostratigraphy, BW1 is correlated to GX1-2, BW2-3 are correlated to GX3-4 and CM1-7, whereas GX5 is correlated to CM8 (Fig. 8, 9, 10).

EVIDENCE FOR SEAFLOOR TOPOGRAPHY

There is widespread sedimentological evidence for seafloor topography during deposition of the BFG, which as we discuss below reflects the interplay between active salt growth (salt-induced) and depositional stacking (debrite-/MTD-induced) controlling the available accommodation.

Ripple cross-lamination, cross-stratification and sole marks indicate a regional south-westerly paleoflow direction (Fig. 11). This direction is consistent with a northerly source for the BFG, supporting the Landes Massif as a potential regional source area (e.g., Rat 1988; Robles et al. 1988; Ferrer et al. 2008; Puelles et al. 2014). At Cabo Matxiatxako, a secondary westerly-paleoflow orientation (Fig. 11A) is comparable to findings by Robles et al. (1988), who suggest this reflects the passage of gravity-flows that spilled across the Guernica structure into the Sollube basin. Therefore palaeocurrent data (Fig. 11A) suggests modulation of a regional (primarily south-trending) palaeoflow by salt-induced topography (west-trending flows off east-facing slopes) (Fig. 12). Analogously, a west-south-westerly paleoflow observed at Bakio Bay West (Fig. 3) may reflect the passage of gravity-flows that spilled from the Sollube basin, across the Bakio structure into the Jata basin. This west-south-westerly paleoflow could alternatively represent the westward deflection of regional paleoflow around the Bakio diapir.

Ripple lamination in opposing directions is common within individual thin-bedded turbidites (Fig. 11B). Such features have been attributed to flow reflection or deflection from seafloor topography (e.g., Kneller et al. 1991; McCaffrey and Kneller 2001; Barr et al. 2004; Hodgson and Haughton 2004). Moreover, hybrid beds seen outside the frontal fringe (Fig. 5L, 5M, 8, 9, 10) indicate that topography has influenced a transformation of flow from turbulent to laminar (Fig. 14) (e.g., Barker et al. 2008; Soutter et al. 2019).

Turbidites that pinch-out up depositional slope (Fig. 7C) reflect the thinning towards topography (e.g., Ericson et al. 1952; Gorsline and Emery 1959) as the low-density part of the turbidity current ran up the topography further than the high density component (e.g., Al-Ja'aidi 2000; Bakke et al. 2013). Hence, thicker sandstones are more likely to be confined to localised salt withdrawal minibasins (Fig. 12, 13, 14), whereas thinner sandstones may drape halokinetically-influenced topography (Fig. 12, 13, 14) (e.g., Straub et al. 2008; Soutter et al. 2019). Based on a bed-scale thinning rate of 10 cm/m at Cabo Matxitxako (Fig. 3, 10), we calculate the slope angle to be 2-3° (Fig. 7C). Due to the distance (~5km) from the present day Bakio diapir, it is unlikely that this slope is related to primary diapir growth, but rather caused by localised salt withdrawal or welding from the salt source layer at depth.

Multiple palaeoflow directions, hybrid beds, and abrupt pinch-out of beds could verify the presence of (static) topography. However, the number of MTDs intercalated with lobes, and the tapered composite halokinetic sequence observed at Bakio West Bay (Fig. 11D) indicate this topography and salt growth was active at the time of deposition (e.g., Counts et al. 2019).

Mass transport deposits

Description

MTDs account for 23% of stratigraphy across all measured sections, with an average thickness of 111 cm, assuming that all MTDs (Table 1, Fig. 5K, 7D) are derived from diapir slopes and all turbidites are derived from far-field. A 1:4 ratio of halokinetically- to axially-derived deposition exists across the study area, suggesting that locally, extra stratigraphy may be present in salt-confined basins compared to unconfined settings; therefore interpretation of stacking patterns may be challenging due to halokinetic modulation of allocyclic signals. MTDs on the flank of the Jata basin have an average thickness of 140 cm, compared to 119 cm and 73 cm in the axis and flank of the Sollube basin respectively. 31% of measured stratigraphy on the flank of the Jata basin comprises MTDs compared to 18% and 22% in the axis and flank of the Sollube basin respectively. MTD composition shows siliciclastic dominance in the axis of the Sollube basin, MTDs with carbonate clasts or matrix become more common on the flank of the Sollube basin and are dominant on the flank of the Jata basin (Fig. 8, 9, 10) in agreement with halokinetic sequence models (Giles and Rowan 2012).

Limestone clasts of similar composition within MTDs on both the Jata and Sollube flank support the presence of a carbonate platform growing on top of the Bakio diapir (e.g., García-Mondéjar and Robador 1987; Poprawski et al. 2014; 2016), indicating these MTDs are related to local diapir failures.
Isolated limestone megaclasts (Fig. 9F, 11E, 11F) derived from the Gaztelugatxe Limestone could be out-runner blocks (e.g., De Blasio et al. 2006; Soutter et al. 2018) or fractured blocks of platform limestone that have toppled off during diapiric growth (e.g., Alves et al. 2002; 2003; Martín-Martín et al. 2016). Younger deposits progressively onlap these limestone clasts (Fig. 11E, 11F) showing subsequent turbidity currents have interacted with this additional seafloor topography (e.g., Kilhams et al. 2012; 2015 Olafiranye et al. 2013; 2015).

Interpretation

MTDs could either be sourced from collapse on top of the diapir or its flanks, or from failures of the shelf-edge and/or slope (e.g., Doughty-Jones et al. 2019; Rodriguez et al. 2020; Wu et al. 2020). The presence of more MTDs in the basal active part of the Sollube basin (Fig. 8, 9, 10, 13) compared to the upper passive part of the basin fill (Fig. 10) suggests mass failures are more common during initial development of salt-confined depocenters in agreement with Wu et al. (2020). The difference in MTD proportions between the

Jata and Sollube basins ratify that they developed, at least partially, as separate depocenters influenced by different controls (Fig. 8, 9, 10).

The presence of complicated variations in thickness, clast type and MTD style across the study area suggests that mass flows are likely to be both locally-derived (from the salt structures) and regionally-derived (from the shelf), and therefore MTDs are likely to be both allocyclically- and halokinetically-controlled (e.g., Moscardelli and Wood 2008; Doughty-Jones et al. 2019; Wu et al. 2020).

DISCUSSION

The discussion initially focusses on the Sollube basin, then compares the Sollube and Jata basins, before comparing our observations to similar depocenters developed in other salt-influenced basins.

Sollube Basin architecture

A 2D cross section through the Sollube basin is similar in size and geometry to subsurface minibasins (Fig. 13) (e.g., Pratson and Ryan 1994; Booth et al. 2003; Madof et al. 2009). Therefore this rare, exhumed example of a halokinetically-influenced deep-water succession provides an excellent exposure of fine-scale minibasin depositional architecture, providing an analogue for subsurface minibasins.

Facies and architecture distribution

The Sollube basin is 8 km wide and confined to the east and west by the Guernica and Bakio structures respectively (Fig. 4) (e.g., Robles et al. 1998; Poprawski and Basile 2018). Repeated stratigraphy and facies distribution on either side of Cabo Matxitxako, the change in bedding angle between the LBF and UBF, and sedimentological evidence for syn-depositional topography support the presence of a broadly symmetrical basin confined by the Bakio and Guernica structures.

Early stratigraphy within the siliciclastic fill of the Sollube basin is dominated by thin-bedded sandstones, with localised MTDs on the flanks (Fig. 8, 10, 13). As the basin developed, subsequent thicker-bedded sandstones representing channel-fills and lobes were deposited in topographic lows (basin axis), consistent with subsurface analogues (e.g., Booth et al. 2003; Madof et al. 2009; Mayall et al. 2010; Doughty-Jones et al. 2017) and numerical models (e.g., Sylvester et al. 2015; Wang et al. 2017). Towards the flanks, the lower density parts of the flows responsible for the thick-bedded sandstones, may run up topography, depositing thinly-bedded sandstones. Therefore, allocyclically controlled, axially-derived, and often the thickest stratigraphy is observed in the axis of the minibasin. Halokinetically-controlled (e.g. MTDs) or -influenced (e.g. thickness variations) stratigraphy occurs towards the basin margins. These interpretations are consistent with subsurface studies (e.g., Doughty-Jones et al. 2017; Rodriguez et al. 2020; Wu et al. 2020).

Oluboyo et al. (2014) suggest a fundamental control on the type of confinement developed is the incidence angle between the strike of the salt structure and the palaeoflow direction. 'Fill-and-spill' architecture is observed in deep-water environments where topographic highs strike perpendicular to the gravity-flow direction (i.e. at a high incidence angle) (e.g., Piper and Normark 1983; Prather et al. 2012; Soutter et al. 2019). This study documents a rare example of an exhumed halokinetically-influenced deep-water succession where paleoflow is at a low incidence angle to structural strike (i.e. oblique-parallel). In such scenarios, spill between basins is rare, and sedimentary systems are deflected to run broadly parallel to salt-walls within minibasins for several kilometres (Fig. 13, 14, 15) (e.g., Oluboyo et al. 2014). The four-fold model of a confined basin-fill (Sinclair and Tomasso 2002) is not appropriate where paleoflow is oblique or parallel to salt structures, and there is a down-dip exit (i.e. not confined in all directions) . Our study indicates that the dominant style of interaction between gravity flows and topography is lateral confinement, with channels and lobes in the Sollube basin being thickest in the axis and elongated parallel to salt-controlled basin margins (e.g., Booth et al. 2003; Wu et al. 2020). The presence of MTDs is somewhat overlooked in both the confinement model proposed by Oluboyo et al. (2014), and the earlier 'fill-and-spill' model (e.g., Winker 1996; Prather et al. 1998; Sinclair and Tomasso 2002). MTDs sourced from either up-dip (i.e. extra-basinal; detached) or from local mass failures (i.e. intra-basinal; attached) related to growing salt structures, can generate additional syn-depositional relief and flow confinement (Fig. 14) (e.g., Moscardelli and Wood 2008; Rodriguez et al. 2020).

The hierarchical scheme for classifying deep-water systems developed in the Karoo basin (Prélat et al. 2009) is widely accepted, but must be used with caution, or be adapted for confined systems (e.g., Prélat et al. 2010; Etienne et al. 2012; Marini et al. 2015) . Prélat et al. (2010) recognises that width: thickness ratios and areal extent: thickness ratios will be different for confined and unconfined systems. Width: thickness is 100:1 in selected subsurface confined settings, compared to 1000:1 in unconfined settings and areal extent: maximum thickness is 30 times greater in unconfined systems compared to confined systems (Prélat et al. 2010). All examples used in Prélat et al. (2010) are from settings where palaeoflow is perpendicular (high angle) to topographic strike.

In terms of areal extent, stratigraphy in the Sollube basin (~8 km wide) would be best classified as a lobe element (~5 km wide) using the Prélat et al. (2009) framework. However, in terms of thickness each lithostratigraphic unit observed at Cabo Matxitxako (18-124 m thick) (Fig. 10) would be classified as a lobe complex (~50 m thick). The width: thickness ratio of lobes within the Sollube basin is ~160:1 (taking an mid-point thickness of 53 m), in agreement with Prélat et al. (2010). This suggests similar basic geometries for confined lobes regardless of incidence angle between palaeoflow and topographic-strike.

Confined lobe complexes are predicted to have smaller areal extents because radial spreading is minimal due to topographic confinement (e.g., Marini et al. 2015; Soutter et al. 2019). The ratio of axis to fringe deposition is likely to be increased in confined settings where flows stay turbulent for longer, flow deceleration is limited and development of a wide fringe is hindered due to presence of topography (e.g., Etienne et al. 2012; Soutter et al. 2019). The presence of thicker axial deposits due to confinement by topography, and less space for lateral lobe switching to occur, may make axis definition easier in confined setting, however this may change through time if topography is healed and depositional systems become less confined (e.g. Marini et al. 2015).

This study supports recent work (e.g., Oluboyo et al. 2014; Rodgriguez et al. 2020) which suggest that elongate systems are common adjacent to topography, on all scales. This is in contrast with the roughly equant geometries predicted in unconfined systems (Prélat et al. 2009).

Multi-scalar analysis suggests all hierarchical elements would have greater lengths than widths, and lesser areal extents and greater thicknesses (lower aspect ratios) than unconfined settings when deposited adjacent to oblique-parallel topography (e.g., Booth et al. 2003; Oluboyo et al. 2014; Rodriguez et al. 2020).

Axial system development

The overall upward-thickening of beds and coarsening of grainsize from south to north at Cabo Matxitxako (Fig. 10) is associated with a transition in depositional environment from lobe distal fringe to channel-lobe transition zone (Fig. 10, 12). Coarsening- and thickening-upwards elsewhere is widely interpreted to represent progradation (e.g., Mutti 1974; Macdonald et al. 2011; Kane and Pontén 2012); however, they could also represent (a component of) lateral stacking of lobes (e.g., Prélat and Hodgson 2013).

Throughout the Pyrenean, the BFG is interpreted to be controlled by allocyclic progradation (e.g., Robles et al. 1988; Agirrezabala and Bodego 2005), driven by increases in sediment supply following the uplift of the Landes Massif (e.g., García-Mondéjar et al. 1996; Martín-Chivelet et al. 2002; Puelles et al. 2014) and/or increased flow efficiency from confinement (Hodgson et al. 2016). This regional progradation, along with our field observations, provides compelling evidence that on a lobe-to-lobe complex scale, the stratigraphic architecture of the study area is primarily controlled by system progradation. Lateral switching may be reduced due to confining topography decreasing the amount of space available for switching to take place (e.g., Mayall et al. 2010; Oluboyo et al. 2014).

By definition, only two lobe elements would be able to fit laterally within the Sollube basin during LBF deposition (Prélat et al. 2009), suggesting that due to confinement lateral stacking in our study area is only feasible at the bed-scale (Marini et al. 2015). The apparent retrogradation observed between CM5-7 could be a result of bed-lobe scale lateral shifting and compensational stacking modulating an otherwise progradational lobe complex (e.g., Gervais et al. 2006; Pickering and Bayliss 2009; Etienne et al. 2012; Morris et al. 2014).

The lack of space for lateral stacking to occur suggests that lateral topography reduces flow loss to overspill and deceleration, and therefore the system remains turbulent for longer. This causes a basinward shift in deposition effectively acting to magnify the effects of progradation (e.g., Kneller and McCaffrey 1999; Talling et al. 2012; Patacci et al. 2014). This concept accounts for numerous, thick, high-density turbidites (LBF) within the axis of the Sollube basin; formed by gravity flows that were funnelled between the two structures (Fig. 13, 14C, 14F, 15) (e.g., Scott et al. 2010; Oluboyo et al. 2014; Counts and Amos 2016).

Using observations from Bakio, a range of stacking patterns may form during progradation of a deep-water system in an unconfined, partially confined and dual-confined setting (Fig. 15). Unconfined fans have a higher aspect ratio, surface area and avulsion angle than confined systems as the ability of the flows to spread radially was not restricted by topography (Prélat et al. 2009; Spychala et al. 2017). Where only one lateral confinement is present deposits may be asymmetrical, as flows are confined by diapir topography in one direction but able to spread radially away from it, as is seen in the deposits of the Jata basin (Fig. 9) (Soutter et al. in review).
In settings with lateral confinement, deep-water systems are elongated axially, sub-parallel with bounding relief (Fig. 13, 14, 15) (e.g. Oluboyo et al. 2014; Soutter et al. in review). Funnelling of axial gravity flows, and therefore bed amalgamation , is interpreted to be more enhanced where two salt structures are present, resulting in thicker deposits, but areally smaller depositional architectures than unconfined settings (e.g., Kneller and McCaffrey 1999; Patacci et al. 2014; Soutter et al. in review).

Diapir growth is not continuous through time, and phases of rapid growth (e.g., Fig. 5; t2-t3, t5-t6) and quiescence (e.g., Fig. 15; t1, t4) (Hudec and Jackson 2007) cause destabilisation and remobilisation of the diapir roof, overburden or flank deposits (Fig. 8, 9, 10). This can drive re-routing of subsequent systems to avoid failure topography, potentially resulting in lateral or compensational stacking (e.g., Kane et al. 2012; Doughty-Jones et al. 2017; 2019; Rodriguez et al. 2018; 2020) (Fig. 9, 12F, 14E, 15). In fully confined settings, there is no space for rerouting and lateral MTDs could be amalgamated with, or eroded away by, flows depositing axial turbidity currents (Fig. 7C, 10, 12, 13, 14, 15).

Active or Passive topography

The geometry and number of the MTDs, and thin-bedded sandstones that pinchout, is controlled by the presence of actively growing topography during LBF deposition. The absence of MTDs in the UBF suggest that diapir growth ceased following uplift of the Landes Massif (e.g., García-Mondéjar et al. 1996; Puelles et al. 2014).

Following the cessation of diapir growth we infer an underfilled syncline remained due to remnant topography of the buried Bakio and Guernica structures, which appears to have constrained UBF deposition until it was filled (Fig. 3, 12G, 13). The LBF represents early stage 'active' deposition, perhaps comparable to syn-kinematic megasequences observed in the subsurface, whereas the UBF represents late stage 'passive' deposition, infilling antecedent topography, comparable to post-kinematic megasequences observed in the subsurface (e.g., Pratson and Ryan 1994; Warren 1999; 2006; Jackson and Hudec 2017). UBF deposits are less confined due to the lesser influence of salt-influenced topography during deposition, and therefore through time may evolve represent semi- or un-confined deep water systems, more capable of lateral stacking (e.g. Marini et al. 2015).

Comparison of Sollube and Jata basins

Different facies distributions on either side of the Bakio diapir varied during LBF times according to the degree of confinement and distance from diapir crest (Fig. 12, 13). Within the Bakio Breccia Formation, clast- and matrix-supported breccias are common in the Sollube and Jata basins respectively (Poprawski et al. 2016) suggesting minibasin individualisation is long-lived. The lack of confining topography to the west of the Jata basin may have caused flows to dilute, resulting in muddier, more-matrix rich breccias (e.g., Hampton 1972; Sohn et al. 2002; Baas et al. 2009).

LBF stratigraphy in the Jata basin thin towards the Bakio diapir (Fig. 11D) showing more evidence for topography than comparable strata in the Sollube basin, supporting the idea that halokinetic deformation is greatest closest to salt structures (e.g., Giles and Lawton 2002; Giles and Rowan 2012). Richness in limestone clasts in LBF MTDs in the Jata Basin (Fig. 9C, Table 3) could indicate asymmetric build up and failure of the carbonate platform above the Bakio diapir, preferentially filling the Jata basin (e.g., Rosales and Pérez-García 2010; Li et al. 2012). The presence of a multitude of different clast types in the Jata basin (Table 3; Fig. 9) could suggest different depositional routing relative to the Sollube basin, possibly due to the presence of salt topography causing different source areas to be tapped (e.g., Mayall et al. 2010; Oluboyo et al. 2014).

Another key difference is the architecture of thick-bedded sandstones. In the Jata basin, individual depositional elements are often concave-up, thinner, and show more tractional structures (e.g. ripple and planar lamination) than those in the Sollube basin. Where lateral confinement occurs along one margin sandstones could represent sinuous low-relief channel-fills that ran sub-parallel to topography (e.g., Mayall et al. 2010; Oluboyo et al. 2014). They are able to spread laterally and migrate because are only partially unconfined (e.g., Mayall et al. 2010; Oluboyo et al. 2014). Such systems are less modulated by halokinetic controls than those that develop under dual-lateral confinement (e.g., Oluboyo et al. 2014; Rodriguez et al. 2020). Subsurface observations indicate that channels migrate away from growing structures (e.g., Mayall et al. 2010; Kane et al. 2012), however, those at Bakio West Bay appear to step towards the diapir in 2D (Fig. 6F, 7B). This could indicate that structural growth had reduced (Kane et al. 2012) and localised halokinetic controls on deposition below seismic resolution. Alternatively, the MTDs underlying the thick-bedded sandstones could form pathways that controlled sandstone deposition, and therefore the apparent movement towards the diapir was in fact controlled by the deep-water systems infilling debrite-related paleotopography (e.g. Armitage et al. 2009). However, deciphering detailing interpretations of 3D sinuous channels from 2D exposure remains challenging.

The Jata and Sollube basins have unique tectono-stratigraphic histories throughout the deposition of the BBF and LBF due to the interplay of halokinetic, allocyclic, and autocyclic controls. Inaccessible UBF stratigraphy to the west of Bakio (Fig. 11D) from UAV photographs appears to exhibit similar facies and geometries to UBF stratigraphy at northern Cabo Matxitxako (e.g., Vincente Bravo and Robles 1991; 1995) (Fig. 10) suggesting that halokinetic-influence decreased through time. This supports the idea that sediment accumulation rate ultimately outpaced diapir growth rate, possibly due to the increase in sediment supply associated with the uplift and erosion of the Landes Massif (e.g., Martín-Chivelet et al. 2002; Puelles et al.

2014). Partial or complete welding of salt bodies could also be, at least partially, responsible for the reduction of halokinetic-influence through time (e.g., Jackson and Hudec 2017).

Comparison to other settings

Recognition of halokinetically-influenced stratigraphy in the field

Prior to this study, most understanding of halokinetically-influenced deep-water systems came from subsurface datasets (e.g., Booth et al. 2003; Madof et al. 2009; Carruthers et al. 2013; Doughty-Jones et al. 2017). Features characterising deposition in halokinetic settings include: multi-scalar thinning and onlap, growth faulting, pebble conglomerates, mixed siliciclastic-carbonate lithologies, MTDs, variable paleocurrents, angular unconformities and abrupt facies variability (e.g., Dalgarno and Johnson 1968; Dyson 1999; Kernen et al. 2012; 2018; Carruthers et al. 2013; Counts and Amos 2015; Counts et al. 2019). Deposition of thick-bedded sandstones in the axis of the Sollube basin, and thinner beds and mudstones on the flanks of the Sollube and Jata basins is comparable to fluvial facies distribution (e.g. Banham and Mountney 2013a; b; 2014; Ribes et al. 2015) where channel-fill sandstones dominate axial settings and floodplain mudstones are observed closer to the diapir.

Individual beds within the BBF (Poprawski et al. 2014; 2016) are comparable in size (10-100's m packages) and composition to stacked MTDs reported overlying bounding unconformities in halokinetic sequences in the La Popa Basin (10-120 m in thickness) (e.g., Giles and Lawton 2002) associated with remobilization of diapir roof or cap rock. Smaller carbonate breccias with triangular geometries (metre-scale packages) (Fig. 7E) are similar in geometry and composition as 'Lentils' (1-100's m thick) described by McBride et al. (1974), but differ in thickness and areal extent. Giles and Lawton (2002) suggest lentils, MTDs and breccias represent talus-like failure from diapir roof stratigraphy (e.g., Rosales and Pérez-García 2010; Poprawski et al. 2014; 2016).

Presence of evaporite clasts within fluvial successions (e.g., Banham and Mountney 2013; Ribes et al. 2015), suggest nearby diapir was exposure during deposition. Such clasts are not observed in our study area, suggesting the Bakio and Guernica structures never breached the seabed. This fits the interpretation of carbonate platform growth above the structures, preventing salt exposure (e.g., García-Mondéjar 1990; Rosales and Pérez-García 2010; Poprawski et al. 2014; 2016).

The consistency of our observations and previously described halokinetically-influenced settings suggests that the criteria for recognising halokinetically-influenced systems is similar regardless of depositional environment, suggesting halokinetic controls are dominant over allocyclic ones. Multiple directions of ripple lamination, presence of hybrid beds, range ofMTD types, and abrupt juxtaposition of deep-water depositional facies, can be used to identify halokinetically-influenced deep-water systems in core and outcrop.

Comparison of static and active confinement

The gravity flows responsible for the Eocene to Oligocene Annot Sandstone, SE France were confined during deposition by Alpine fold and thrust belt topography (e.g., Apps 1987; Sinclair 1994; Soutter et al. 2019). When compared with active topography associated with diapir growth, the topography associated with orogenic deformation is effectively static.

Like the BFG, the stratigraphy of the Grès d'Annot is broadly progradational, and rapid facies changes occur over 10's of metres towards pinch-outs (Soutter et al. 2019). Unlike Bakio, where paleoflow was at a low angle to structural trend, sub-basins in the Annot area are eventually filled and sediment bypasses and spilled into subsequent down-dip basins (e.g., Prather et al. 2012; Soutter et al. 2019) indicating that paleoflow was perpendicular to at least one of the complex structural trends (Oluboyo et al. 2014). Nevertheless and similar to Bakio, interplaying axial and traverse sediment routing systems were coeval during deposition (Salles et al. 2014) (Fig. 12, 13, 14, 15).

MTDs in the Grès d'Annot are slope-derived and infrequent compare with this study area, which are sourced laterally from failures of stratigraphy above salt structures that are intercalated with axially-derived deep-water deposits (Fig. 12, 13, 14, 15). A reflection of a more active-slope in diapiric settings.

The stratigraphy in this study is characterised by an axial deep-water depositional system and a series of lateral systems dominated by MTDs fed from the growing salt structures. This interplay of two distinct depositional systems is common in deep water environments influenced by active rift topography, such as the Gulf of Corinth, Greece (e.g., Leeder and Gawthorpe 1987; Pechlivanidou et al. 2018; Cullen et al. 2019) and the Gulf of Suez, Egypt (e.g., Sharp et al. 2002; Jackson et al. 2002; 2005; Leppard et al. 2006). Here the continually evolving footwall scarps feeding lateral MTD rich systems coevally with axial, allocyclically controlled depositional systems. Deposits in syn-rift settings are often narrow and elongated parallel to the strike of normal fault segments (e.g., Carr et al. 2003; Jackson et al. 2005; Cullen et al. 2019), indicating the control on stratigraphic architecture by footwall physiography. Analogous depositional facies variability occurs due to salt structure evolution in halokinetically-influenced settings.

CONCLUSION

This study documents deep-water facies distributions, with variable amounts of topographic confinement, adjacent to growing salt structures from a rare exposed example. We compare observations from two minibasins, a confined (Sollube) and a partially confined (Jata), which are comparable in size and facies heterogeneity to known subsurface minibasins in salt provinces globally.

Stratigraphic variability and juxtaposition of architectural elements between the Jata and Sollube basins is high and controlled by the interplay of halokinetic, autocyclic and allocyclic processes. The low angle between the paleoflow and strike direction of salt structures result in the depositional system being focussed between two salt structures in the Sollube basin, and against one salt structure in the Jata basin, but with not evidence of a downdip flow confinement. Confinement against topography increases the effects of allocyclic progradation. Failure of carbonate platforms developed above the crests of the active Bakio diapir and Guernica structure created lateral MTDs in the flanking basins. The MTDs formed local topography further constraining axial depositional systems. MTDs can also be sourced axially from up-dip failures on the shelf, and the different compositions of MTDs ratifies that the Jata and Sollube basins are differently influenced.

Indicators of active topography include hybrid beds, remobilised strata, lateral thickness changes over short distances, reversal in ripple cross-laminating within beds and intercalation of MTDs throughout the stratigraphy. These indicators are not diagnostic of salt-influenced topography, but collectively provide a set of features that support interpretation of halokinetic modulation of a deepwater setting. Following the cessation of diapir growth, topography does not heal instantly and the 'passive' paleotopography continues to confine subsequent depositional systems despite diapir inactivity.

Closely related depositional systems can be highly variable depending on their complete or partial confinement. Stacked, amalgamated sandstones are observed between the confining barriers in the Sollube basin, whereas more variable architectures are observed in the Jata basin where only partial confinement is present. These observations are due to the modulation of a broadly progradational system by halokinetically-influenced laterally barriers and the coeval development of axial allocyclic and lateral MTD-rich depositional systems.

Utilising outcrop analogues combined with a good regional understanding of source area and salt movement and extracting learnings from depositional analogues are advised when exploring in the salt-sediment interface for carbon storage, geothermal or hydrocarbon reservoir targets.

ACKNOWLEDGMENTS

This paper contains work conducted during ZCs' PhD study undertaken as part of the Natural Environment Research Council (NERC) Centre for Doctoral Training (CDT) in Oil & Gas [grant number NEM00578X/1]. ZC is a recipient of an American Association of Petroleum Geologists (AAPG) Foundation Grant in-Aid 'Gustavus E.Archie Memorial Grant' which supported this fieldwork. Stereonet 10 is acknowledged for data plotting. Dave Lee is acknowledged for building digital outcrop models. Ross Grant is thanked for his comments, figure beautifying and proof-reading.

REFERENCES

Ábalos, B., 2016, Geologic map of the Basque-Cantabrian Basin and a new tectonic interpretation of the Basque Arc: International Journal of Earth Sciences, v. 105, p. 2327-2354.

Agirrezabala, L.M., 1996, El Aptiense-Albiense del Anticlinorio Nor-Vizcaino entre Gernika y Azpeitia. [PhD Thesis]: Euskal Herriko Unibertsitatea, Bilbo, 429 p.

Agirrezabala, L.M., and Bodego, A., 2005, Interbedded mudstone slope and basin-floor sandy deposits in the Ondarroa turbidite system (Albian, Basque-Cantabrian Basin): Geogaceta, v. 38, p. 83-86.

Agirrezabala, L.M., and Dinarés-Turell, J., 2013, Albian syndepositional block rotation and its geological consequences, Basque–Cantabrian Basin (Western Pyrenees): Geological Magazine, v. 150, p. 986–1001.

Agirrezabala, L.M., and García-Mondéjar, J., 1989, Evolución tectosedimentaria de la plataforma urgoniana entre Cabo Ogoño e Itziar durante el Albiense inferior y medio (Región Vasco-Cantábrica nor-oriental): Simposio del XII Congreso Español de Sedimentología. Leioa 11-20.

Agirrezabala, L.M., and López-Horgue, M., 2017, Environmental and ammonoid faunal changes related to Albian Bay of Biscay opening: Insights from the northern margin of the Basque-Cantabrian Basin: Journal of Sea Research, v. 130, p. 36-48.

Al -Ja'Aidi, 2000, The influence of topography and flow efficiency on the deposition of turbidites [PhD Thesis]: University of Leeds, UK, 162 p.

Alves, T.M., Manuppella, G., Gawthorpe, R.L., Hunt, D.W., and Monterio, J.H., 2003, The depositional evolution of diapir- and fault-bounded rift basins: examples from the Lusitanian Basin of West Iberia: Sedimentary Geology, v. 162, p. 273–303.

Alves, T.M., Gawthorpe, R.L., Hunt, D.W., and Monteiro, J.H., 2002, Jurassic tectono-sedimentary evolution of the Northern Lusitanian Basin (offshore Portugal): Marine and Petroleum Geology, v. 19, p. 727-754.

Amy, L.A., McCaffrey, W.D., and Kneller, B.C., 2004, The influence of a lateral basin-slope on the depositional patterns of natural and experimental turbidity currents, *in* Lomas, S.A., and Joseph, P., eds., Confined Turbidite Systems, Geological Society, London, Special Publications. v. 222, p. 311-330.

Apps, G.M., 1987. Evolution of the Grès d'Annot Basin, South West Alps [Ph.D. thesis]: University of Liverpool, UK.

Armitage, D.A., Romans, B.W., Covault, J.A., and Graham, S.A., 2009, The influence of mass-transport-deposit surface topography on the evolution of turbidite architecture: the Sierra Contreras, Tres Pas Formation (Cretaceous), Southern Chile: Journal of Sedimentary Research, v. 79, p. 287-301.

Baas, J.H., 2004, Conditions for formation of massive turbiditic sandstones by primary depositional processes: Sedimentary Geology, v. 166, p. 292-310.

Baas, J.H., Best, J.L., Peakall, J., and Wang, M., 2009, A phase diagram for turbulent, transitional and laminar clay suspension flows: Journal of Sedimentary Research, v. 79, p. 162-183.

Baas, J.H., Best, J.L. and Peakall, J., 2011, Depositional processes, bedform development and hybrid bed formation in rapidly decelerated cohesive (mud–sand) sediment flows: Sedimentology, v. 58, p. 1953-1987.

Baas, J.H., Davies, A.G., and Malarkey, J., 2013, Bedform development in mixed sand–mud: The contrasting role of cohesive forces in flow and bed: Geomorphology, v. 182, p. 19-32.

Bakke, K, Kane, I.A., Martinsen, O.J., Petersen, S.A., Johansen, T.A., Hustoft, S., Hadler, J., and Groth, A., 2013, Seismic modelling in the analysis of deep-water sandstone termination styles: AAPG Bulletin, v. 97, p. 1395-1419.

Banham, S.G., and Mountney, N.P., 2013a, Evolution of fluvial systems in salt-walled mini-basins: a review and new insights: Sedimentary Geology, v. 296, p. 142–166.

Banham, S.G., and Mountney, N.P., 2013b, Controls on fluvial sedimentary architecture and sediment-fill state in salt-walled mini-basins: Triassic Moenkopi Formation, Salt Anticline Region, SE Utah, USA: Basin Research, v. 25, p. 709–737.

Banham, S.G., and Mountney, N.P., 2014, Climatic versus halokinetic control on sedimentation in a dryland fluvial succession: Sedimentology, v. 61, p. 570–608.

Barker, S.P., Haughton, P.D.W., McCaffrey, W.D., Archer, S.G., and Hakes, B, 2008, Development of rheological heterogeneity in clay-rich high-density turbidity currents: Aptian Britannia Sandstone Member, UK continental shelf: Journal of Sedimentary Research, v. 78, p. 45–68.

Barr, B.C., Slinn, D.N., Pierro, T., and Winters, K.B., 2004, Numerical simulation of turbulent, oscillatory flow over sand ripples: Journal of Geophysical Research, v. 109.

Bodego, A., and Agirrezabala, L.M., 2013, Syn-depositional thin- and thick-skinned extensional tectonics in the mid Cretaceous Lasarte sub-basin, western Pyrenees: Basin Research, v. 25, p. 594-612.

Booth, J.R., Dean, M.C., Duvernay, A.E., and Styzen, M.J., 2003, Paleo-bathymetric controls on the stratigraphic architecture and reservoir development of confined fans in the Auger Basin: Central Gulf of Mexico slope: Marine and Petroleum Geology, v. 20, p. 563–586.

Boulesteix, K., Poyatos-More, M., Flint, S.S., Taylor, K.G., Hodgson., D.M., and Hasiotis, S.T., 2019, Transport and Deposition of Mud in Deep-water Environments: Processes and Stratigraphic Implications: Sedimentology, v. 66, p. 2894-2925.

Brooks, H.L., Hodgson, D.M., Brunt, R.L., Peakall, J., Hofstra, M., and Flint, S.S., 2018, Deep-water channel-lobe transition zone dynamics: Processes and depositional architecture, an example from the Karoo Basin, South Africa: Geological Society of America Bulletin, v. 130, p. 1-10.

Brunet, M.F., 1994, Subsidence in the Parentis Basin (Aquitaine, France): implications of the thermal evolution, *in* Mascle, A. eds., Hydrocarbon and Petroleum Geology of France: Special Publication of the European Association of Petroleum Geoscientists, v. 4, p.187–198.

Cámara, P., 2017, Salt and Strike-Slip Tectonics as Main Drivers in the Structural Evolution of the Basque-Cantabrian Basin, Spain, *in* Soto, J.I., Flinch, J.F., Tari, G., eds., Permo-Triassic Salt Provinces of Europe, North Africa and the Atlantic Margins, Elsevier, p. 371-393.

Carr, I.D., Gawthorpe, R.L., Jackson, C.A-L., Sharp, I.R., and Sadek, A., 2003, Sedimentology and sequence stratigraphy of early syn-rift tidal sediments: the Nukhul Formation, Suez Rift, Egypt: Journal of Sedimentary Research, v. 73, p. 407–420.

Carruthers, D., Cartwright, J., Jackson, M.P.A., and Schutjens, P., 2013, Origin and timing of layer-bound radial faulting around North Sea salt stocks: New insights into the evolving stress state around rising diapirs: Marine and Petroleum Geology, v. 48, p. 130-48.

Cecil, C.B., 2003, The concept of autocyclic and allocyclic controls on sedimentation and stratigraphy, emphasizing the climatic variable: SEPM Special Publication, v. 77, p. 13-20.

Charles, R., and Ryzhikov, K., 2015, Merganser Field: managing subsurface uncertainty during the development of a salt diapir field in the UK Central North Sea: *in* McKie, T., Rose, P.T.S., Hartley, A.J., Jones, D.W., and Armstrong, T.L., eds., Tertiary Deep-Marine reservoirs of the North Sea Region. Geological Society, London, Special Publications, v. 403, p. 261-298.

Clark, I.A., and Cartwright., J.A., 2009, Interactions between submarine channel systems and deformation in deepwater fold belts: Examples from the Levant Basin, Eastern Mediterranean sea: Marine and Petroleum Geology, v. 26, p. 1465-1482.

Clark, I.A., and Cartwright., J.A., 2011, Key controls on submarine channel development in structurally active settings: Marine and Petroleum Geology, v. 28, p. 1333-1349.

Counts, J.W., and Amos, K., 2016, Sedimentology, depositional environments and significance of an Ediacaran salt-withdrawal minibasin, Billy Springs Formation, Flinders Ranges, South Australia: Sedimentology, v. 63, p. 1084–1123.

Counts, J.W., Dalgarno, C.R., Amos, K.J., and Hasiotis, S.T., 2019, Lateral facies variability along the margin of an outcropping salt-withdrawal minibasin, South Australia: Journal of Sedimentary Research, v. 89, p. 28-45.

Cronin, B.T., Owen, D., Hartley, A.J., and Kneller, B., 1998, Slumps, debris flows and sandy deep-water channel systems: implications for the application of sequence stratigraphy to deep-water clastic sediments: Journal of the Geological Society of London, v. 155, p. 429–432.

Crimes, T.P., 1973, From limestones to distal turbidites: a facies and trace fossil analysis in the Zumaya flysch (Paleocene-Eocene), North Spain: Sedimentology, v. 20, p. 105-131.

Cullen, T.M,, Collier, R.E.L., Gawthorpe, R.L., Hodgson, D.M., and Barrett, B.J., 2019, Axial and transverse deep‐water sediment supply to syn‐rift fault terraces: Insights from the West Xylokastro Fault Block, Gulf of Corinth, Greece: Basin Research.

Cumberpatch, Z.A., Soutter, E.L., Kane, I.A., and Casson, M. A. 2020, Evolution of a mixed siliciclastic-carbonate deep-marine system on an unstable margin: the Cretaceous of the Eastern Greater Caucasus, Azerbaijan: Basin Research (in review), EarthArXiv.

Dalgarno, C.R., and Johnson, J.E., 1968, Diapiric structures and late Precambrian–early Cambrian sedimentation in Flinders Ranges, South Australia, *in* Braunstein, J., and O'Brien, G.D., eds., Diapirism and Diapirs: AAPG Memoir, v. 8, p. 301–314.

Davison, I., Alsop, G.I., Evans, N.G., and Safaricz, M., 2000b, Overburden deformation patterns and mechanisms of salt diapir penetration in the Central Graben, North Sea: Marine and Petroleum Geology, v. 17, p. 601–618.

De Blasio, F.V., Engvik, L.E., and Elverhøi, A., 2006, Sliding of outrunner blocks from submarine landslides: Geophysical Research Letters, v.30.

DeFelipe, I., Pedreira, D., Pulgar, J.A., Iriarte, E. and Medina, M., 2017, Mantle exhumation and metamorphism in the Basque-Cantabrian Basin (N Spain): Stable and clumped isotope analysis in carbonates and comparison with ophicalcites in the North-Pyrenean Zone (Urdach and Lherz): Geochemistry, Geophysics, Geosystems, v. 18, p. 631-652.

Deptuck, M., and Sylvester, Z., 2017, Submarine fans and their channels, levees and lobes, *in* Micallef, A., Krastel, S., Savini, A., eds., Submarine Geomorpology, p. 273-299.

Doughty-Jones, G., Mayall, M., AND Lonergan, L., 2017, Stratigraphy, facies, and evolution of deep-water lobe complexes within a salt controlled intraslope minibasin: AAPG Bulletin, v. 101, p. 1879-1904.

Doughty-Jones, G., Lonergan, L., Mayall, M., and Dee, S.J., 2019, The role of structural growth in controlling the facies and distribution of mass transport deposits in a deep-water salt minibasin: Marine and Petroleum Geology, v. 104, p. 106-124.

Dyson, I.A., 1999, The Beltana Diapir: a salt withdrawal mini-basin in the northern Flinders Ranges: Mines and Energy of South Australia, Journal, v. 15, p. 40–46.

Ericson, D.B., Ewing, M., and Heezen, B.C., 1952, Turbidity currents and sediments in North Atlantic: AAPG Bulletin, v. 36, p. 489-511.

Espejo, J., 1973, Mapa Geológico de España 1:50.000, Hoja 38 (Bermeo). Segunda Serie (MAGNA), Primera Edición IGME.

Espejo, J., and Pastor, F., 1973, Mapa Geológico de España 1:50.000, Hoja 37 (Algorta). Segunda Serie (MAGNA), Primera Edición IGME.

Etienne, S., Mulder, T., Bez, M., Desaubliaux, G., Kwasniewski, A., Parize, O., Dujoncquoy, E., and Salles, T., 2012, Multiple scale characterization of sand-rich distal lobe deposit variability: Examples from the Annot Sandstones Formation, Eocene–Oligocene, SE France, v. 273-274, p. 1-18.

Ferrer, O., Roca, E., Benjumea, B. Muñoz, J., and Ellouz, N., 2008, The deep seismic reflection MARCONI-3 profile: Role of extensional Mesozoic structure during the Pyrenean contractional deformation at the eastern part of the Bay of Biscay: Marine and Petroleum Geology, v. 25, p 714-730.

Ferrer, O., Arbues, P., Roca, E., Giles, K., Rowan, M., Matties, M., and Muñoz, J., 2014, Effects of diapir growth on Synkinimatic deepwater sedimentation: the Bakio diapir (Basque-Cantabrian Basin, Northern Spain): AAPG Search and Discovery article 41385.

Flint, S.S., and Hodgson, D.M., 2005, Submarine Slope Systems: Processes and Products *in* Hodgson, D.M. and Flint, S.S., eds., Submarine Slope Systems: Processes and Products, Geological Society London, Special Publication, v. 244, p. 1-6.

García-Mondéjar, J., 1990a, The Aptian-Albian carbonate episode of the Basque-Cantabrian basin (northern spain) general charactertistics controls and evolution, *in* Tucker, M.E., Wilson, J.L., Crevello, P.D., Sarg, J.F., and Reads, J.F., eds., Carbonate Platforms – facies, sequences and evolution: International Association of Sedimentologists Special Publication, v. 9, p. 257-290.

García-Mondéjar, J., 1996, Plate reconstruction of the Bay of Biscay: Geology, v. 24, p. 635-638.

García-Mondéjar, J., Fernandez-Mendiola, P.A., Agirrezabala, L.M., Aranburu, A., Lôpez-Horgue, M.A. Iriarte, E., and Martinez de Rituerto, S., 2004, El Aptiense-Albiense de la Cuenca Vascao-Cantabrica: Geologica de España, p. 291-296.

García-Mondéjar, J., and Robador, A., 1987, Sedimentacion y paleogeograf la del Complejo Urgoniano (Aptiense-Albiense) en el area de Bermeo (region Vasco-Cantabrica septentional): Acta Geologica Hispanica, v. 22, p. 411-418.

Garrote-Ruiz, A., García-Potero, J. A., Eguiguren-Altuna, E., and García-Pascual, I., 1991, Mapa de la Hoja n° 38-I (Bermeo) del Mapa Geológico del País Vasco a escala 1:25.000. Ente Vasco de la Energía-EVE, Bilbao.

Garrote-Ruiz, A., García-Potero, J. A., Eguiguren-Altuna, E., and García-Pascual, I., 1992, Mapa de la Hoja n° 38-III (Mungia) del Mapa Geológico del País Vasco a escala 1:25.000. Ente Vasco de la Energía-EVE, Bilbao.

Garrote-Ruiz, A., García-Potero, J. A., Eguiguren-Altuna, E., and García-Pascual, I., 1993a, Mapa de la Hoja n° 37-II (Armintza) del Mapa Geológico del País Vasco a escala 1:25.000. Ente Vasco de la Energía-EVE, Bilbao.

Garrote-Ruiz, A., García-Potero, J.A., Eguiguren-Altuna, E. and García-Pascual, I., 1993b, Mapa de la Hoja n° 37-IV (Getxo) del Mapa Geológico del País Vasco a escala 1:25.000. Ente Vasco de la Energía-EVE, Bilbao.

Gee, M.J.R., and Gawthorpe, R.L., 2006, Submarine channels controlled by salt tectonics: Examples form 3D seismic data offshore Angola: Marine and Petroleum Geology, v. 22, p. 443-458.

Gee, M.J.R., and Gawthorpe, R.L., 2007, Seismic geomorphology and evolution of submarine channels from the Angolan continental margin: Journal of Sedimentary Research, v. 77, p. 433-446.

Geluk, M., McKie, T., and Kilhams, B., 2018, An introduction to the Triassic: current insights into the regional setting and energy resource potential of NW Europe, *in* Kilhams, B., Kukla, P.A., Mazur, S., Mckie, T., Mijnlieff, H.F., Van Ojik, K., eds., Mesozoic Resource Potential in the Southern Permian Basin: Geological Society, London, Special Publications, p. 469.

Gervais, A., Sayoye, B., Mulder, T. and Gonthier, E., 2006, Sandy modern turbidite lobes: A new insight from high resolution seismic data: Marine and Petroleum Geology, v. 23, p. 485-502.

Giles, K., and Lawton, T., 2002, Halokinetic sequence stratigraphy adjacent to the El Papalote diapir, Northeastern Mexico: AAPG Bulletin, v. 86, p. 823-840.

Giles, K., and Rowan, M., 2012, Concepts in halokinetic-sequence deformation and stratigraphy, *in* Alsop, G.I., Archer, S.G., Hartley, A.J., Grant, N.T., and Hodgkinson, R., eds., Salt Tectonics, Sediments and Prospectivity: Geological Society, London, Special Publications, v. 363, p. 7-31.

Gómez, M., Verges, J., and Riaza, C., 2002, Inversion tectonics of the northern margin of the Basque Cantabrian Basin: Bulletin de la Society et Geologique de France, v. 173, p. 449-459.

Gorsline, D.S. and Emery, K.O., 1959, Turbidity-current deposits in San Pedro and Santa Monica basins off southern California: Geological Society of America Bulletin, v. 70, p. 279-290.

Hampton, M.A., 1972, The Role of Subaqueous Debris Flow in Generating Turbidity Currents: Journal of Sedimentary Petrology, v. 42, p. 775-793.

Haq, B.U., Hardenbol, J., and Vail, P.R., 1987, Chronology of fluctuating sea levels since the Triassic (250 million years ago to present): Science, v. 235, p. 1156- 1167.

Haq, B.U., 2014, Cretaceous eustasy revisited: Global and Planetary Change, v. 113, p. 44-58.

Haughton, P.D.W., 1994, Deposits of deflected and ponded turbidity currents, Sorbas basin, Southeast Spain: Journal of Sedimentary Research, v. 64, p. 233–246.

Haughton, P.D.W., Davis, C., McCaffrey, W., Barker, S., 2009, Hybrid sediment gravity flow deposits - Classification, origin and significance: Marine and Petroleum Geology, v. 26, p. 1900-1918.

Hodgetts, D., 2013, Laser scanning and digital outcrop geology in the petroleum industry: A review: Marine and Petroleum Geology, v.46, p. 335-354.

Hodgson, D.M., and Haughton, P.D.W., Impact of syndepositional faulting on gravity current behaviour and deep-water stratigraphy: Tabernas-Sorbas Basin, SE Spain, *in* Lomas, S.A., and Joseph, P., eds., Confined Turbidite Systems, Geological Society of London Special Publication, 222, pp. 135-158.

Hodgson, D.M., 2009, Distribution and origin of hybrid beds in sand-rich submarine fans of the Tanqua depocenter, Karoo Basin, South Africa: Marine and Petroleum Geology, v. 26, p. 1940-1956.

Hodgson, D.M., Di Clema, C.N., Brunt, R.L., and Flint, S.S., 2011, Submarine slope degradation and aggradation and the stratigraphic evolution of channel-levee systems: Journal of the Geological Society, v. 168, p. 625-628.

Hodgson, N.A., Farnsworth, J., and Fraser, A.J., 1992, Salt-related tectonics, sedimentation and hydrocarbonplays in the Central Graben, North Sea, UKCS, *in* Hardman, R.F.P., ed., Exploration Britain: Geological Insights for the Next Decade, Geological Society, London, Special Publications, v. 67, p. 31–63.

Hofstra, M., Hodgson, D.M., Peakall, J., and Flint, S.S., 2015, Giant scour-fills in ancient channel-lobe transition zones: Formative processes and depositional architecture: Sedimentary Geology, v. 329, p. 98-114.

Hubbard, S.M., Romans, B.W., and Graham, S.A., 2008, Deep-water foreland basin deposits of the Cerro Toro Formation, Magallanes basin, Chile: architectural elements of a sinuous basin axial channel belt: Sedimentology, v. 55, p. 1333-1359.

Hubbard, S.M., Covault, J.A., Fildani, A., and Romans, B.W., 2014, Sediment transfer and deposition in slope channels: Deciphering the record of enigmatic deep-sea processes from outcrop: Geological Society of America Bulletin, v. 126, p. 857-871.

Hudec, M., and Jackson, M., 2007, Terra infirma: Understanding salt tectonics: Earth-Science Reviews, v. 82, p. 1-28.

Hunnicutt, L.A., 1998, Tectonostratigraphic interpretation of Upper Cretaceous to lower Tertiary limestone lentils within the Potrerillos Formation surrounding El Papalote diapir, La Popa basin, Nuevo Leon, Mexico [MS Thesis]: New Mexico State University, Las Cruces, New Mexico, 181 p.

Inverson, R.M., 1997, The physics of debris flows: Reviews of Geophysics, v. 35, p. 245-296.

Inverson, R.M., Logan, M., Lahusen, R.G., and Berti, M., 2010, The perfect debris flow? Aggregated results from 28 largescale experiments: Journal of Geophysical Research: Earth Surface, v. 115, p. 1-29.

Jackson, M.P.A., and Hudec, M.R., 2017. Salt Tectonics: Principles and Practise, Cambridge University Press, p. 515.

Jackson, C.A.L., Gawthorpe, R.L., and Sharp, I.R., 2002, Growth and linkage of the East Tanka fault zone, Suez rift: structural style and syn-rift stratigraphic response: Journal of the Geological Society, v. 159, p. 175-187.

Jackson, C.A.L., Gawthorpe, R.L., Carr, I.D., and Sharp, I.R., 2005, Normal faulting as a control on the stratigraphic development of shallow marine syn-rift sequences: the Nukhul and Lower Rudeis Formations, Hammam Faraun fault block, Suez Rift, Egypt: Sedimentology, v. 52, p. 313-338.

Jackson, C.A.L., and Johnson, H.D., 2009, Sustained turbidity currents and their interaction with debrite-related topography; Labuan Island: Sedimentary Geology, v. 219, p. 77-96.

Janocko, M., Nemec, W., Henriksen, S. and Warchol, M., 2013, The diversity of deep-water sinuous channel belts and slope valley-fill complexes: Marine and Petroleum Geology, v.41, p. 7-34.

Jammes, S., Mannatschal, G., Lavier, L. and Masini, E., 2009, Tectonosedimentary evolution related to extreme crustal thinning ahead of a propagating ocean: an example of the western Pyrenees; Tectonophysics, v. 28.

Jobe, Z.R., Lowe, D.R., and Morris, W.R., 2012, Climbing-ripple successions in turbidite systems: depositional environments, sedimentation and accumulation times: Sedimentology, v. 59, p. 867-898.

Jobe, Z.R., Howes, N.C., and Auchter, N.C., 2016, Comparing submarine and fluvial channel kinematics: Implications for stratigraphic architecture: Geology, v. 44, p. 931–934.

Jobe, Z.R., Sylvester, Z., Howes, N., Pirmez, C., Parker, A., Cantelli, A., Smith, R., Wolinsky, M.A., O'Byrne, C., Slowey, N., and Prather, B., 2017, High-resolution, millennial-scale patterns of bed compensation on a sand-rich intraslope submarine fan, western Niger Delta slope: GSA Bulletin, v. 129, p. 23-37.

Johnson, S.D., Flint, S., Hinds, D. and De Ville Wickens, H., 2001, Anatomy, geometry and sequence stratigraphy of basin floor to slope turbidite systems, Tanqua Karoo, South Africa: Sedimentology, v. 48, p. 987-1023.

Jones, I.F., and Davison, I., 2014, Seismic imaging in and around salt bodies: Interpretation. v. 2, p. 1-20.

Jones, G., Mayall, M., and Lonergan, L., 2012, Contrasting depositional styles on a slope system and their control by salt tectonics—Through-going channels, ponded fans and mass transport complexes, *in* Rosen, N.C., Weimer, P., Coutes Dos Anjos, S., Henrickson, E., Marques, E., Mayall, M., and Fillon, R., eds., New understanding of the petroleum systems of continental margins of the world: 32nd Annual Gulf Coast Section SEPM Foundation Bob F. Perkins Research Conference, Houston, Texas, December, v. 2–5, p. 503–533.

Kane, I.A., McCaffrey, W.D., and Martinsen, O.J., 2009, Allogenic vs. Autogenic Controls on Megaflute Formation: Journal of Sedimentary Research, v. 79, p. 643-651.

Kane, I.A., Catterall, V., McCaffrey, W.D. and Martinsen, O.J., 2010, Submarine channel response to intrabasinal tectonics: The influence of lateral tilt: AAPG bulletin, v. 94, p. 189-219.

Kane, I.A., McGee, D.T., and Jobe, Z.R., 2012, Halokinetic effects on submarine channel equilibrium profiles and implications for facies architecture: conceptual model illustrated with a case study from Magnolia Field, Gulf of Mexico: *in* Alsop, G.I., Archer, S.G., Hartley, A.J., Grant, N.T., and Hodgkinson, R., eds., Salt Tectonics, Sediments and Prospectivity: Geological Society, London, Special Publications, v. 363, p. 289-302.

Kane, I.A., Pontén, A.S., Vangdal, B., Eggenhuisen, J.T., Hodgson, D.M., Spychala, Y.T., 2017, The stratigraphic record and processes of turbidity current transformation across deep-marine lobes: Sedimentology, v. 64, p. 1236-1273.

Kane, I.A., and Hodgson, D.M., 2011, Sedimentological criteria to differentiate submarine channel levee subenvironments: Exhumed examples from the Rosario Fm. (Upper Cretaceous) of Baja California, Mexico, and the Fort Brown Fm. (Permian), Karoo Basin, S. Africa: Marine and Petroleum Geology, v. 28, p. 807-823.

Kane, I.A. and Pontén, A.S.M., 2012, Submarine transitional flow deposits in the Paleogene Gulf of Mexico: Geology, v 40, p. 1119-1122.

Kernen, R.A., Giles, K.A., Rowan, M.G., Lawton, T.F., and Hearon, T.E., 2012, Depositional and Halokinetic-Sequence Stratigraphy of the Neoproterozoic Wonoka Formation Adjacent to Patawarta Allochthonous Salt Sheet, Central Flinders Ranges, South Australia, *in* Alsop, G.I., Archer, S.G., Hartley, A.J., Grant, N.T., and Hodgkinson, R., eds., Salt Tectonics, Sediments and Prospectivity: Geological Society, London, Special Publications, v. 363, p. 81–105.

Kernen, R.A., Giles, K.A., Poe, P.L., Gannaway Dalton, C.E., Rowan, M.G., Fiduck, J.C., and Hearon, T.E., 2018, Origin of the Neoproterozoic rim dolomite as lateral carbonate caprock, Patawarta Salt Sheet, Flinders Ranges, South Australia: Australian Journal of Earth Sciences.

Kilhams, B.A., Hartley, A., Huuse, M., Davis, C., 2012, Characterizing the Paleocene turbidites of the North Sea: the Mey Sandstone Member, Lista Formation, UK Central Graben: Petroleum Geoscience, v. 18, p. 337-354.

Kilhams, B.A., Hartley, A., Huuse, M., and Davis, C., 2015, Characterizing the Paleocene turbidites of the North Sea: Maureen Formation, UK Central Graben, *in* McKie, T., Rose, P.T.S., Hartley, A.J., Jones, D.W., and Armstrong, T.L., eds., Tertiary Deep-Marine reservoirs of the North Sea Region. Geological Society, London, Special Publications, v. 403, p. 43-62.

Kneller, B.C., Edwards, D., McCaffrey, W.D., and Moore, R., 1991, Oblique reflection of turbidity currents: Geology, v. 19, p. 250 252.

Kneller, B.C., and Bramney, M.J., 1995, Sustained high-density turbidity currents and the deposition of thick massive sands: Sedimentology, v. 42, p. 607-616.

Kneller, B.C., and McCaffrey, W.D., 1999, Depositional effects of flow non-uniformity and stratification within turbidity currents approaching a bounding slope: deflection, reflection and facies variation: Journal of Sedimentary Research, v. 69, p. 980-991.

Kneller, B., Dykstra, M., Fairweather, L., and Milana, J.P., 2016, Mass-transport and slope accommodation: Implications for turbidite sandstone reservoirs: AAPG Bulletin, v. 100, p. 213-235.

Laudon, R.C., 1975, Stratigrphy and petrology of the Difunta Group, La Popa and eastern Parras Basins, northeastern Mexico [Ph.D. Dissertation]: University of Texas, Austin.

Leeder, M.R., and Gawthorpe, R.L., 1987, Sedimentary models for extensional tilt-block/half-graben basins: Geological Society, London, Special Publications, v. 28, p. 139–152.

Leppard, C.W., and Gawthorpe, R.L., 2006, Sedimentology of rift climax deep water systems; Lower Rudeis Formation, Hammam Faraun Fault Block, Suez Rift, Egypt: Sedimentary Geology, v. 191, p. 67–87.

Lerche, I. and Petersen, K. 1995. Salt and sediment dynamics, London, 336 p.

López-Horgue, M.A., Owen, H.G., Aranburu, A., Fernández-Mendiola, P.A. and García-Mondéjar, J., 2009, Early late Albian (Cretaceous) of the central region of the Basque-Cantabrian Basin, northern Spain: biostratigraphy based on ammonites and orbitolinids: Cretacaceous Research, v. 30, p. 385–400.

Lotze, F., 1953, Salzdiapirismus im nördlichen Spanien: Journal of the German Geological Society, v. 105, p. 814 – 822.

Lowe, D.R., 1982, Sediment gravity flows: II Depositional models with special reference to the deposits of high-density turbidity currents: Journal of Sedimentary Research, v. 52. p. 279-297.

Lowe, D.R., and Guy, M., 2000, Slurry-flow deposits in the Britannia Formation (Lower Cretaceous), North Sea: a new perspective on the turbidity current and debris flow problem: Sedimentology, v. 47, p. 31-70.

Macdonald, H.A., Peakall, J., Wignall, P.B., and Best, J., 2011, Sedimentation in deep-sea lobe-elements: Implications for the origin of thickening-upward sequences; Journal of the Geological Society, London, v. 168, p. 319–331.

Madof, A.S., Christie-Blick, N., and Anders, M.H., 2009, Stratigraphic controls on a salt-withdrawal intraslope minibasin, north-central Green Canyon, Gulf of Mexico: Implications for misinterpreting sea level change: AAPG Bulletin, v. 93, p. 636-561.

Mannie, A.S., Jackson, C. A-L., and Hampson, G.J., 2014, Shallow-marine reservoir development in extensional diapir-collapse minibasins: An integrated subsurface case study from the Upper Jurassic of the Cod terrace, Norwegain North Sea: AAPG Bulletin, v. 98, p. 2019-2055.

Mathey, B., 1987, Les flysch du Cretaceous superieur des Pyrenes basques (France, Espagne): Geological Memoirs University of Dijon, p. 1-12.

Marini, M., Milli, S., Ravnås, R., and Moscatelli, M., 2015, A comparative study of confined vs. semiconfined turbidite lobes from the Lower Messinian Laga Basin (Central Apennines, Italy): Implications for assessment of reservoir architecture: Marine and Petroleum Geology, v. 63, p. 142-165.

Martín-Chivelet, J., Breastegui, X., Rosales, I., Vera, J.A., Vilas, L., Caus, R., Greafe, K-I., Sergua, M., Puig, C., Mas, R., Robles, S., Floquet, M., Quesada, S., Ruiz-Ortiz, P. A., Fregenal-Martinez, M.A., Salas. R., Garcia, A., Martin-Algaraara, A., Arias, C., Melendez, N., Chacon, B., Molina, J.M., Sanz, J.L., Castro, J.M., Garcia-Hernandez, M., Carenas, B., Garcia-Hibalgom J., and Ortega, F., 2002, Cretaceous, *in* Gibbons, W., and Moreno, T., eds., The Geology of Spain, Geological Society, London, Special Publications. p. 255-292.

Martín-Martín, J.D., Vergés, J., Saura, E., Moragas, M., Messager, G., Baqués, V., Razin, P., Grélaud, C., Malaval, M., Joussiaume, R., Casciello, E., Cruz-Orasa, I., and Hunt, D.W., 2016, Diapiric growth within an Early Jurassic rift basin: The Tazoult salt wall (central High Atlas, Morocco): Tectonics, v. 36, p. 2-32.

Mayall, M., Jones, E., and Casey, M., 2006, Turbidite channel reservoirs key elements in facies prediction and effective Development: Marine and Petroleum Geology, v. 23, p. 821–841.

Mayall, M., Lonergan, L. Bowmn, A., James, S., Milles, K., Primmer, T., Pope, D. Rogers, L., and Skeene, R., 2010, The response of turbidite slope channels to growth-induced seabed topography: AAPG Bulletin, v. 94, p. 1011-1030.

McArthur, A., Kane, I.A., Bozetti, G., Hansen, L., and Kneller, B.C., 2020, Supercritical flows overspilling from bypass-dominated submarine channels and the development of overbank bedforms: The Depositional Record, v. 6 (1), p. 21-40.

McBride, E.F., Weidie, A.E., Wolleben, J.A., and Laudon, R.C., 1974, Stratigraphy and structure of the Parras and La Popa Basins, Northeastern Mexico: Geolgoical Society of America Bulletin. v. 85, p. 1603-1622.

McCaffrey, W.D., and Kneller, B.C., 2001, Process controls on the development of stratigraphic trap potential on the margins of confined turbidite systems and aids to reservoir evaluation: AAPG Bulletin, v. 85, p. 971-988.

Morris, E.A., Hodgson, D.M., Flint, S.S., Brunt, R.L., Butterworth, P.J., and Verhaeghe, J., 2014, Sedimentology, stratigraphic architecture, and depositional context of submarine frontal-lobe complexes; Journal of Sedimentary Research, v. 84, p. 763-780.

Moscardelli, L., and Wood, L., 2008. New classification system for mass transport complexes in offshore Trinidad: Basin Research, v. 20, p. 73-98.

Mutti, E., 1974, Examples of ancient deep-sea fan deposits from circum Mediterranean geosynclines in modern and ancient geosynclinal sedimentation, *in*: Dott, R.H., Jr. and Shaver, R.H., eds., Modern and ancient geosynclinal sedimentation. Society of Economic Paleontologists and Mineralogists, Special Publications, v.19, p. 92–105.

Mutti, E., 1992, Turbidite Sandstones: AGIP – Instituto di Geologia, Università di Parma, p. 275.

Mutti, E., and Normark, W.R., 1987, Comparing examples of modern and ancient turbidite systems: problems and concepts, *in* Legget, J.R., and Zuffa, G.G., eds., Marine Clastic Sedimentology. p. 1-38.

Nardin, T.R., Hein, F.J., Gorsline, D.S., and Edwards, B.D., 1979, A review of mass movement processes, sediment and acoustic characteristics, and contrasts in slope and base-of-slope systems versus canyon-fan-basin floor systems: SEPM Special Publications, v. 27, p. 61-73.

Normark, W.R., Piper, D.J.W., and Hess, G.R., 1979, Distributary channels, sand lobes, and mesotopography of navy submarine fan, California Borderland, with application to ancient fan sediments: Sedimentology, v. 26, p. 749–774.

Olafiranye, K., Jackson, C. A-L. and Hodgson, D.M., 2013, The role of tectonics and mass-transport complex emplacement on upper slope stratigraphic evolution: A 3D seismic case study from offshore Angola: Marine and Petroleum Geology, v. 44, pp. 196-216.

Oluboyo, A.P., Gawthorpe, R.L., Bakke, K. and Hadler-Jacobsen, F., 2014, Salt tectonic controls on deep-water turbidite depositional systems: Miocene, southwestern Lower Congo Basin, offshore Angola: Basin Research, v. 26, p. 597-620.

Ortiz-Karpf, A., Hodgson, D.M., and McCaffrey, W.D., 2015, The role of mass-transport complexes in controlling channel avulsion and the subsequent sediment dispersal patterns on an active margin: the Magdalena Fan, offshore Colombia: Marine and Petroleum Geology, v. 64, p. 58-75.

Ortiz-Karpf, A., Hodgson, D.M., Jackson, C.A-L., and McCaffrey, W.D., 2016, Mass-Transport Complexes as Markers of Deep-Water Fold-and-Thrust Belt Evolution: Insights from the Southern Magdalena Fan, Offshore Colombia: Basin Research, v. 30, p. 65-88.

Patacci, M., Haughton, P.D., and McCaffrey, W.D., 2014, Rheological complexity in sediment gravity flows forced to decelerate against a confining slope, Braux, SE France: Journal of Sedimentary Research, v. 84, p. 270-277.

Peakall, J., Amos, K.J., Keevil, G.M., Bradbury, P.W., and Gupta, S., 2007, Flow processes and sedimentation in submarine channel bends: Marine and Petroleum Geology, v. 24, p. 470-486.

Pechlivanidou, S., Cowie, P.A., Hannisdal, B., Whittaker, A.C., Gawthorpe, R.L., Pennos, C., and Riiser, O.S., 2018, Source-to-sink analysis in an active extensional setting: Holocene erosion and deposition in the Sperchios rift, central Greece: Basin Research, v. 30, p. 522-543.

Pemberton, E.A.L., Hubbard, S.M., Fildani, A., Romans, B., and Stright, L., 2016, The stratigraphic expression of decreasing confinement along a deep-water sediment routing system: Outcrop example from southern Chile: Geosphere, v. 12, p. 114-134.

Pichel, L.M, and Jackson, C. A-L., 2020, Four-dimensional variability of Composite Halokinetic Sequences: Basin Research, online early.

Pickering, K.T., and Bayliss, N.J., 2009, Deconvolving tectono-climatic signals in deep-marine siliciclastics, Eocene Ainsa basin, Spanish Pyrenees: Seesaw tectonics versus eustacy; Geology, v. 37, p. 203-206.

Piper, D.J.W., and Normark, W.R., 1983, Turbidite depositional patterns and flow characteristics, Navy Submarine Fan, California Borderland: Sedimentology, v. 30, p. 681-694.

Poprawski, Y., Basile, C., Agrirrezabala, L.M., Jaillard, E., Gaudin, M., and Jacquin, T., 2014, Sedimentary and structural record of the Albian growth of the Bakio salt diapir (the Basque Country, northern Spain): Basin Research, v. 26, p. 746-766.

Poprawski, Y., Basile, C., Jaillard, E., Gaudin, M., and Lopez, M., 2016, Halokinetic sequences in carbonate systems: An example from the Middle Albian Bakio Breccias Formation (Basque Country, Spain): Sedimentary Geology, v. 334, p. 34-52.

Poprawski, Y., and Basile, C., 2018, Long-lasting diapir growth history in the Basque-Cantabrian Basin (northern Spain): a review, Penrose conference presentation.

Posamentier, H.W., and Kolla, V., 2003, Seismic geomorphology and stratigraphy of depositional elements in deep-water settings: Journal of Sedimentary Research, v. 73, p. 367-388.

Prather, B.E., Booth, J.R., Steffens, G.S., and Craig, P.A., 1998, Classification, lithologic calibration, and stratigraphic succession of seismic facies of intraslope basins, deep-water Gulf of Mexico: AAPG Bulletin, v. 82, p. 701-728.

Prather, B.E., Pirmez, C., Winker, C.D., Deptuck, M.E., and Mohrig, D., 2012, Stratigraphy of linked intraslope basins: Brazos-Trinity system western Gulf of Mexico. Application of the principles of seismic geomorphology to continental-slope and base-of-slope systems: Case studies from seafloor and near-seafloor analogues: SEPM, Special Publication, v. 99, p. 83-109.

Pratson, L.F., and Ryan, W.B.F., 1994, Pliocene to recent infilling and subsidence of intraslope basins offshore Louisiana: American Association of Petroleum Geologists Bulletin, v. 78, p. 1483–1506.

Prélat, A., Hodgson, D.M., and Flint, S.S., 2009, Evolution, architecture and hierarchy of distributary deep-water deposits: a high-resolution outcrop investigation from the Permian Karoo Basin, South Africa: Sedimentology, v. 56, p. 2132-2154.

Prélat, A., Covault, J.A., Hodgson, D.M., Fildani, A., and Flint, S.S., 2010, Intrinsic controls on the range of volumes, morphologies, and dimensions of submarine lobes: Sedimentary Geology, v. 232, p. 66-76.

Prélat, A., and Hodgson, D.M., 2013, The full range of turbidite bed thickness patterns in submarine lobes: Controls and implications; Journal of the Geological Society, v. 170, p. 209-214.

Pringle, J.K., Brunt, R.L., Hodgson, D.M., and Flint, S.S., 2010, Capturing stratigraphic and sedimentological complexity from submarine channel complex outcrops to digital 3D models, Karoo Basin, South Africa: Petroleum Geoscience, v. 16, p. 307-330.

Puelles, P., Ábalos, B., García De Madinabeitia, S., Sánches-Lorda, M.E., Fernández-Armas, S., and Gil Ibarguchi, J.I., 2014, Provenance of quartz-rich metamorphic tectonite pebbles from the 'Black Flysch' (W Pyrenees, N Spain): An EBSD and detrital zircon LA-ICP-MS study: Tectonophysics, v. 632, p. 123-137.

Pujalte, V., Robles, S., and Garcìa-Mondéjar, J., 1986, Caracteristicas sedimentológicas y paleogeográficas del fan-delta albiense de la Formación Monte Grande y sus relaciones con el Flysh Negro (Arminza-Górliz, Vizcaya): Acta Geologica Hispánica, v. 21, p. 141–150.

Pujalte, V., Baceta, J.I., Payros, A., Orue-Etxebarria, X., and Serra-Kiel, J., 1994, Late Cretaceous- Middle Eocene Sequence Stratigraphy and Biostratigraphy of the SW and W Pyrenees (Pamplona and Basque

Basins): a Field Seminar of the Groupe de Etude du Paleogene. IGCP Project 286, Universidad del País Vasco/Euskal Herriko Univertsitatea, p. 118.

Pujalte, V., Baceta, J.I., Orue-Etxebarria, and X., Payros, A., 1998, Paleocene strata of the Basque Country, W Pyrenees, N Spain: facies and sequence development in a deep-water, starved basin, *in* De Graciansky, P.C., Hardenbol, J., Jacquin, T., Vail, P.R., eds., Mesozoic and Cenozoic Sequence Stratigraphy of European basins, SEPM Special Publication, v. 60, p. 311-325.

Rat, P., 1988, The Basque-Cantabrian Basin between the Iberian and the European Plates. Some facts but still many problems: Revista de la Sociedad de Geologica de España, v.1, p. 3-4.

Remacha, E., Fernandez, L.P., and Maestro, E., 2005, The transition between sheet-like lobe and basin-plain turbidites in the Hecho Basin (South-Central Pyrenees, Spain): Journal of Sedimentary Research, v. 75, p. 798-819.

Ribes, C., Kergaravat, C, Bonnel, C., Crumeyrolle, P., Callot, J-P., Poisson, A., Temiz, H., AND Ringenbach, J-C., 2015, Fluvial sedimentation in a salt-controlled mini-basin: Stratal patterns and facies assemblages, Sivas Basin, Turkey: Sedimentology, v. 62, p. 1513-1545.

Robles, S., Pujalte, V., and García-Mondéjar, J., 1988, Evolucion de los sistemas sedimentarios del margen continental canabrico durante el Albiense y Cenomaniense, en la transversal del litoral Vizcaino: Revista de la Sociedad de Geologia de España, v. 1, p. 3-4.

Robles, S., Garrote, A., and García-Mondéjar, J., 1989, XII Congreso Español de Sedimentología: Simposios y conferencias. Universidad del País Vasco, Departamento de Estratigrafía, Geodinámica y Paleontología, Bilbao.

Rodriguez, C.R., Jackson, C.A-L., Rotevatn, A., Bell, R.E., and Francis, M., 2018, Dual tectonic-climatic controls on salt giant deposition in the Santos Basin, offshore Brazil: GEOSPHERE, v. 14, p. 215-242.

Rodriguez, C.R., Jackson, C.A-L., Bell, R.E., Rotevatn, A., and Francis, M., 2019, Deep-water reservoir distribution on a salt-influenced slope, Santos Basin, offshore Brazil: AAPG Bulletin, in press.

Romans, B.W., Fildani, A., Hubbard, S.M., Covault, J.A., Fosdick, J.C., and Graham, S.A., 2011, Evolution of deep-water stratigraphic architecture, Magallanes Basin, Chile: Marine and Petroleum Geology, v. 28 (3), p. 612-628.

Rosales, I., and Pérez-García, A., 2010, Porosity development, diagenesis and basin modelling of a Lower Cretaceous (Albian) carbonate platform from northern Spain, *in* van Buchem, F.S.P., Gerdes, K.D., and Esteban, M., eds., Mesozoic and Cenozoic Carbonate System of the Mediterranean and the Middle East: Stratigraphic and Diagenetic Reference Models, Geological Society, London, Special Publications. v. 329, p. 317-342.

Rowan, M.G., Giles, K.A., Roca, E., Arbues, P., and Ferrer, O., 2012b, Analysis of Growth Strata Adjacent to an Exposed Deepwater Salt Diapir, northern Spain: AAPG Annual Convention, Long Beach, USA.

Salles, L., Ford, M., and Joseph, P., 2014, Characteristics of axially-sourced turbidite sedimentation on an active wedge-top basin (Annot Sandstone, SE France): Marine and Petroleum Geology, v. 56, p. 305-323.

Scott, E.D., Gelin, F., Jolley, S.J., Leenaarts, E., Sadler, S.P., and Elsinger, R.J., 2010, Sedimentological control of fluid flow in deep marine turbidite reservoirs: Pierce Field, UK Central North Sea, *in* Jolley, S.J., Fisher, Q.J., Ainsworth, R.B., Vrolijk, P.J., and Delisle, S., eds., Reservoir Compartmentalization, Geological Society, London, Special Publications, v. 347, p. 113–132.

Sharp, I.R., Gawthorpe, R.L., Underhill, J.R., and Gupta, S., 2002, Fault-propagation folding in extensional settings: Examples of structural style and synrift sedimentary response from the Suez rift, Sinai, Egypt: Bulletin of the Geological Society of America, v. 112, p. 1877–1899.

Sinclair, H.D., 1994, The influence of lateral basinal slopes on turbidite sedimentation in the Annot sandstones of SE France: Journal of Sedimentary Research, v. 64, p. 42-54.

Sinclair, H.D., and Tomasso, M., 2002, Depositional evolution of confined turbidite basins: Journal of Sedimentary Research, p. 72, v. 451-456.

Sohn, Y.K., 2000, Depositional processes of submarine debris flows in the Miocene fan deltas, Pohang Basin, SE Korea with special reference to flow transportation: Journal of Sedimentary Research, v. 70, p. 491-503.

Sohn, Y.K., Choe, M.Y., and Jo, H.R., 2002, Transition from debris flow to hyperconcentrated flow in a submarine channel (the Cretaceous Cerro Toro Formation, southern Chile): Terra Nova, v. 14, p. 405-415.

Soto, R., Beamud, E., Roca, E., Carola, E., and Almar, Y., 2017, Distinguishing the effect of diapir growth on the magnetic fabrics of syn-diapiric overburden rocks: Basque Cantabrian Basin, Northern Spain: Terra Nova, v. 29, p. 191-201.

Soutter, E.L, Kane, I.A., and Huuse, M., 2018, Giant submarine landslide triggered by Paleocene mantle plume activity in the North Atlantic: Geology, v. 46, p. 511-514.

Soutter, E.L., Kane, I.A., Fuhrmann, A., Cumberpatch, Z.A., and Huuse, M., 2019, The Stratigraphic Evolution of Onlap in Clastic Deep-Water Systems: Autogenic Modulation of Allogenic Signals: Journal of Sedimentary Research, v. 89 (10), p. 890-917.

Soutter, E.L., Cumberpatch, Z.A., Bell, D. Ferguson, R.A., Kane, I.A., Spychala, Y.T., and Eggenhuisen, J. 2020, The effect of topographic orientation on confined turbidity currents and their deposits: Frontiers In Earth Science (In review), EarthArXiv.

Spychala, Y.T., Hodgson, D.M., Prélat, A., Kane, I.A., Flint, S.S., and Mountney, N.P., 2017, Frontal and lateral submarine lobe fringes: comparing sedimentary facies, architecture and flow processes: Journal of Sedimentary Research, v. 87, p. 75-96.

Stevenson, C.J., Jackson, C.A-L., Hodgson, D.M., Hubbard, S.M., and Eggenhuisen, J.T., 2015, Deep-water sediment bypass: Journal of Sedimentary Research, v. 85, p. 1058-1081.

Straub, K.M., Mohrig, D., Mcelroy, B., Buttles, J., and Pirmez, C., 2008, Interactions between turbidity currents and topography in aggrading sinuous submarine channels: A laboratory study: GSA Bulletin, v. 120, p. 368-385.

Sumner, E.J., Peakall, J., Parsons, D.R., Wynn, R.B., Darby, S.E., Dorrell, R.M., McPhail, S.D., Perrett, J., Webb, A., and White, D., 2013, First direct measurements of hydraulic jumps in an active submarine density current: Geophysical Research Letters, v. 40, p. 5904-5908.

Sylvester, Z., Cantelli, A., and Pirmez, C., 2015, Stratigraphic evolution of intraslope minibasins: Insights from surface-based model: AAPG Bulletin, v. 99, p. 1099-1129.

Talling, P., Masson, D., Sumner, E., and Malgesinil, G., 2012, Subaqueous sediment density flows: Depositional processes and deposit types: Sedimentology, v. 59, p. 1937-2003.

Teixell, A., Labaume, P., Ayarza, P., Espurt, N., De Saint Blanquat, M. and Lagabrielle, Y., 2018, Crustal structure and evolution of the Pyrenean-Cantabrian belt: A review and new interpretations from recent concepts and data: Tectonophysics, v. 724-725, p. 146-170.

Teles, V., Chauveau, B., Joseph, P., Weill, P., and Maktouf, F., 2016, CATS- A process-based model for turbulent turbidite systems at reservoir scales: Comptes Rendus Geoscience, v. 384, p. 473-478.

Vail, P.R., Mitchumi, R.M., Jr., Todd, R.G., Widmier, J.M., Thompson, S., III, Sangree, J.B., Bubb, J.N., and Hatelid, W.G., 1977, Seismic stratigraphy and global changes of sea-level, *in* Payton, C.E., ed., Seismic stratigraphy-applications to hydrocarbon exploration: AAPG Memoir, v. 26, p. 49-212.

Van Der Voo, R., 1969, Paleomagnetic evidence for the rotation of the Iberian peninsula: Tectonophysics, v. 7, p. 5-56.

Vicente Bravo, J., and Robles, S., 1991a, Geometría y modelo deposicional de la secuencia Sollube del Flysch Negro (Albiense medio, norte de Bizkaia): Geogaceta, v. 10, p. 69–72.

Vicente Bravo, J., and Robles, S., 1991b, Caracterización de las facies de la transición canal- lóbulo en la secuencia Jata del Flysch Negro (Albiense Superior norte de Vizcaya): Geogaceta,v. 10, p. 72–75.

Vicente Bravo, J.C., and Robles, S., 1995, Large-scale mesotopographic bedforms from the Albian Black Flysch, northern Spain: characterization, setting and comparisons with recent analogues, *in* Pickering, K.T., Hiscott, R.N., Kenyon, N.H., Ricci Luchi, F., and Smith, R.D.A., eds., Atlas of Deep-water Environments: Architectural Style in Turbidites Systems, 216-226.

Warren, J., 1999, Evaporites: Their evolution and economics: Oxford, Blackwell Science, 438 p.

Warren, J., 2006, Evaporites: Sediments, resources, and hydrocarbons: Berlin, Springer, 1035 p.

Walker, R.G., 1978, Deep-water sandstone facies and ancient submarine fans: Models for exploration for stratigraphic traps: AAPG Bulletin, v. 62, p. 932-966.

Wang, X., Luthi, S.M., Hodgson, D.M., Sokoutis, D., Willingshofer, E., Groenenberg, R.M., 2017, Turbidite stacking patterns in salt-controlled minibasins: Insights from integrated analogue models and numerical fluid flow simulations, Sedimentology, v. 64, pp.530-552.

Winker, C.D., 1996, High resolution seismic stratigraphy of a late Pleistocene submarine fan ponded by salt-withdrawal mini-basins on the Gulf of Mexico Continental slope: Proceedings from 1996 Offshore Technology Conference, paper OTC 8024, May 6–9, 1996, Houston, Texas, p. 619–628.

Wynn, R.B., Kenyon, N.H., Masson, D.G., Stow, D.A.V., and Weaver, P.P.E., 2002, Characterization and recognition of deep-water channel-lobe transition zones: AAPG Bulletin,v. 86, p. 1441–1462.

Wu, N., Jackson, C.A-L., Johnson, H.D., Hodgson, D.M., and Nugraha, H.D., 2020, Mass-transport complexes (MTCs) document subsidence patterns in a northern Gulf of Mexico salt minibasin: Basin Research, online early.

Zamora, G., Fleming, M., and Gallastegui, J., 2017, Salt Tectonics within the offshore Asturian Basin: North Iberian Margin. *in* Soto, J.I., Flinch, J.F., Tari, G., eds., Permo-Triassic Salt Provinces of Europe, North Africa and the Atlantic Margins, Elsevier, p. 371-393.

FIGURE CAPTIONS

Figure 1: Sketch summarising the structural controls, with respect to gravity-driven processes, on depositional systems from the shelf to basin floor. Note the complex and sinuous paths taken by slope channels around salt structures (Modified from Mayall et al. 2010).

Figure 2: Simplified geological map, stratigraphy and cross-section of the Basque-Cantabrian Basin (BCB), highlighting numerous present day surface exposures of NE-SW orientated diapirs (including the Bakio diapir, the focus of this study), commonly flanked by Cretaceous strata. The inset map shows the location of the BCB in northern Spain. Line A-A' locates cross section and line B-B' locates Figure 4. Black box locates Figure 3. Stratigraphy indicates mega sequences that can be used to group basin fill (after Ábalos 2016). Cross-section is modified from Poprawski et al. 2016.

Figure 3: A) Geological map and B) stratigraphic column for the study area. A) Compiled from Espejo and Pastor (1973), Espejo (1973), Garrote-Ruiz et al. (1991, 1992, 1993a &b), Pujalte et al. (1986), García-Mondéjar and Robador (1987), Robles et al. (1988, 1989), Vicente Bravo and Robles (1991a; 1991b), Poprawski et al. (2014; 2016), Ábalos (2016) and fieldwork observations. Lateral facies changes in carbonates around the salt outcrops at Guernica are modified from García-Mondéjar and Robador (1987). Located in Figure 2. The Guernica structure has been weathered away and forms a present-day estuary. Green lines show locations of stratigraphic logs shown in succeeding figures, dashed lines indicate missing section. B) Abbreviations for stratigraphic units are shown in ( ) and formation names of Poprawski et al. (2014; 2016), where they differ from those used in this study, are shown in [ ]. Numbers adjacent to stratigraphy refer to regional sequences of Agirrezabala and López-Horgue (2017), based on biostratigraphy. Line of section is shown for Figure 4, for full extent see Figure 2.

Figure 4: Schematic structural-stratigraphic cross section through the Bakio and Guernica diapirs. Full extent is located using B-B' on Figure 2, partial extent also shown on Figure 3. The section combines Poprawski and Basile (2018), Robles et al (1988), field observations and publically available vintage onshore seismic lines from IGME. Facies are indicated where known or inferred from literature, but are left blank where they cannot be inferred. 2 times vertical exaggeration for clarity.

Figure 5: Siliciclastic facies photographs. Yellow arrow indicates way up. Peach outline highlights scale, either lens cap (52 mm), or indicated. A) Granular-cobbly laterally extensive sandstone thick beds. B) Granular-cobbly sandstone with medium-thickness beds exhibiting lateral facies variations. C) Stacked, amalgamated thick-bedded sandstones. D) Medium-bedded sandstones interspersed with mudstones and poorly-sorted mudstones and sandstones. E) Thin-bedded sandstone showing ripples, planar lamination and loading. F) Succession of stacked thin-bedded sandstones. G) Siltstone and very-thin bedded sandstones, phosphate nodules are common in this facies. H) Mudstone with occasional, rare drapes of siltstone. I) Poorly-sorted mudstone, foundered into by a thick bedded sandstone. J) Poorly-sorted muddy sandstone, containing sporadic granules and raft blocks. K) Chaotic clast-rich matrix-supported deposit encased between units of thin-medium bedded sandstones. L) Tri-partite bed consisting of lower medium-bedded sandstone with weak cross-lamination, middle poorly-sorted mudstone and upper poorly-sorted sandstone. M) Bi-partite bed consisting of lower thick-bedded sandstone which becomes mud-clast rich upwards overlain by a poorly-sorted mudstone above.

Figure 6: Type examples of the seven documented facies associations within this study (Table 3). A) Thick-bedded sandstones of lobe-axis. B) Interbedded sandstones and mudstones of lobe off-axis. C) Thin bedded sandstones interbedded with mudstones of the proximal fringe. D) Mudstones and very thin bedded sandstones and siltstones of distal fringe. E) Thick-bedded granular sandstones of channel-lobe transition zone. F) Sandstones and poorly sorted mudstones of channel-axis. F) Thin bedded sandstones interbedded with mudstones of the channel axis. Peach highlights scale, either lens cap (52 mm), or indicated. Black arrow points to the north and Yellow shows way up.

Figure 7: Photographs showcasing the variety of geometries observed in the study area. North indicated. Peach highlights scale. A) Tabular bedded B) Concave upward, white lines highlight individual architectural elements C) Pinching-out upslope, black lines highlight pinch-out geometry D) Convex upwards, white lines highlight each element E) Pinching-out downslope, white lines outline triangular geometries and white arrows indicate onlap (also in 5C). F) Undulose G) Tabular amalgamated beds, white lines outline individual beds.

Figure 8: Sedimentological log through the Black Flysch Group at Gaztelugatxe Island. Located in Figure 3. Transects of individual logs are separated by missing sections as highlighted, and are therefore not continuous. Similar sedimentary facies on either side of the fault suggest GX 3 continues on both sides of the structure, and the structure is minor. Key for all logs shown. Thicknesses are in metres. GX # relate to stratigraphic units discussed in text. Pie chart shows MTD data divided by predominant clast type and MTD type (Table 2), relative proportions of all MTDs at this section and average thickness of each type is shown.

Figure 9: Large-scale channelized architectures and facies variability at Bakio West Bay, located on Figure 3. A and B are stratigraphic logs, which are located on D and blown up for clarity. Thickness is in metres. Key on Figure 8. BW # refers to stratigraphic unit discussed in text. Dashed line between logs show correlation. C) Pie chart shows MTD data divided by predominant clast type and MTD type (Table 2), relative proportions of all MTDs at this section and average thickness of each type is shown. D) Un-interpreted and E) Interpreted large scale architectures and facies details at Bakio West Bay. Unconformities are from Poprawski et al. 2014, and are highlighted in red where they divide packages of stratigraphy. U4 of Poprawski et al. (2014) is not laterally extensive and appears to represent an isolated, erosionally based depositional element (Fig. 9E). Based on these observations and the presence of channel axis facies associations we suggest U4 represents the base of a channel cut and not a halokinetic angular unconformity (*sensu* Giles and Rowan 2012). Black box on photograph locates channel axis facies association (Fig. 5F). F) Clasts of Gaztelugatxe Limestone which form out-runner blocks and act as sea floor topography.

Figure 10: Sedimentary log through Cabo Matxitxako Beach. Located on Figure 3. Missing sections are indicated, thickness is in metres. Key for all logs is provided in Figure 8. CM # indicate stratigraphic units discussed in text. Roughly 500 m of missing section separates South and North Cabo Matxitxako. Pie chart shows MTD data divided by predominant clast type and MTD type (Table 2), relative proportions of all MTDs at this section and average thickness of each type is shown.

Figure 11: Evidence for topography and palaeoflow direction, black arrow shows orientation and peach indicates scale, lens cap is 52mm. A) Rose diagram for 284 palaeocurrent indicators (ripples, sole marks, cross-stratification) from the Black Flysch Group. Readings have been corrected for tectonic tilt, yellow arrow indicates dominant palaeoflow direction, some radial spread due to ripple reflection. Grey arrows indicate regional (to the south) and local (to the west) palaeoflow directions, discussed in text. B) Evidence for opposing direction ripples suggesting ripple reflection. C) Triassic-aged Keuper Group outcrop of clays, carbonate and gypsum at Bakio Beach thought to be part of the Bakio diapir. D) Halokinetic sequence associated with the western flank of the Bakio diapir, HS = Halokinetic sequence. E) Onlap of lowermost Black Flysch Group thin-bedded turbidites onto a Gaztelugatxe Limestone clast on the eastern flank of the diapir. F) High density turbidite terminating against a block of Gaztelugatxe Limestone within HS 3.

Figure 12: Schematic depositional models showing the geological evolution of the system through time, specifically detailing deep-water sub-environments and their interactions with salt induced topography. Black line on top of each model outlines present day coastline. Bakio and Guernica structures are indicated. Guernica salt body geometry is hypothetic. Extrapolations between localities are based on topography, outcrop pattern and UAV imagery, A-C are after Poprawski et al. 2014, D-G are based on this study, location of stratigraphic units discussed in text (e.g. GX1, CM1) are shown. A-G are schematic with dimensions indicated in A. H is present day and to scale based on Figure 3 and Figure 5, with two times vertical exaggeration, representing post Cretaceous inversion, uplift and erosion.

Figure 13: Schematic deep-water facies and architectural elements observed on both flanks of the Bakio diapir showing the sub-seismic scale heterogeneity that can be associated with these systems and diapir

flank plays. Section is vertically exaggerated twice. Sollube and Jata Basins are indicated. Note change in orientation at the Bakio diapir.

Figure 14: Comparison between unconfined and confined lobe sub-environments (A-C) and progradation style within these settings (D-F). A and B compare the nomenclature of sub-environments of Spychala et al. (2017) and Soutter et al. (2019) from the Karoo and Annot basins respectively. Confined systems are smaller, more elongate and have more frequent hybrid beds. C shows how active topography would modify the model proposed by Soutter et al. (2019). One salt body has a carbonate roof and one a siliciclastic roof purely for clarity. D shows compensational stacking occurring during system progradation. E shows how progradation may be accelerated by parallel topography, based on flume tank experiments by Soutter et al. 2019b and the western flank of the Bakio diapir. F shows how progradation is further accelerated as gravity flow deposits are funnelled through dual- confinement. Both clastic and carbonate failures are shown on E and F to indicate diapiric influence on axial deposition. LDT: low-density turbidite, HB: Hybrid Bed, MDT: medium-density turbidite, HDT: high-density turbidite.

Figure 15: Thought experiment comparing the effects of variable topography in deep marine system evolution. Unconfined settings, partially confined systems and confined systems are compared. Unconfined settings are based on Prélat et al. 2009 and Sphycala et al. 2017. One structural barrier is based on the Jata basin and Soutter et al. in prep. Two salt barriers based on Sollube basin. Upper image indicates schematic map section. Black line shows line of section shown in chronostratigraphy and lithostratigraphy. Chronostratigraphy shows deposition during time step (t1-6). Lithostratigraphy shows how deposits relate to topography and previous deposits. Key is the same as Figure 14. Arrows on salt structures indicate periods of salt rise, lack of arrows suggest relative quiescence. No scale implied.

TABLE CAPTIONS

Table 1: Carbonate facies table detailing the major observations of the six facies which comprise the early Albian Bakio Marls and early Middle Albian Bakio Breccias formation. Yellow arrow indicates way up. Peach outline highlights scale, either lens cap (52 mm) or indicated.

Table 2: Siliciclastic facies table detailing the 10 facies that comprise the Black Flysch Group.

Table 3: Facies association table detailing the assemblages that comprise the Black Flysch Group.

Table 4: Table describing geometrical configurations observed within the Black Flysch Group.

Figure

Click here to access/download;Figure;Figure1.pdf

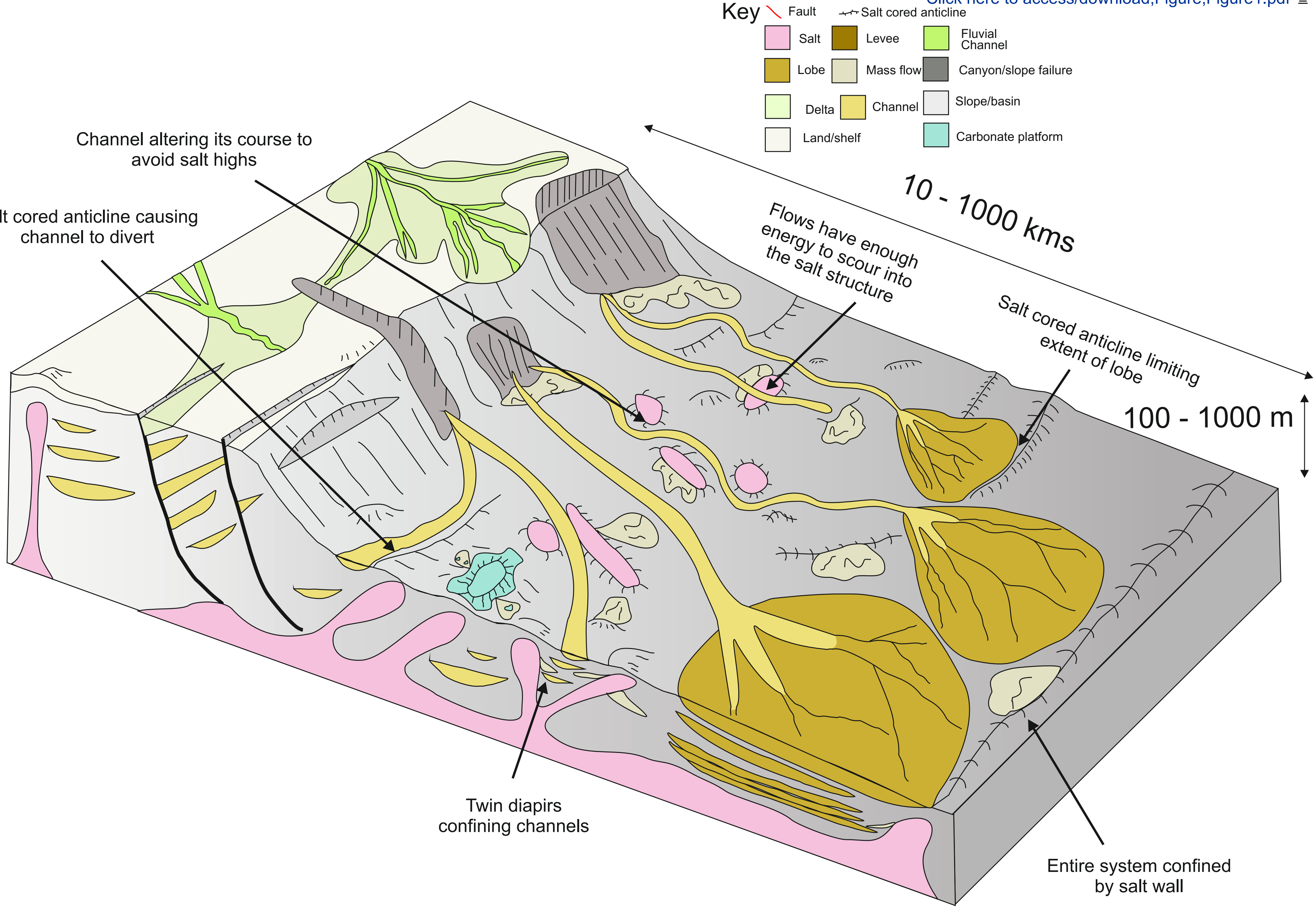

Figure

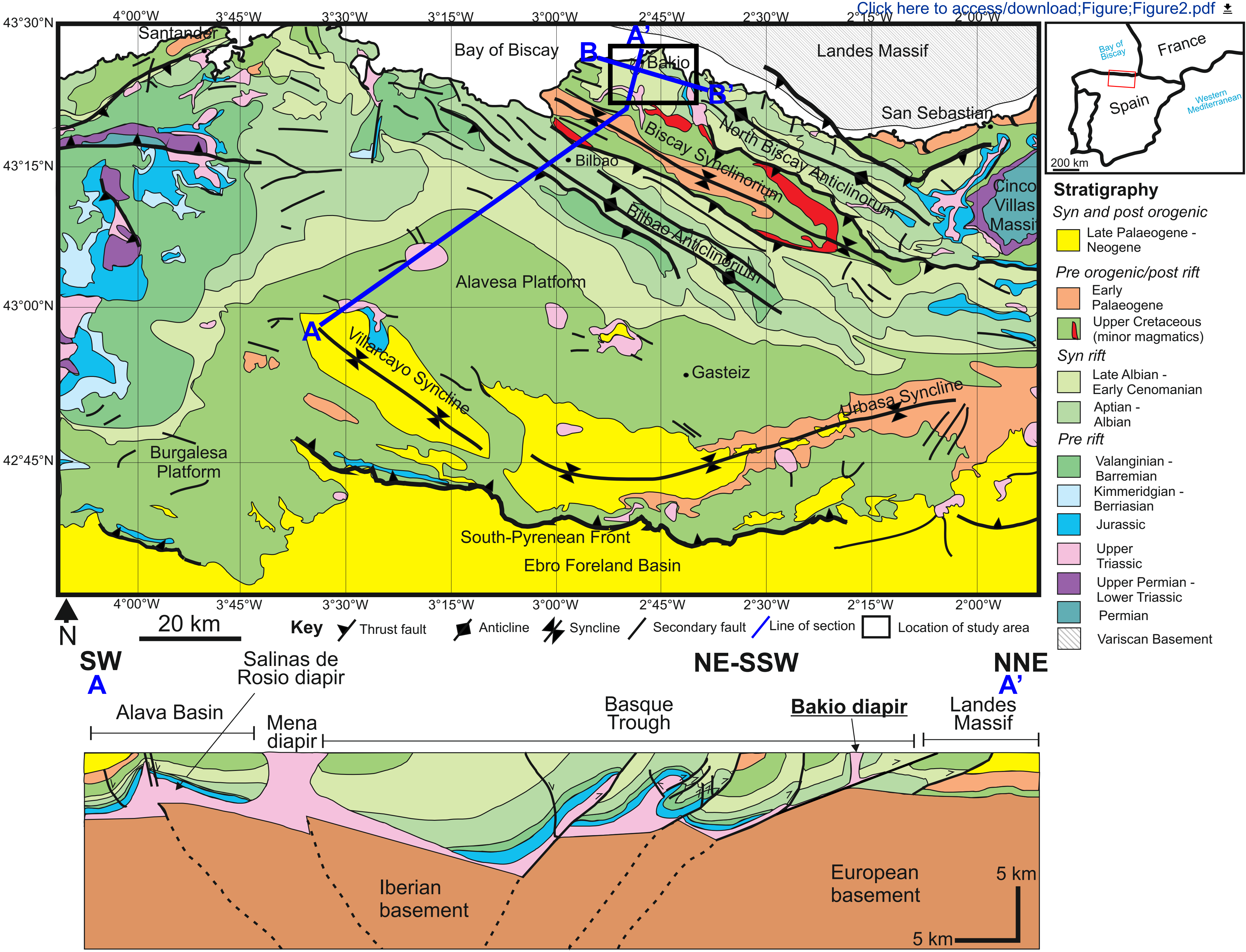

43°30'N
43°15'N
43°00'N
42°45'N
4°00'W
3°45'W
3°30'W
3°15'W
3°00'W
2°45'W
2°30'W
2°15'W
2°00'W
Santander
Bay of Biscay
A'
B
B'
Bakio
Landes Massif
San Sebastian
Bilbao
Biscay Synclinorium
North Biscay Anticlinorium
Bilbao Anticlinorium
Cinco Villas Massif
Alavesa Platform
A
Villarcayo Syncline
Gasteiz
Urbasa Syncline
Burgalesa Platform
South-Pyrenean Front
Ebro Foreland Basin
N
20 km
Key
Thrust fault
Anticline
Syncline
Secondary fault
Line of section
Location of study area
Bay of Biscay
France
Spain
Western Mediterranean
200 km
Stratigraphy
Syn and post orogenic
Late Palaeogene - Neogene
Pre orogenic/post rift
Early Palaeogene
Upper Cretaceous (minor magmatics)
Syn rift
Late Albian - Early Cenomanian
Aptian - Albian
Pre rift
Valanginian - Barremian
Kimmeridgian - Berriasian
Jurassic
Upper Triassic
Upper Permian - Lower Triassic
Permian
Variscan Basement
SW
A
NE-SSW
NNE
A'
Salinas de Rosio diapir
Alava Basin
Mena diapir
Basque Trough
Bakio diapir
Landes Massif
Iberian basement
European basement
5 km
5 km

Figure

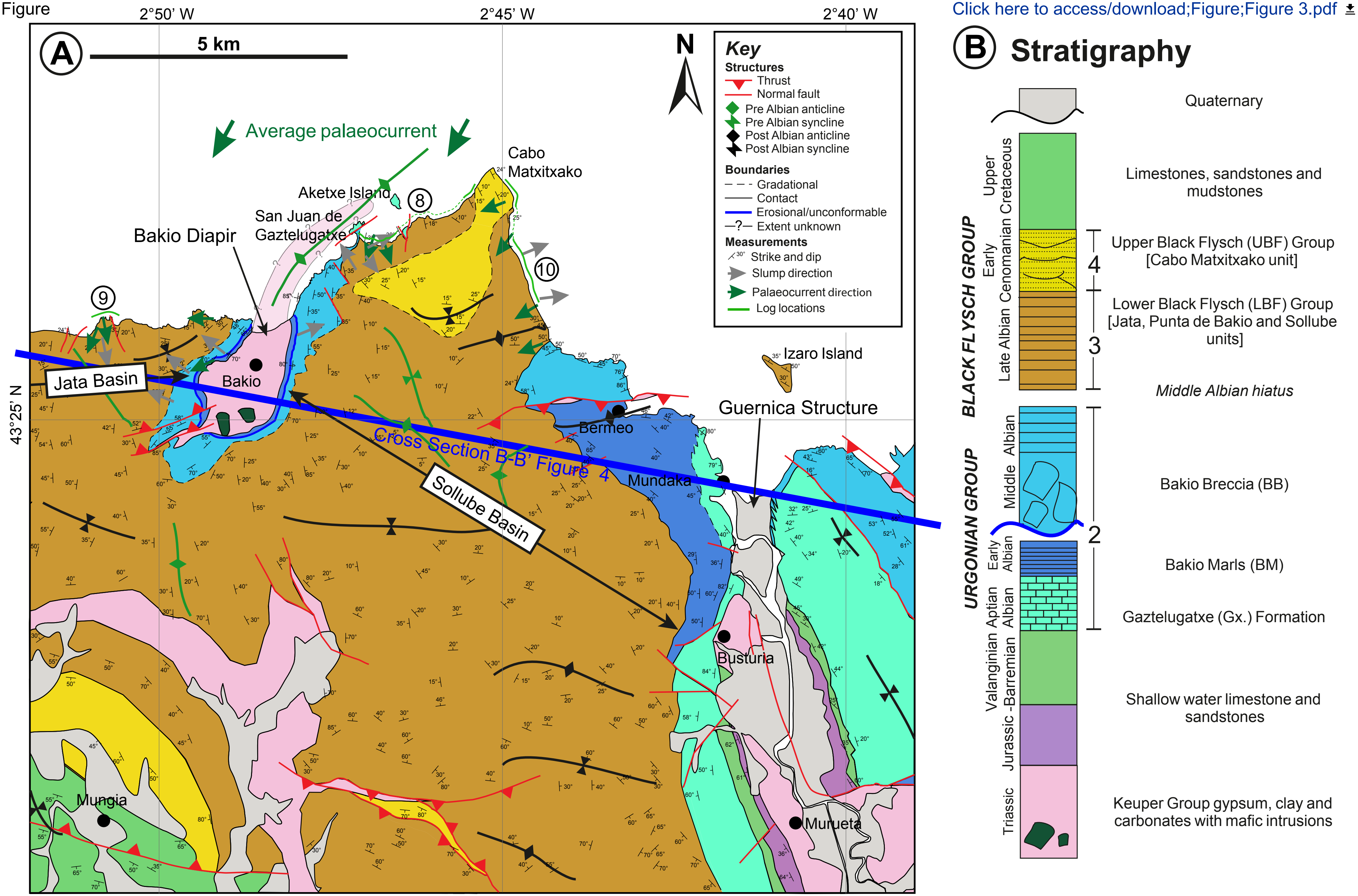

A
2°50' W
2°45' W
2°40' W
43°25' N
5 km
N
Key
Structures
Thrust
Normal fault
Pre Albian anticline
Pre Albian syncline
Post Albian anticline
Post Albian syncline
Boundaries
Gradational
Contact
Erosional/unconformable
Extent unknown
Measurements
Strike and dip
Slump direction
Palaeocurrent direction
Log locations
Average palaeocurrent
Cabo Matxitxako
Aketxe Island
San Juan de Gaztelugatxe
Bakio Diapir
Bakio
Jata Basin
Sollube Basin
Cross Section B-B' Figure 4
Izaro Island
Guernica Structure
Bermeo
Mundaka
Busturia
Murueta
Mungia
8
9
10
B
Stratigraphy
Quaternary
BLACK FLYSCH GROUP
Upper Cretaceous
Limestones, sandstones and mudstones
Early Cenomanian
Upper Black Flysch (UBF) Group [Cabo Matxitxako unit]
4
Late Albian
Lower Black Flysch (LBF) Group [Jata, Punta de Bakio and Sollube units]
3
Middle Albian hiatus
URGONIAN GROUP
Middle Albian
Bakio Breccia (BB)
2
Early Albian
Bakio Marls (BM)
Aptian Albian
Gaztelugatxe (Gx.) Formation
Valanginian -Barremian
Shallow water limestone and sandstones
Jurassic
Triassic
Keuper Group gypsum, clay and carbonates with mafic intrusions

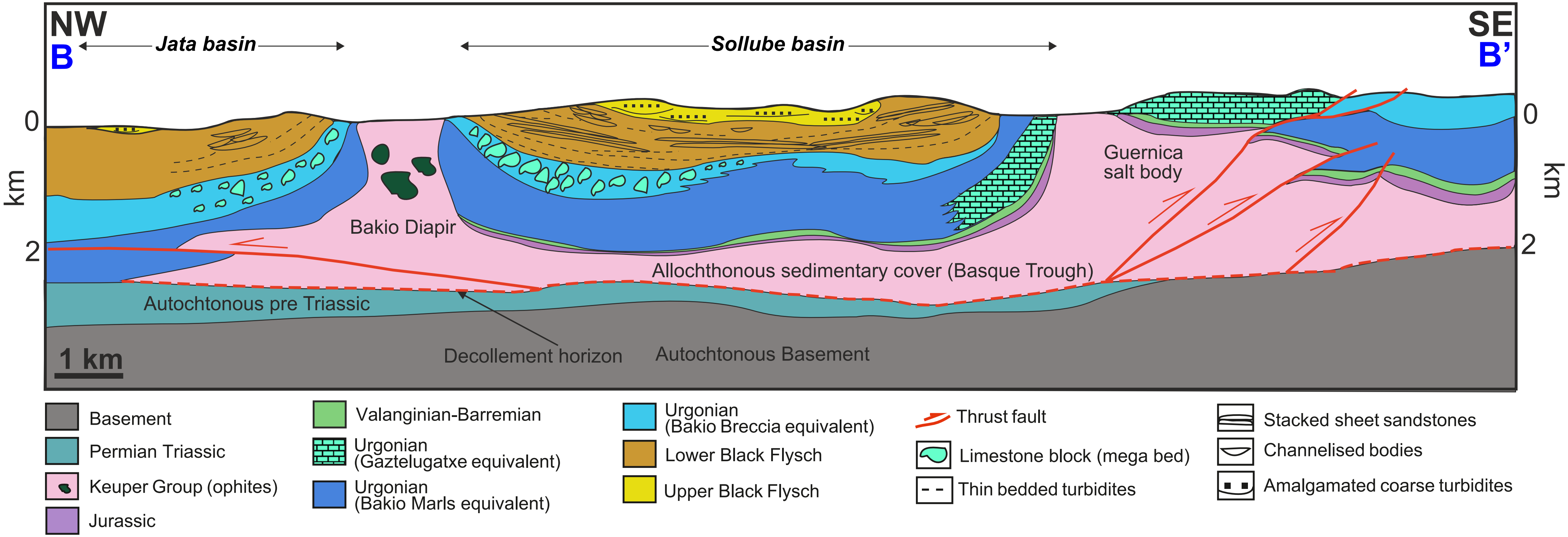
NW
B
Jata basin
Sollube basin
SE
B'
0
2
km
0
2
km
Bakio Diapir
Guernica
salt body
Allochthonous sedimentary cover (Basque Trough)
Autochtonous pre Triassic
Decollement horizon
Autochtonous Basement
1 km
Basement
Permian Triassic
Keuper Group (ophites)
Jurassic
Valanginian-Barremian
Urgonian
(Gaztelugatxe equivalent)
Urgonian
(Bakio Marls equivalent)
Urgonian
(Bakio Breccia equivalent)
Lower Black Flysch
Upper Black Flysch
Thrust fault
Limestone block (mega bed)
Thin bedded turbidites
Stacked sheet sandstones
Channelised bodies
Amalgamated coarse turbidites

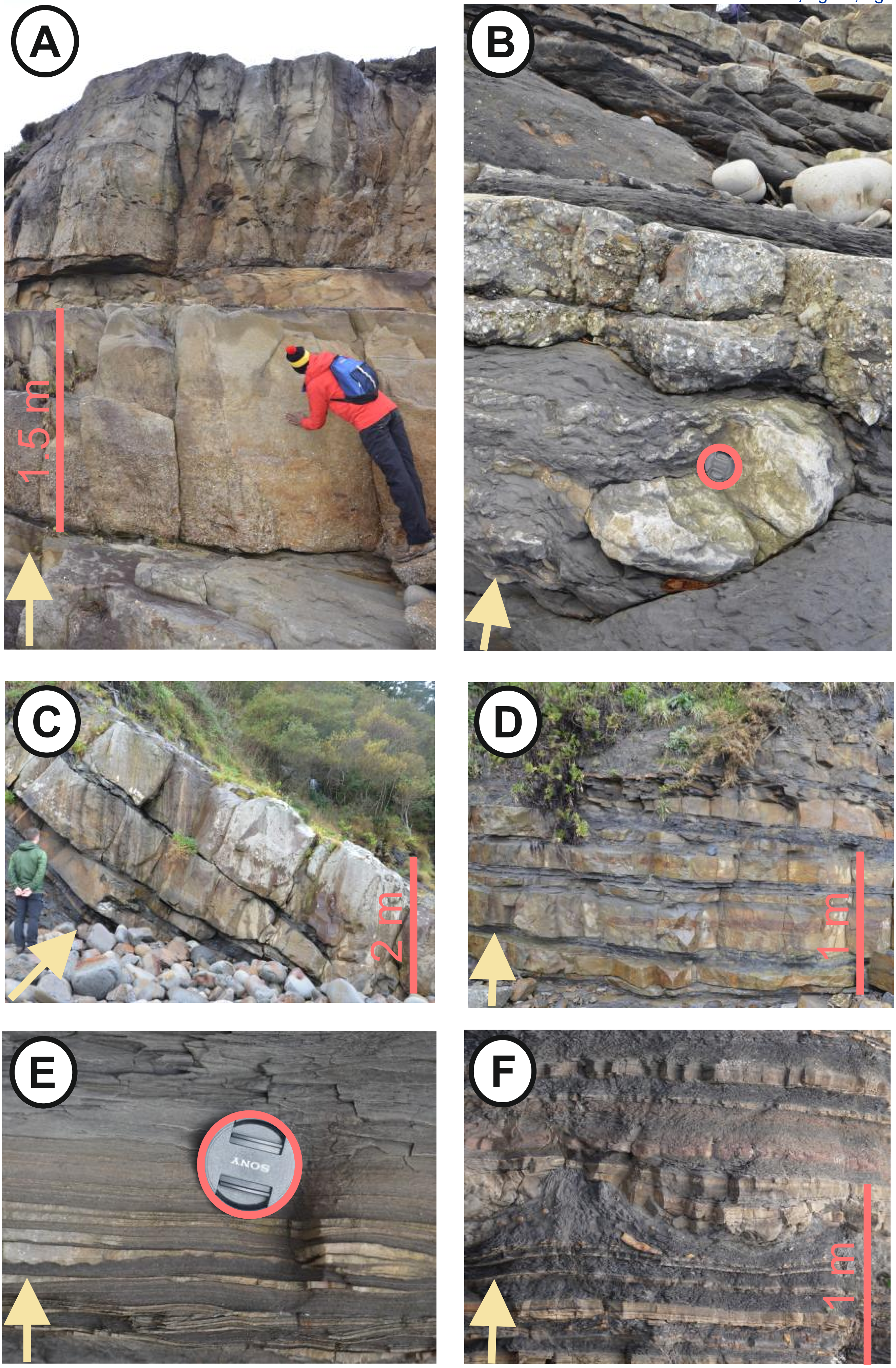
A
1.5 m
B
C
2 m
D
1 m
E
F
1 m

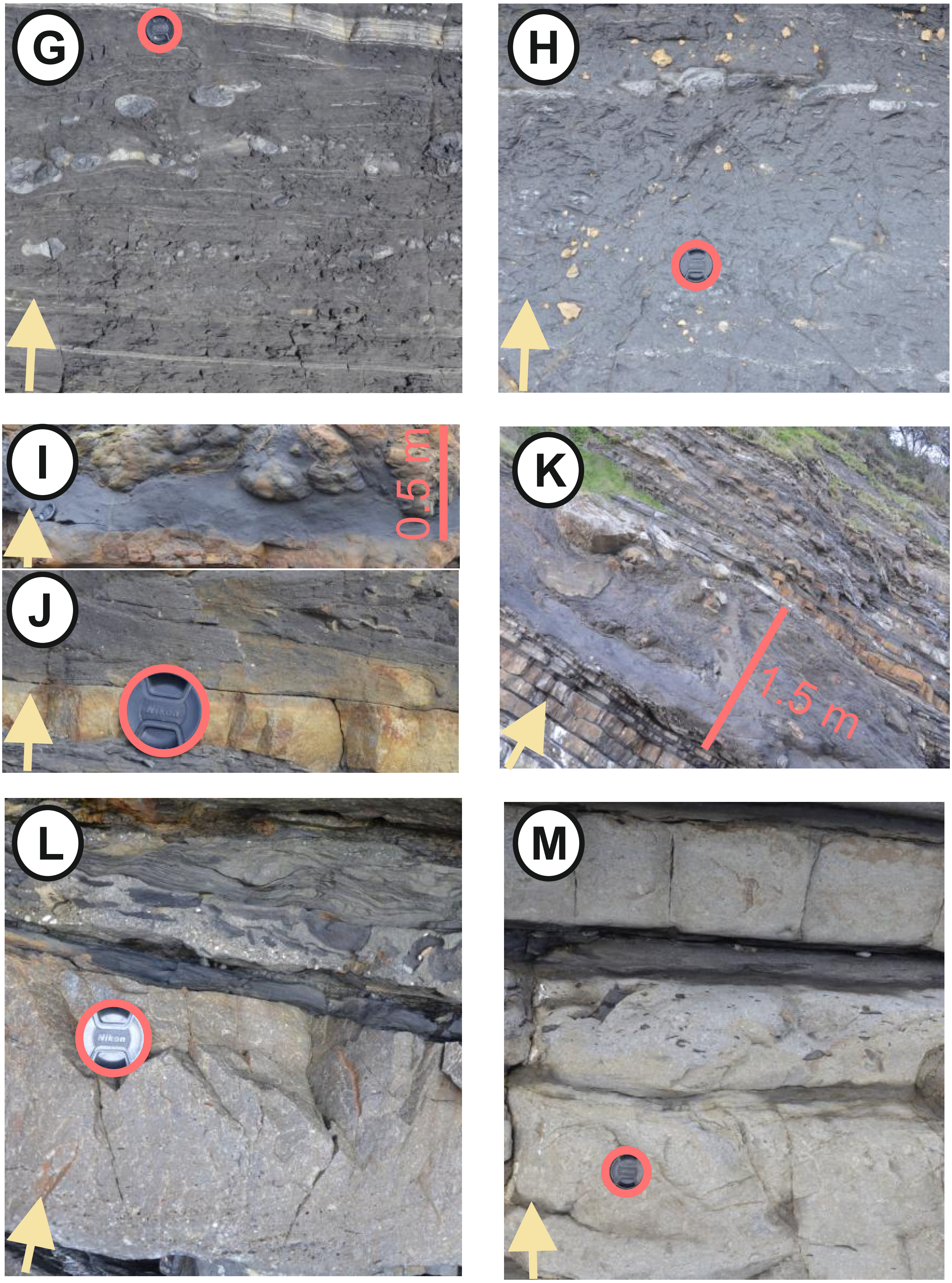

G
H
I
0.5 m
J
K
1.5 m
L
M

Figure

Click here to access/download;Figure;Figure6.pdf

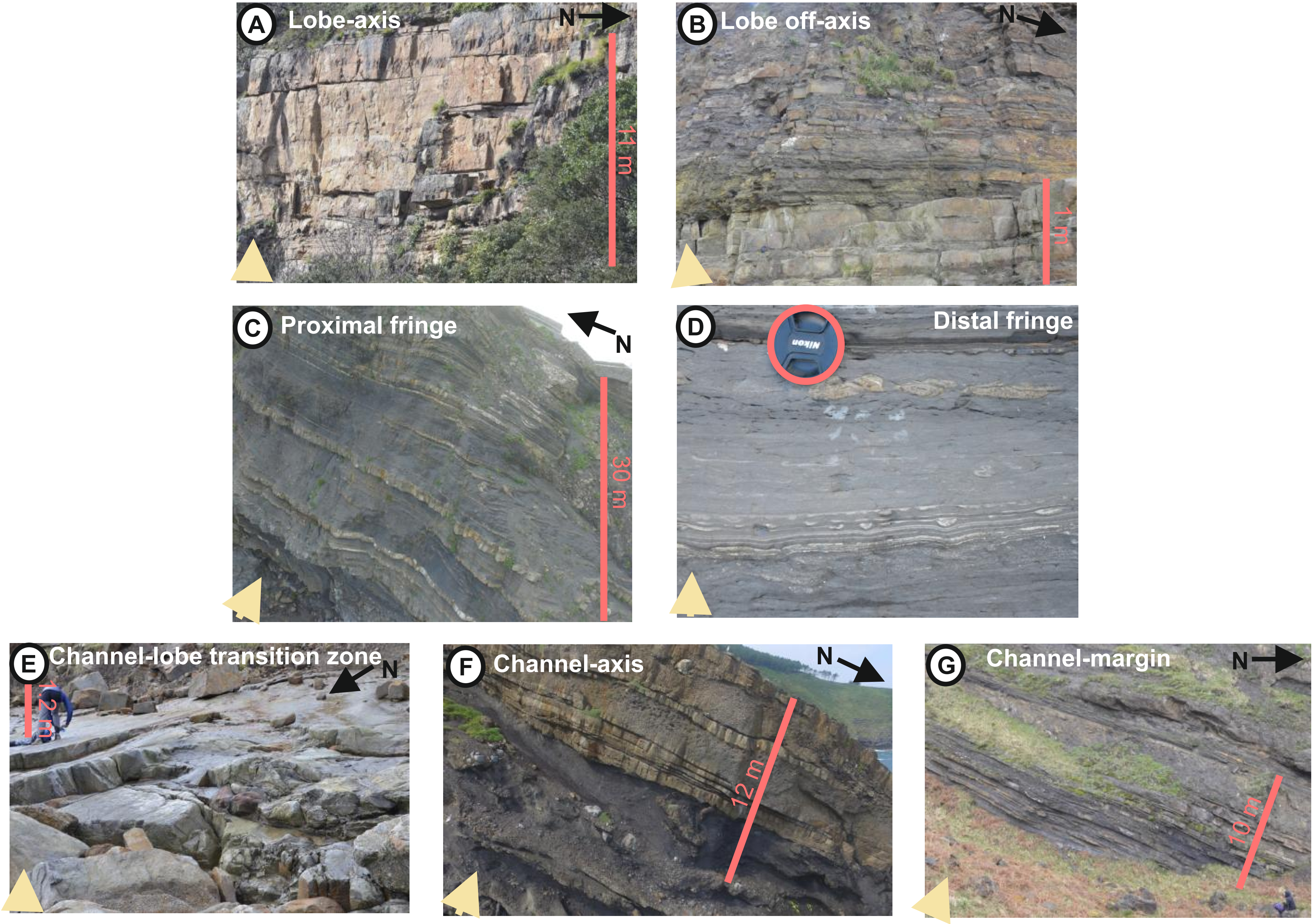

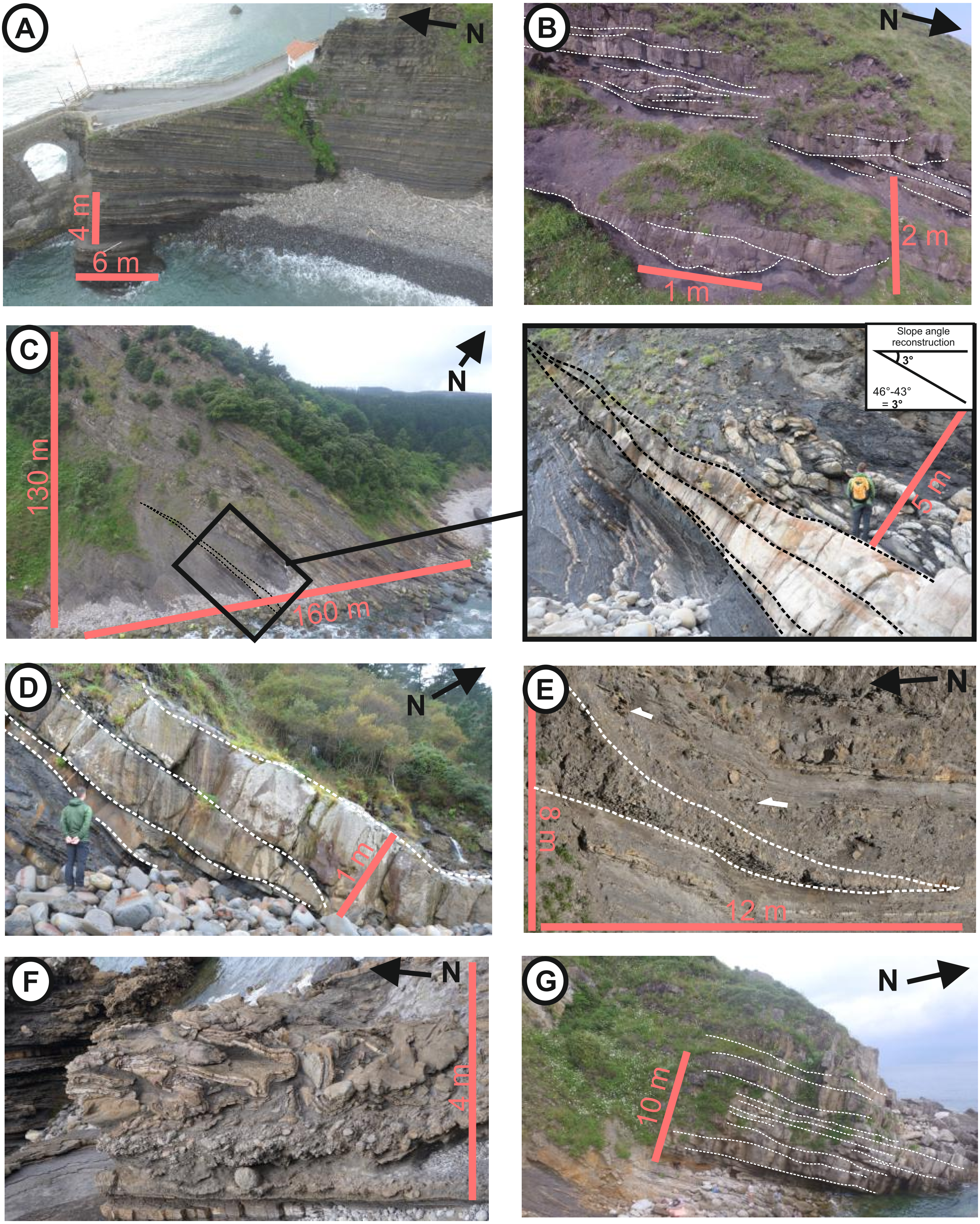
A
N
4 m
6 m
B
N
2 m
1 m
C
N
130 m
160 m
Slope angle reconstruction
3°
46°-43° = 3°
5 m
D
N
1 m
E
N
8 m
12 m
F
N
4 m
G
N
10 m

Figure

Click here to access/download;Figure;Figure8.pdf

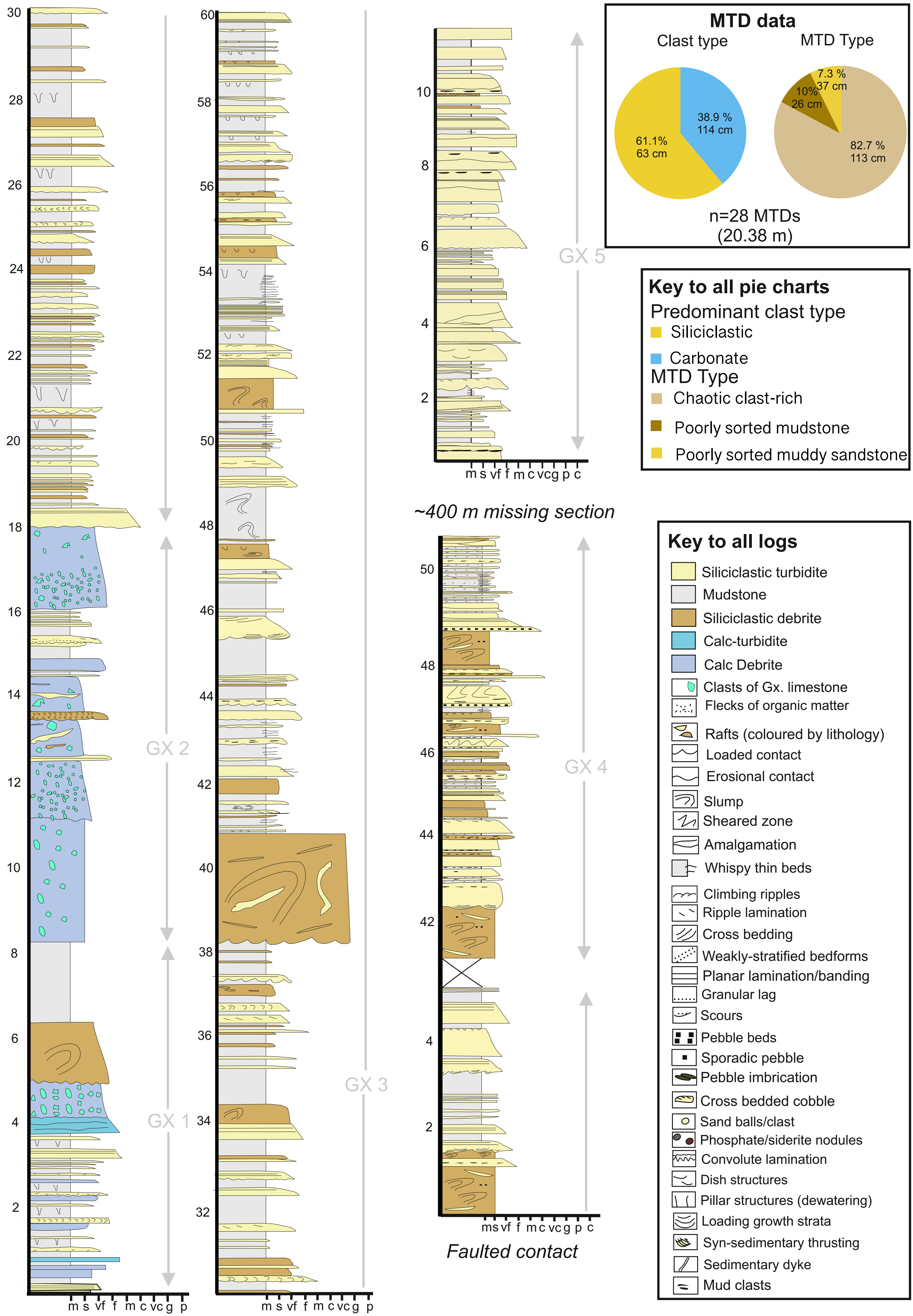

Figure

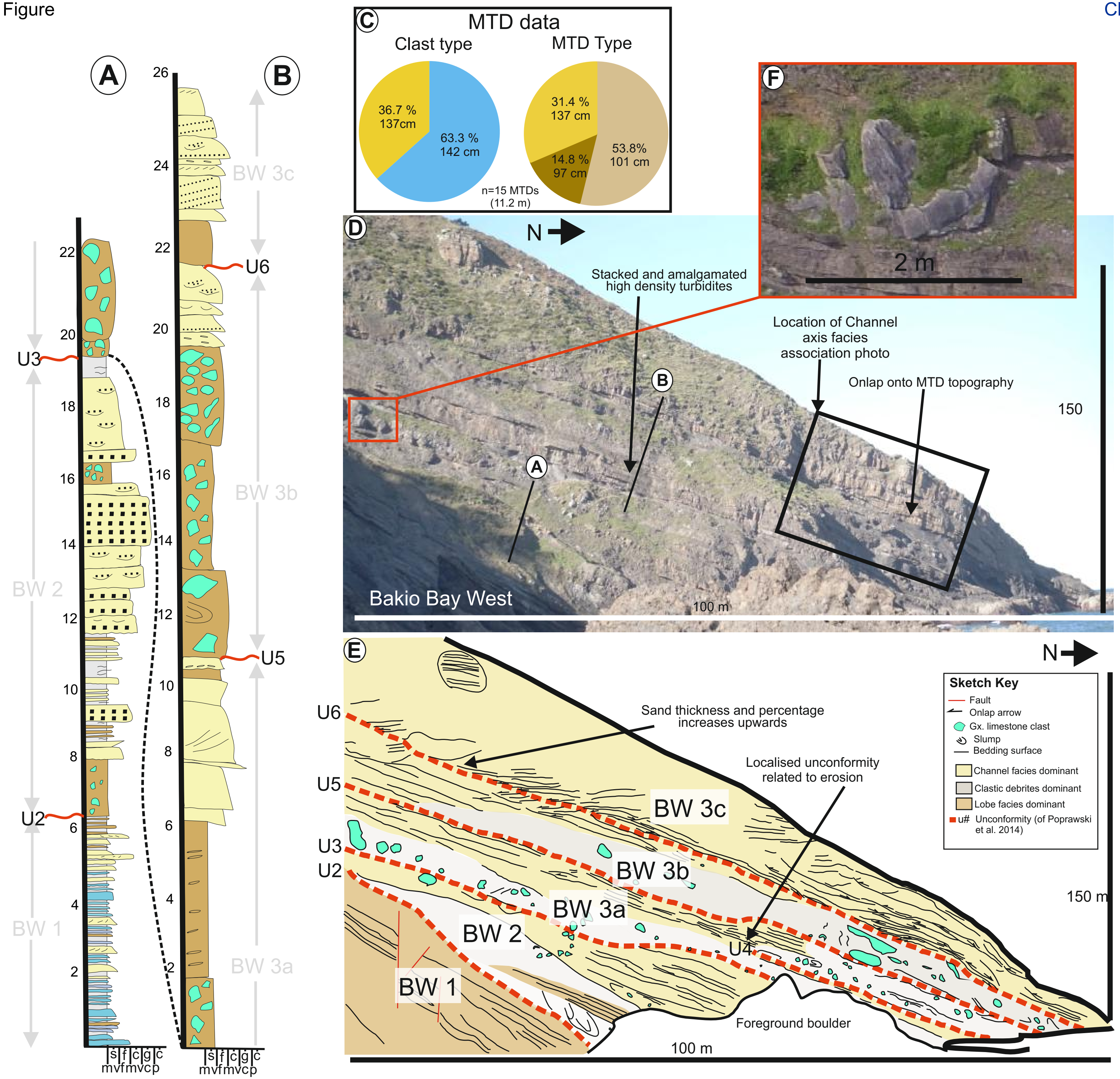
A
B
C
MTD data
Clast type
MTD Type
36.7 % 137cm
63.3 % 142 cm
31.4 % 137 cm
14.8 % 97 cm
53.8% 101 cm
n=15 MTDs (11.2 m)
D
N
Stacked and amalgamated high density turbidites
Location of Channel axis facies association photo
Onlap onto MTD topography
150
Bakio Bay West
100 m
F
2 m
E
Sand thickness and percentage increases upwards
Localised unconformity related to erosion
Foreground boulder
BW 3c
BW 3b
BW 3a
BW 2
BW 1
U6
U5
U4
U3
U2
150 m
Sketch Key
Fault
Onlap arrow
Gx. limestone clast
Slump
Bedding surface
Channel facies dominant
Clastic debrites dominant
Lobe facies dominant
u# Unconformity (of Poprawski et al. 2014)
s f c g c
mvfmvcp

Figure

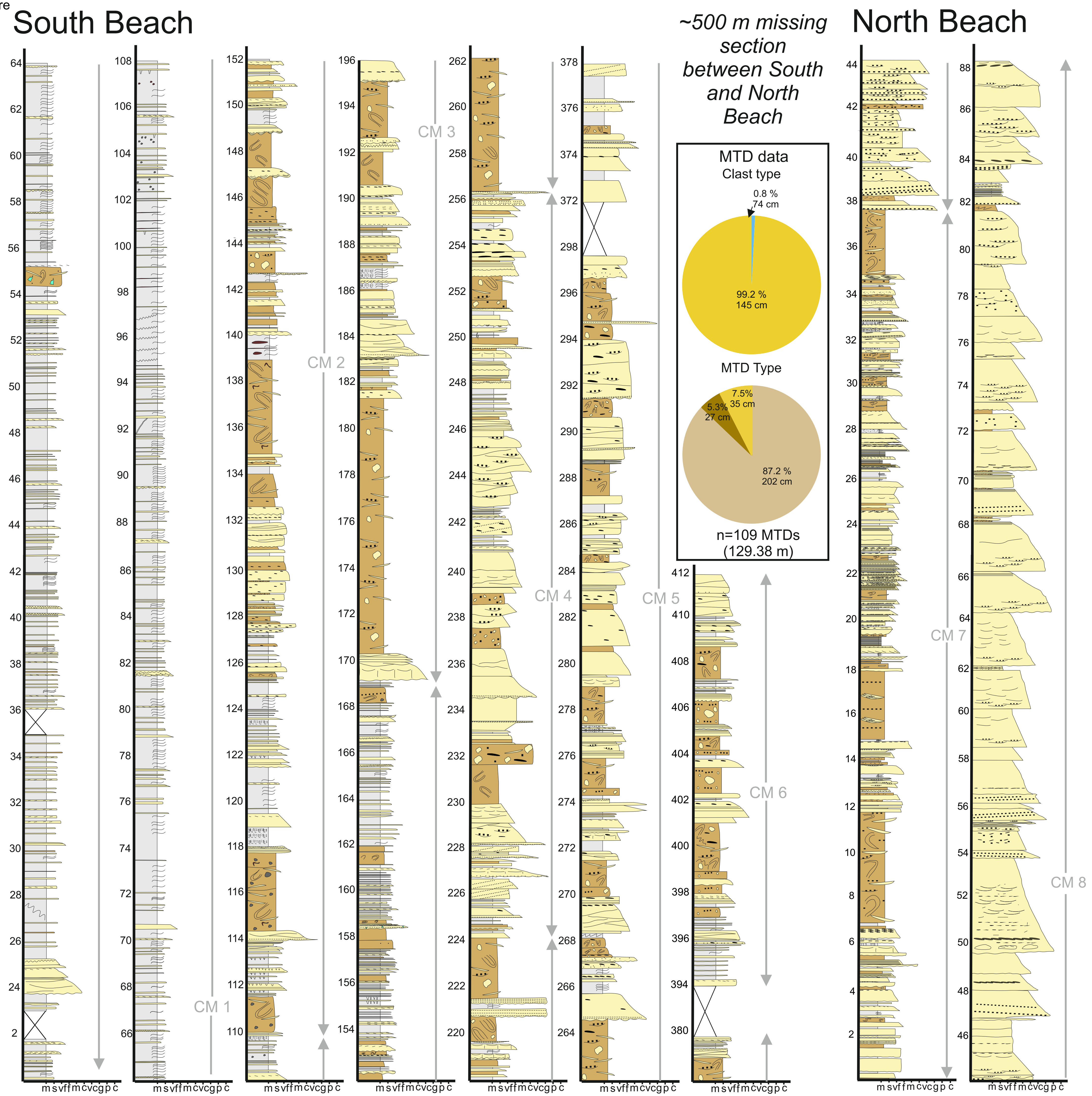

Click here to access/download;Figure;Figure10.pdf

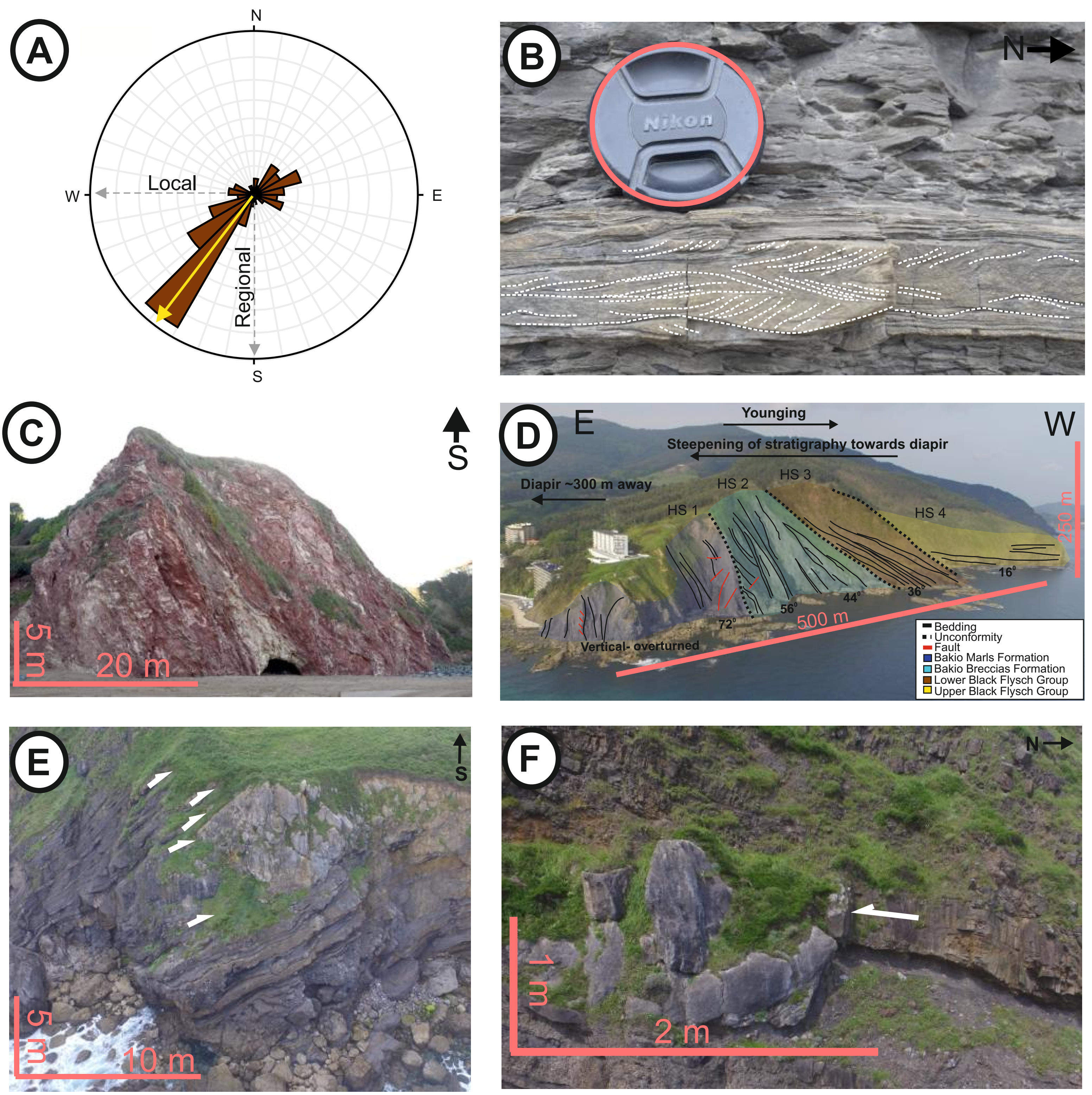
A
N
W
E
S
Local
Regional
B
N
Nikon
C
S
5 m
20 m
D
E
W
Younging
Steepening of stratigraphy towards diapir
Diapir ~300 m away
HS 1
HS 2
HS 3
HS 4
250 m
16°
36°
44°
56°
72°
500 m
Vertical- overturned
Bedding
Unconformity
Fault
Bakio Marls Formation
Bakio Breccias Formation
Lower Black Flysch Group
Upper Black Flysch Group
E
S
5 m
10 m
F
N
1 m
2 m

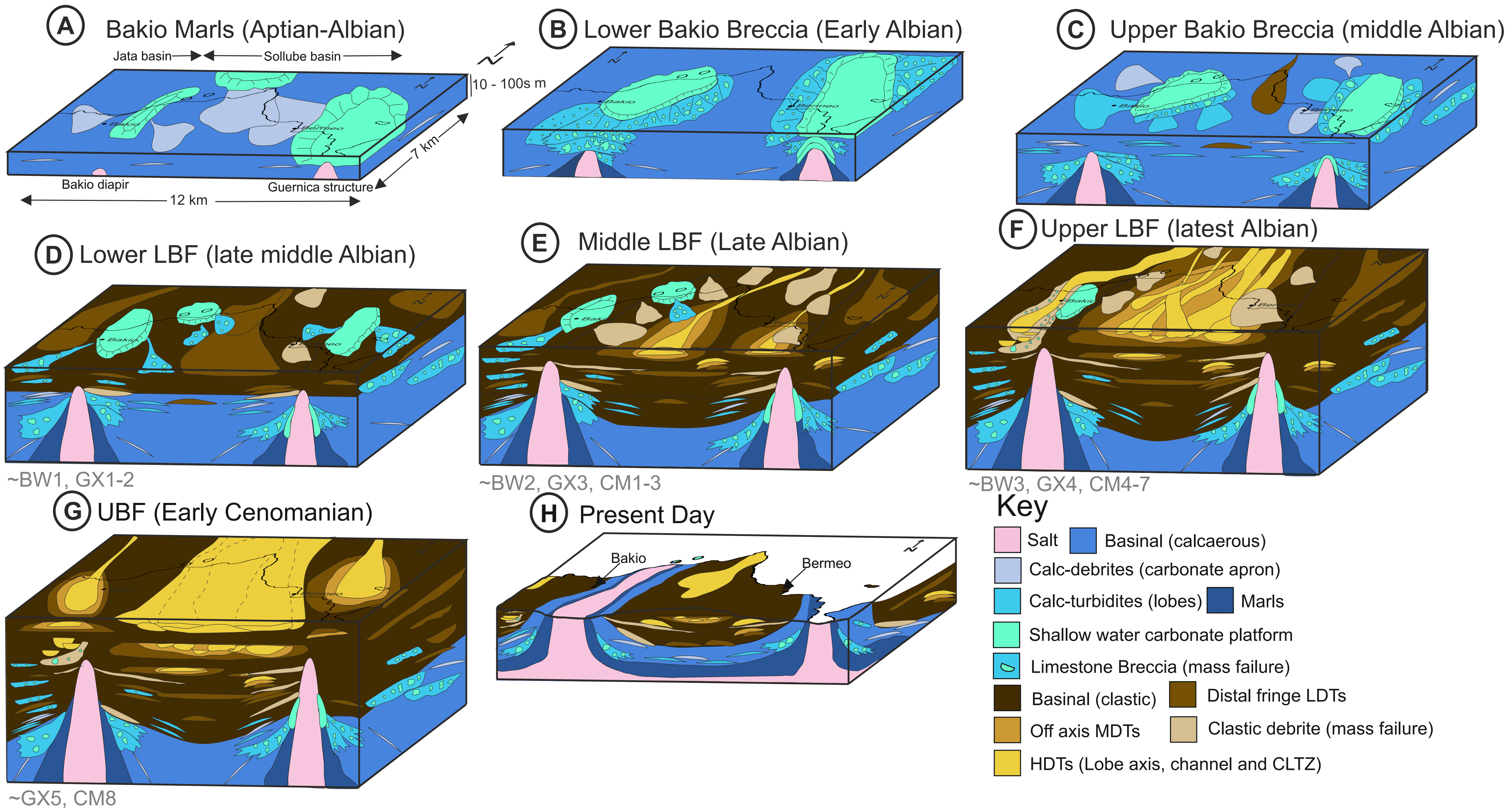
A Bakio Marls (Aptian-Albian)
Jata basin
Sollube basin
10 - 100s m
7 km
Bakio diapir
Guernica structure
12 km
B Lower Bakio Breccia (Early Albian)
C Upper Bakio Breccia (middle Albian)
D Lower LBF (late middle Albian)
~BW1, GX1-2
E Middle LBF (Late Albian)
~BW2, GX3, CM1-3
F Upper LBF (latest Albian)
~BW3, GX4, CM4-7
G UBF (Early Cenomanian)
~GX5, CM8
H Present Day
Bakio
Bermeo
Key
Salt
Basinal (calcaerous)
Calc-debrites (carbonate apron)
Calc-turbidites (lobes)
Marls
Shallow water carbonate platform
Limestone Breccia (mass failure)
Basinal (clastic)
Distal fringe LDTs
Off axis MDTs
Clastic debrite (mass failure)
HDTs (Lobe axis, channel and CLTZ)

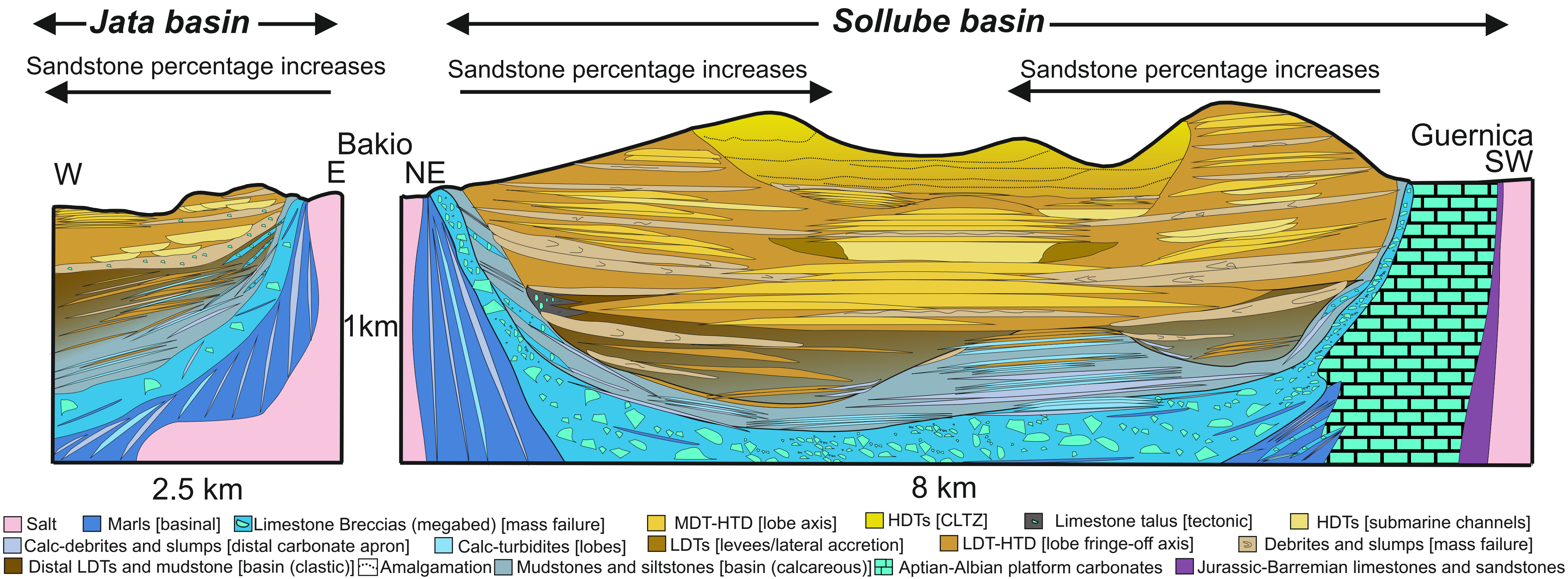

Jata basin
Sandstone percentage increases
Sollube basin
Sandstone percentage increases
Sandstone percentage increases
Bakio
W
E
NE
Guernica
SW
1km
2.5 km
8 km
Salt
Marls [basinal]
Limestone Breccias (megabed) [mass failure]
MDT-HTD [lobe axis]
HDTs [CLTZ]
Limestone talus [tectonic]
HDTs [submarine channels]
Calc-debrites and slumps [distal carbonate apron]
Calc-turbidites [lobes]
LDTs [levees/lateral accretion]
LDT-HTD [lobe fringe-off axis]
Debrites and slumps [mass failure]
Distal LDTs and mudstone [basin (clastic)]
Amalgamation
Mudstones and siltstones [basin (calcareous)]
Aptian-Albian platform carbonates
Jurassic-Barremian limestones and sandstones

Figure

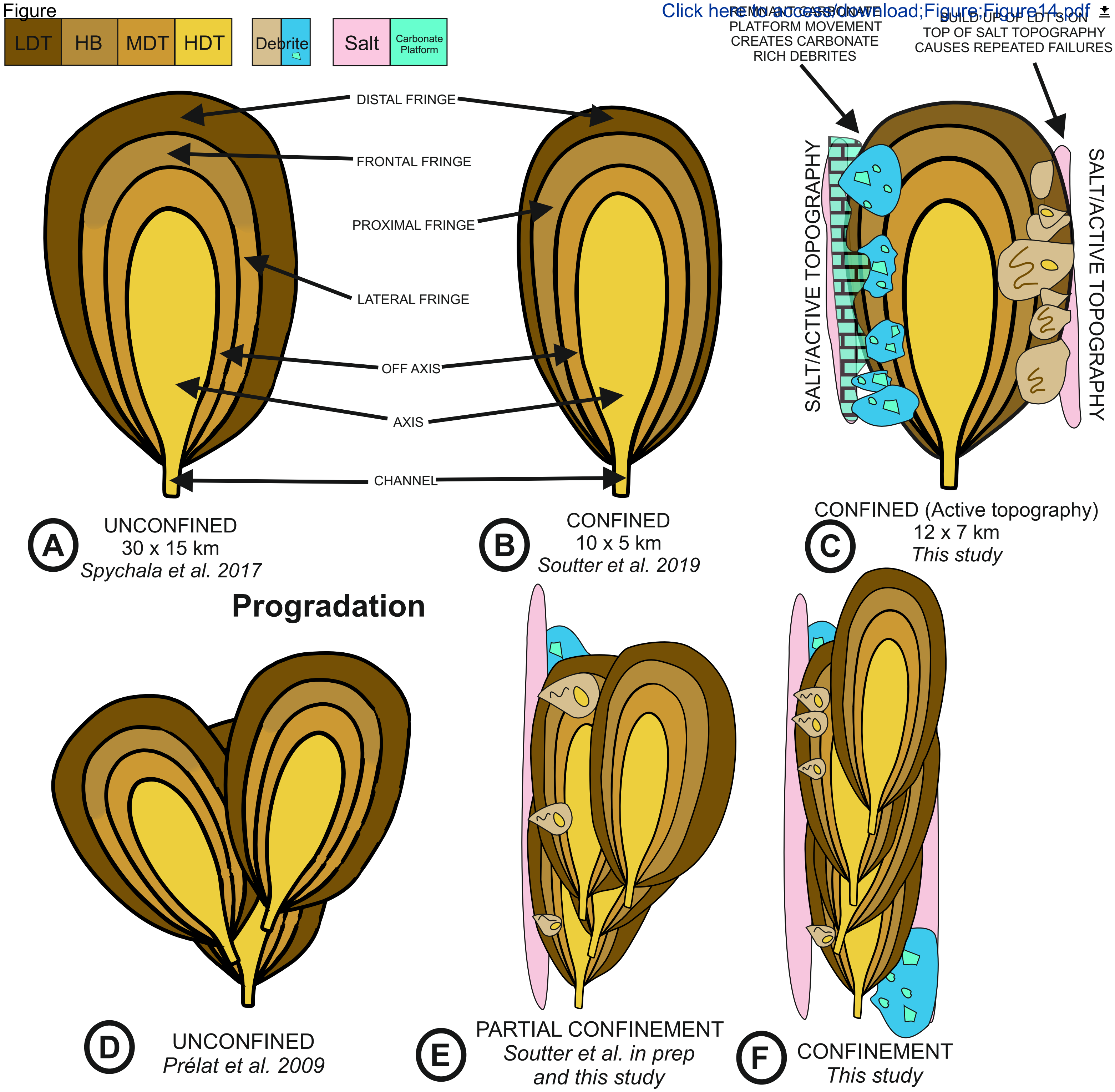
LDT
HB
MDT
HDT
Debrite
Salt
Carbonate Platform
PLATFORM MOVEMENT CREATES CARBONATE RICH DEBRITES
TOP OF SALT TOPOGRAPHY CAUSES REPEATED FAILURES
DISTAL FRINGE
FRONTAL FRINGE
PROXIMAL FRINGE
LATERAL FRINGE
OFF AXIS
AXIS
CHANNEL
SALT/ACTIVE TOPOGRAPHY
SALT/ACTIVE TOPOGRAPHY
A
UNCONFINED
30 x 15 km
Spychala et al. 2017
B
CONFINED
10 x 5 km
Soutter et al. 2019
C
CONFINED (Active topography)
12 x 7 km
This study
Progradation
D
UNCONFINED
Prélat et al. 2009
E
PARTIAL CONFINEMENT
Soutter et al. in prep
and this study
F
CONFINEMENT
This study

Figure

Click here to access/download;Figure;Figure15.pdf

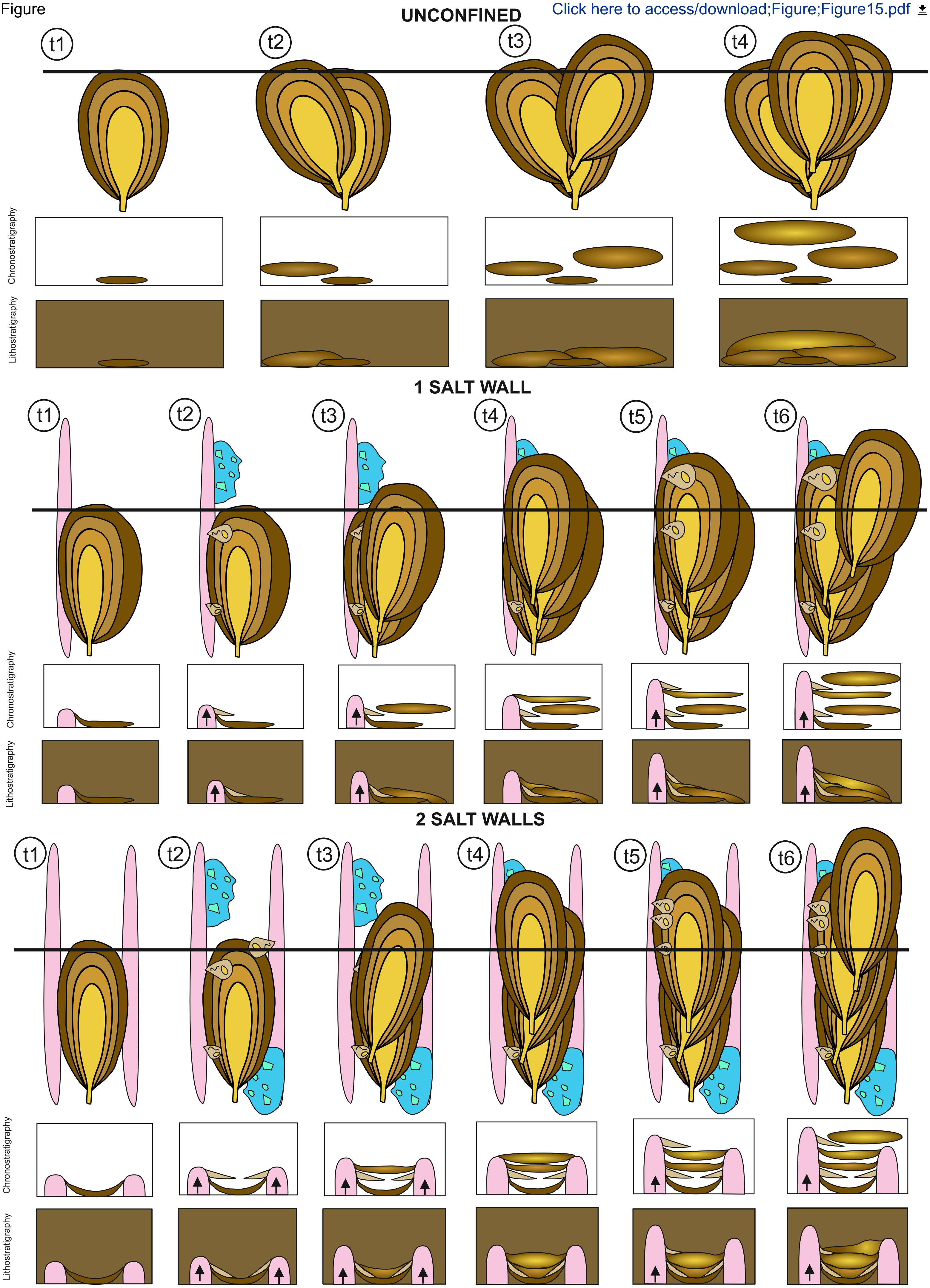

Table 1: Carbonate facies table detailing the major observations of the six facies which comprise the early Albian Bakio Marls and early Middle Albian Bakio Breccias formation. Yellow arrow indicates way up. Peach outline highlights scale, either lens cap (52 mm) or indicated.

Photograph and name	Observations	Interpretations
 **Thin bedded calcareous sandstone**	0.01-0.1 m thick beds of bioclastic (corals and shell fragments) very fine-fine grained sandstones. Commonly normally graded with flat tops and flat bases. Weak planar, ripple and convolute lamination.	**Low-density calciturbidites:** Thin-bedded structured sandstones deposited from dilute turbidity currents.
 **Medium bedded calcareous sandstone**	0.1-0.3 m thick very fine-medium grained normally-graded sandstones, with flat bases and flat tops. Planar, ripple and convolute lamination observed. Mud clasts and intense dewatering also present.	**Medium-high density turbidites:** Presence of tractional structures suggests deposition from a dilute turbidity current. High mud clast percentage could suggest imminent flow transformation (Barker et al. 2008).

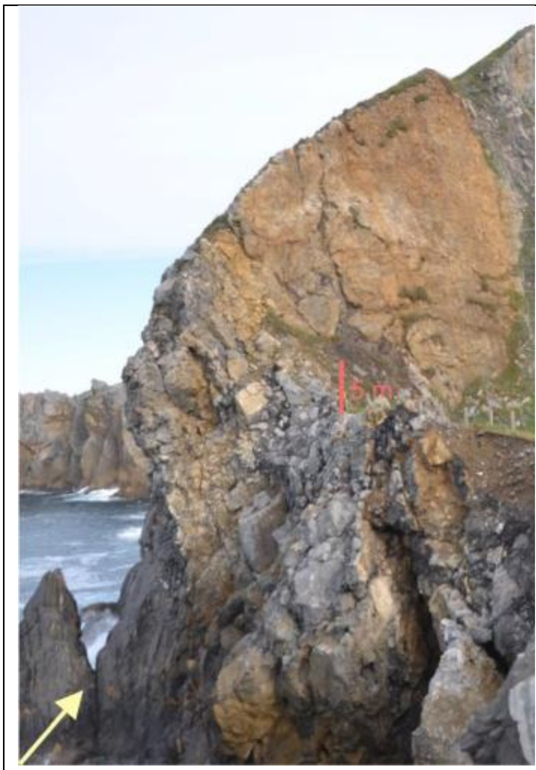 **Limestone breccia**	10+ m thick beds of matrix- or clast- supported limestone breccia, with erosive bases and undulating tops. Poorly-sorted beds consisting of sub-angular – angular limestone mega-clasts, which can be normally-, inversely- or non-graded. Mega-clasts commonly contain entire rudists and fragmented corals.	**Mass transport complex:** Poorly-sorted clasts suggest deposition from 'flow freezing' of a flow with yield strength (Inverson et al. 2010). Limestone clasts are similar in composition to the Gaztelugatxe Limestone, suggesting it is their source (Poprawski et al. 2014; 2016).
 **Fossiliferous poorly-sorted carbonate mudstone**	0.03 – 0.2 m thick poorly-sorted, non-graded carbonate mudstone with fossil fragments. Beds are laterally-discontinuous, with undulose, gradational beds and tops. Cm to dm sized bioclasts of urchins, brachiopods, bryozoans bivalves, corals, crinoid stems and rarer mollusc shell fragments.	**Debris flow:** Fragmented bioclasts, poor-sorting and undulose contacts (Nardin et al. 1979). Fossils are fragmented indicating reworking, but are not lithified indicating direct reworking from an active platform or reef.
 **Clast rich poorly-sorted carbonate mudstone**	0.1 – 1+ m thick poorly-sorted beds with angular limestone clasts within a mud-silt matrix. Clasts can be cm-m scale, generally 1-12 cm, and are rich in mollusc fragments. Rare lithics and organics are observed. Undulose tops reflect clast topography and bases are flat, weakly-erosive or undulose. Weak normal-grading and rarer reverse-grading are observed.	**Carbonate clast-rich debrites:** Poor-sorting and large clast size indicates en-masse deposition from a laminar flow (Nardin et al. 1979; Inverson 1997; Sohn 2000) Weak normal-grading suggests some turbulence was influencing the flow. Clast angularity suggests close proximity to source area. Lack of unconsolidated fossil debris suggests lithification has occurred before reworking into the flow.

 **Remobilised carbonates**	5+ m thick packages consisting of a combination of the above facies that have been slightly remobilised but maintain bedding planes. Contacts are erosive, scalloped or smooth and underlying mudstone units often appear sheared. Convolute lamination and soft sediment deformation are present.	**Slide deposits:** The remobilization, but maintenance of individual bedding planes and sheared basal contacts indicates these are slide deposits. Lack of internal deformation suggest these deposits have been remobilised post lithification, conceivably due to halokinetic movements (Ferrer et al. 2014; Poprawski et al. 2016).

Table 1: Siliciclastic facies table detailing the 10 facies that comprise the Black Flysch Group.

Facies name	Description	Interpretation
Granular-cobbly sandstones	0.1-1.5+ m thick beds of granular-cobble sandstones (Fig. 5A, B), with sub-angular (Fig. 5B) to well-rounded, moderately-sorted clasts. Weak cross-stratification (Fig. 5A), pebble imbrication, amalgamation, mud-clasts and erosional surfaces (Fig. 5A, B) are observed. Dish structuration is pervasive (Fig. 5A).	**High density turbidites:** The coarse grain-size, thick beds and amalgamation surfaces suggest deposition from a highly concentrated turbulent flow, indicating these beds are turbidites. Weak stratification indicates traction carpet deposition (Lowe 1982) suggesting high density turbidites.
Thick-bedded sandstones	0.5 – 1+ m thick beds of very-fine to coarse grained normally-graded sandstones, which lack primary depositional structures and are commonly dewatered (Fig. 5C). Bases can be sharp, erosional, stepped or amalgamated, commonly along a mudstone amalgamation surface with a subtle grain-size break (Fig. 5C), and tops are often flat. Plane parallel laminations, mud-clasts and soft sediment deformation are occasionally observed.	**High density turbidites:** The general massive structuration of these deposits suggests that they represent rapid aggradation beneath a highly concentrated flow (Lowe 1982).
Medium-bedded sandstones	0.1-0.5 m thick beds of very fine-medium grained, normally-graded sandstones. Beds are rich in tractional structures, particularly plane parallel laminations (Fig. 5D). Ripple laminations are observed in bed tops and beds are more frequently structureless towards bases. Bed bases are flat with tool marks or loaded and tops are flat or convolute and often rich in mud-clasts (Fig. 5D). Occasionally amalgamated.	**Medium-density turbidites:** Based on their tractional structures and normal grading, beds of this lithofacies are interpreted as deposition from a dilute turbidity current. These beds are interpreted as medium-density turbidites due to their bed thickness and common lack of structures in the lower part of the bed.
Thin-bedded sandstones	0.01 – 0.1 m thick beds of very fine-fine, normally-graded sandstones. Rich in tractional structures, particularly plane parallel laminations (Fig. 5E, F). Banding on a sub-cm scale (Fig. 5E, F) and convolute lamination are common. Bases are flat (Fig. 5F), undulose, loaded (Fig. 5E, F) or weakly erosive and tops are flat to undulose and rich in mud-clasts. Starved, climbing and opposing palaeoflow ripples are observed (Fig. 5E).	**Low-density turbidites:** Tractional structures and normal grading indicate deposition from a dilute turbidity current and are therefore interpreted as low-density turbidites. Common banding may reflect some periodic suppression of turbulence associated with flow deceleration or increased concentration (Lowe and Guy 2000; Barker et al. 2008). Ripples with opposing palaeoflow suggests topographic interference.
Siltstone and very thin bedded sandstones	Packages of 0.1 m composed of individual fine siltstone to fine sandstone events less than 0.01m. Beds form discontinuous drapes within mudstone (Fig. 5G), with flat bases and flat tops. Parallel and ripple laminations and diagenetic phosphate nodules are observed (Fig. 5G).	**Low-density turbidites:** Fine grain-size and thin bed thickness suggest this unit represents deposition from dilute turbidity currents (Boulesteix et al. 2019), representing lower energy conditions than thin-bedded sandstones.
Mudstone	0.01 -5 m thick mudstone – fine siltstone beds of carbonate or siliciclastic mudstone (Fig. 5H). Weakly planar laminated, friable packages (Fig. 5H) with drapes and discontinuous lenses of siltstone (Fig. 5H). *Nereites* bioturbation and diagenetic	**Background sedimentation:** Fine grain-size indicates low-energy conditions, representative of background sedimentation via suspension fallout. Discontinuous siltstones suggest laminations may be present below the

	spherical cm-scale phosphate nodules present.	scale visible in outcrop, representing deposition from a dilute turbidity current (Boulesteix et al. 2019).
Poorly-sorted mudstone	0.1 – 1+ m thick siltstone- fine sandstone rich mudstones (Fig. 5I). Poorly-sorted, matrix-supported, clast-rich deposit with starry night texture. Granules, organic fragments, mud-clasts and rare shelly fragments present, often with subtle alignment. Bases are flat or undulose, tops flat or loaded (Fig. 5I).	**Mud-rich debrites:** The poorly-sorted matrix and clast-rich nature indicates en masse deposition from a laminar flow (Nardin et al. 1979).
Poorly-sorted muddy sandstone	0.1 -1+ m thick, mud-rich poorly-sorted matrix-supported, fine-medium sandstones with starry night texture (Fig. 5J). Organised mudstone clasts and sporadic granules-pebbles are observed. Flat-undulose tops and flat-graded base are common (Fig. 5J). Rare normal-grading and grain-size segregation and infrequent sheared layers present.	**Sand-rich debrites:** En-masse deposition from a laminar flow (Nardin et al. 1979; Inverson 1997; Sohn 2000). Weak normal-grading suggests some turbulence was influencing the flow and therefore deposition from a transitional flow regime is interpreted (Baas et al. 2009; 2013; Sumner et al. 2013).
Chaotic clast-rich matrix supported deposit	0.5 –3 m thick, poorly-sorted deposit with a poorly-sorted matrix of mudstone-fine sandstone. Clasts include: cm-m scale sandstone balls (Fig. 5K), showing internal lamination and soft sediment deformation, dm – m scale sandstone and heterolithic sub-angular rafts, deformed siderite nodules, limestone clasts, gastropod and sponge fragments, mud- clasts and phosphate nodules. Beds are flat-topped and bases are weakly-loaded (Fig. 5K).	**Mega-debrites:** The poorly-sorted matrix and large clast size are suggestive of 'flow freezing' indicating deposition in a debris flow regime (Inverson et al. 2010). These deposits are interpreted as mega-debrites due to their large clast size (rafts) suggesting they are derived from localised mass failure.
Bi or tri-partite beds	0.1 – 1.5 m thick beds that contain multiple parts (Fig. 5L, M). Typically consisting of a lower fine -medium sandstone (division 1) overlain by a poorly-sorted, muddy siltstone-sandstone (division 2) with a flat-slightly undulose base (Fig. 5L, M). Division 3 is sometimes present, consisting of cleaner siltstone or fine grained sandstone loaded into division 2 (Fig. 5L). Division 1 can contain planar laminations and weak cross-stratification (Fig. 5L) but is often massive with sporadic-slightly organised mud clasts (Fig. 5M). Division 2 is organic-rich, highly deformed and can contain sporadic granules or pebbles (Fig. 5L, M). 'Starry night' texture is observed in this division. Division 3 is more frequently planar laminated than division 1 but can be highly chaotic (Fig. 5L).	**Hybrid-beds:** Tractional structures in division 1 and 3 suggest these deposits formed under turbulent flows. Starry night texture, poor-sorting and mud content suggest that division 2 was deposited under transitional-laminar flow regime (Haughton et al. 2009). Flow transformation from turbiditic to laminar can occur through flow decelerations (Barker et al. 2008; Patacci et al. 2014) or by an increase in concentration of fines during flow run-out (Kane et al. 2017).

Table 1: Facies association table detailing the assemblages that comprise the Black Flysch Group

Facies association name	**Description**	**Interpretation**	**Architecture (Table 4; Fig. 7)**
Lobe-axis	Dominantly thick-bedded sandstones (Fig. 6, 7C) with sub-ordinate medium-bedded (Fig. 5D), thin-bedded (Fig. 5E, F) and granular-cobbly sandstones (Fig. 6). Beds are often massive and amalgamated (Fig. 6) with pervasive dewatering, frequent mud-clasts and subtle normal grading (Fig. 5C). Thin-bedded granular-cobbly sandstones can underlie thick-bedded sandstones or form isolated lenticular geometries (Fig. 5B).	Thick-bedded nature suggests deposition from high concentration turbidity currents with relatively high rates of aggradation preventing the development of tractional sedimentary structures (Kneller and Bramney 1995; Talling et al. 2012). Common amalgamation, and entrainment of mudstones clasts in thick-bedded sandstones, indicates that the parent flows were highly energetic and capable of eroding, entraining, and bypassing sediment during the passage of flow (Lowe 1982; Mutti 1992; Stevenson et al. 2015). Similar deposits elsewhere have been interpreted as lobe-axis deposition (Walker 1978; Prélat et al. 2009; Kane et al. 2017). Thin-bedded granular-cobbly sandstones are associated with overlying and adjacent amalgamated thick-bedded sandstones and are thought to represent a mostly bypassing equivalent of the depositional thick-bedded sandstones within the lobe axes (Kane et al. 2009).	Pinching out upslope (Fig. 7C) or convex up (Fig. 6)
Lobe off-axis	Primarily composed of normally-graded structured to structureless medium-bedded sandstones (Fig. 5D) with less common thin-bedded (Fig. 5F) and thick-bedded sandstones (Fig. 5C). Ripples at the top of beds commonly show opposing palaeoflow directions from those that are measured from flutes and grooves on bed bases. Mudstones, poorly-sorted mudstones, sand-rich mudstones and rarer chaotic clast-rich matrix supported deposits are periodically or randomly interspersed in this facies association (Fig. 6).	A medium-density turbidite interpretation is given for these units based on the preservation of both structured and structureless sandstones. Similar preservation of both deposit types has been interpreted as off-axis lobe environments, deposited by decelerating turbidity currents (Prélat et al. 2009; Spychala et al. 2017; Soutter et al. 2019). Opposing palaeocurrent directions within event beds is characteristic of topographically influenced flows (Kneller et al. 1991; Bakke et al. 2013). Periodic deposition of mudstones suggest episodic system shut down. Poorly-sorted mudstones, sand-rich mudstones and chaotic clast-rich matrix supported deposit occurrence, indicate periodic laminar flows which could indicate nearby active topography (Kneller et al. 1991; Mayall et al. 2010).	Pinching out upslope (Fig. 7C) or convex up (Fig. 6)
Proximal fringe	Consists primarily of thin-bedded sandstones (Fig. 5 E, F) and bi or tri-partite event beds (Fig. 5L, M). Siltstone and very-thin bedded sandstones and medium-bedded	Thin-bedded, structured sandstones are interpreted to be deposited from low-concentration turbidity currents (Mutti 1992; Jobe et al. 2012, Talling et al. 2012). Bi- and tri-partite	Tabular (Fig. 7A) or pinching out up slope (Fig.7C).

	sandstones (Fig. 6) are infrequently observed. Poorly-sorted mudstones, sand-rich mudstones and rarer chaotic clast-rich matrix supported deposits are periodically or randomly interspersed within the otherwise organised thin-bedded sandstones and bi or tri-partite beds (Fig. 6).	event beds are interpreted as hybrid beds (Haughton et al. 2009). The transformation of flows within hybrid beds observed here document a change in flow process from high-medium concentration turbulent to laminar or transitional, to low-concentration turbulent (Remacha et al. 2005; Baas et al. 2011). Thin-bedded sandstones and hybrid beds underlie lobe and lobe axis facies associations and are therefore interpreted to be deposited adjacent to such deposits. Abundant hybrid beds and thin-beds indicate lobe fringe deposition elsewhere (Hodgson 2009; Jackson et al. 2009; Kane et al. 2017; Soutter et al. 2019), specifically within the proximal fringe (Sypchala et al. 2017). In tectonically confined settings, flow types are highly variable and the frontal and lateral fringe can be difficult to decipher because flow transformation is influenced by topography so hybrid beds can be common in the lateral and frontal fringe (Barker et al. 2008; Soutter et al. 2019) termed 'proximal fringe'.	
Distal fringe	Dominated by siltstone and very-thin bedded sandstones (Fig. 5G) and mudstones (Fig. 5H) with secondary thin-bedded sandstones, bi and tri-partite beds and thin-bedded poorly-sorted mudstones (Fig. 6). Mudstones separating individual events are often slightly deformed or sheared and show drapes of non-continuous siltstone (Fig. 6).	The fine grain-size, thin-bedded character and low stratigraphic position of these beds is consistent with lobe fringe deposition. The relative lack of hybrid beds within this facies association support a distal lobe fringe interpretation (Hodgson 2009; Jackson et al. 2009; Kane et al. 2017; Soutter et al. 2019), specifically within the proximal fringe (Sypchala et al. 2017).	Tabular (Fig. 7A)
Channel-lobe transition zone	Consists of granular-cobbly sandstones (Fig. 5A) and intensely dewatered thick-bedded sandstones up to 5 m thick (Fig. 5C). Erosional bases, mega-flutes, stepped amalgamation surfaces and mud-clast abundance are common (Fig. 6). Granular-cobbly sandstone lenses infilling lensoid, spoon-shaped, depressions are observed (Fig. 6). Weakly stratified cross-lamination of gravels within sandstone matrix and pebble imbrication is also observed (Fig. 5A, 8). Low-wavelength hummock-like structures are observed (Fig. 6) (Vincente Bravo and Robles 1991).	Erosional based geobodies infilled with coarser clasts indicate active erosion and deposition. Common amalgamation, and entrainment of mudstones clasts in thick-bedded sandstones, indicates that the parent flows were highly energetic and capable of eroding, entraining, and bypassing sediment during the passage of flow (Lowe 1982; Mutti 1992; Stevenson et al. 2015), while weak cross-stratification, slight grading and pebble imbrication are more typical of depositional conditions (Mutti and Normark 1987). This juxtaposition of depositional and erosional elements has been observed elsewhere in channel-lobe transition zones (Mutti and Normark 1987; Wynn et al. 2002; Pemberton et al. 2016; Brooks et al. 2018). The presence of cross-stratified gravels supports the facies association proposed by previous work (Vincete Bravo and Robles 1991; 1995).	Tabular amalgamated beds (Fig. 7G)

Channel-axis	Thick-bedded sandstones (Fig. 5C), granular-cobbly sandstones (Fig. 5A), poorly-sorted muddy sandstones (Fig. 5I) and chaotic clast-rich matrix supported deposits (Fig. 5K). Thick-bedded sandstones typically gradationally overlie granular-cobbly sandstones, which are commonly grooved on the base, showing normal grading (Fig. 6). These successions are erosional into the underlying poorly-sorted muddy sandstones or chaotic clast-rich matrix supported deposits, which exhibit some deformation and shearing (Fig. 6). Sandstone beds either erode into each other, are amalgamated or less commonly are separated by thin beds of mudstone (Fig. 6). Low-angle cross-stratification is observed (Fig. 5A). The sandy mudstones and chaotic units contain sub-angular -angular poorly-sorted clasts of up to boulder size. The composition of these clasts include limestone fragments, organics, siliciclastic fragments, slumped and reworked thin-bedded heterolithics, clasts of granite, deformed and reworked siderite, mud clasts and fossil fragments (Fig. 6).	Common amalgamation, erosion and entrainment of clasts within the sandstones indicate that the parent flows were highly energetic and capable of eroding, entraining and bypassing sediment (Mutti 1992; Stevenson et al. 2015; Soutter et al. 2019). The coarse grain-size and basal location of granular-cobbly sandstones suggests these beds were deposited as a coarse-grained lag in a bypass dominated regime (Hubbard et al. 2014). Erosional-based lenticular sandstones and their grading from cobbly – fine sandstone is consistent with deposition in a submarine channel described elsewhere (Hubbard et al. 2008; Romans et al. 2011; McArthur et al. 2020). Weak low angle lamination within sandstone beds could indicate lateral accretion (Kane et al. 2010; Jobe et al. 2016). Poorly-sorted muddy sandstones and chaotic units could represent channel collapse and margin failure (Flint and Hodgson, 2005; Pringle et al. 2010; Jobe et al. 2017). The wide variation in clast composition, more diverse than that observed in any other facies association, indicates broader catchment area for these debris flows, which may indicate an extra-basinal provenance (Stevenson et al. 2015; Di Celma et al. 2016).	Concave upward (Fig. 6, 7B)
Channel-margin	Thin-bedded sandstones (Fig. 5E, F) and poorly-sorted mudstones with secondary medium-bedded sandstones and chaotic clast-rich matrix supported deposits (Fig. 6). Thin and medium bedded sandstones are planar and ripple laminated (Fig. 5E). Poorly-sorted mudstones and chaotic clast-rich matrix supported deposits include angular –rounded clasts of limestone, siliciclastic fragments and mud-clasts. Medium-bedded sandstones erode into the tops of chaotic clast-rich matrix-supported deposits and thin- bedded sandstone show loaded, flat and weakly erosive bases. This facies association appears beneath the channel-axis facies associations (Fig. 6).	The supercritical bedforms and thin-bedded nature of these deposits is similar to those described as channel-margin facies by others (Kane and Hogdson 2011; Hodgson et al. 2011; Hubbard et al. 2014; Jobe et al. 2017; McArthur et al. 2020). The location of this facies association beneath channel-axis deposits, suggests that they were deposited adjacent to them indicates they represent channel-margin facies association.	Tabular (Fig. 6, 7A)

Table 1: Table describing geometrical configurations observed within the Black Flysch Group

Architecture name	Description	Interpretation	Facies association (Table 3; Fig. 6)
Tabular bedded	A package of stacked beds which show a continuous thickness laterally for 10s – 100s m, occasionally with some subtle thickness changes (Fig. 7A). Post depositional faulting, tectonic and halokinetic tilt prevent these geometries from being traced on a 100s m-km-scale. Common in thin-bedded (Fig. 7A) and medium-bedded sandstones (Fig. 5D). Tabular geometries are observed >500 m away from diapiric influence.	This continuous, stacked geometry suggests constant, depositional energy. Tabular architectures appear to be uninfluenced by topography, and are similar to unconfined settings (Prélat et al. 2009). Low density turbidites are less affected by topography than more cohesive flows (Al-Ja'aidi 2000; Bakke et al. 2013) and therefore can run-up topography for greater distances, without becoming ponded.	Distal fringe (Fig. 6), proximal fringe (Fig. 7A), channel margin (Fig. 6).
Concave upward	Curvilinear geobodies with variable thickness that are concave upward, consisting of a centroid and two margins, which the centroid thins towards, sometimes by up to 80%. (Fig. 7B). Granular sandstones are present in the centroid of the geobody, often overlain by high-density turbidites, which become thinner-bedded towards the margins. The thickness of these geobodies is typically decimetre to metre scale and thickness to width ratios can range between 1:10 and 1:50. The geobodies commonly erode and amalgamate with each other, and stack above the previous deposit.	Each geobody represents at least one event, the coarse-grained basal lag could represent a bypass event before the high density turbulent flow which filled the geometry. These multipart geobodies, which are attributed to deep-water channels based on their geometries stack on top of and erode into each other, suggesting increasing confinement (Mayall et al. 2010).	Channel axis (Fig. 6, 7B)
Pinching out upslope	Elements that change in thickness, but only in one direction (Fig. 7C). Commonly these geometries are amalgamated, with individual events displaying a convex up geometry. Thinning rate is approximately 10cm/m in Fig. 7C.	Thinning of deposits indicates flow deceleration related to topography, which ultimately lowers flow concentration (Baas et al. 2011; Teles et al. 2016). The eventual pinch out of the sandstone is due to the flows inability to run up the entirety of the topography.	Proximal fringe (Fig. 6, Fig. 7C), lobe off-axis, lobe axis (Figure 7C).
Convex up	Packages are generally continuous in thicknesses on the scale of the outcrop, with beds thinning slightly to either side (Fig. 7E). The centroid is typically decimetre-metre thick. The upper surface of each deposit is commonly undulose with an overall, often subtle, convex-upward geometry (Fig. 7E). High-density turbidites dominate these architectures and are commonly stacked or amalgamated.	The upwards curvature and slight thinning of this geometry lead to their interpretation as lobate geometries (Prélat et al. 2009; Hodgson 2009; Sypchala et al. 2017). Shifting of the centroid of the lobe axis indicates compensational stacking is influencing these deposits similar to that observed in unconfined settings (Prélat et al. 2009; Spychala et al. 2017).	Lobe off-axis (Fig. 6), Lobe axis (Fig. 5C, Fig. 6).
Pinching out downslope	Packages are triangular in geometry and pinch out gradually. These architectures are very common at Gaztelugatxe Island (Fig. 3) where they consist of limestone breccia (Table 1) and have thinning rates of 6.7 – 10 cm/ m downslope (Fig. 7E).	These deposits are interpreted as talus deposits, common around diapiric highs (Giles and Lawton 2002; Giles and Rowan 2012) and on fault scarps (Poprawski et al. 2014; 2016). The similarity in facies and geometry to 'carbonate	Limestone breccia (Table 1).

	Towards the top of Gaztelugatxe Island (closer to the contact with Gaztelugatxe Limestone) these architectures are amalgamated, whilst further away from the limestone they are interspersed within tabular architectures. Successive thin-bedded, tabular deposits appear to onlap onto the topography formed by these downslope thinning geobodies (Fig. 7E).	lentils' described elsewhere (McBride et al. 1974; Hunnicutt 1998; Kernen et al. 2012; 2018) and the likely close proximity to the offshore Bakio diapir (Poprawski et al. 2016) suggest these geometries are halokinetically driven. The source of this talus is interpreted to be the Gaztelugatxe Limestone due to its proximity and geometrical relationships. Onlap of successive deposits suggest diapiric collapse was coeval with deep marine deposition.	
Undulose	Packages have an undulose, heterogeneous geometry (Fig. 7F). Individual beds vary in thickness and facies, and include thin-beds, chaotic mud-rich debrites and limestone breccias (Fig. 7F), but overall architecture maintains a broadly consistent thickness. The base of these architectures can be composed of limestone breccias (Fig. 7F, Table 1).	These remobilized units represent slump deposits. Ranging palaeoflow directions, and both carbonate and siliciclastic inclusions, suggest they are derived from the diapir roof and flanks (Poprawski et al. 2014). The undulose geometries could overlie carbonate 'lentils' or may reflect the reworking of 'lentils' within these deposits (Fig. 7F).	Mass failure deposits; limestone breccia (Table 1), chaotic debrites (Fig. 5J, K), remobilised proximal-distal fringe (Fig. 7F).
Tabular amalgamated beds	Packages appear tabular and consist of beds which remain relatively consistent in thickness, with minor deviations related to previous topography (Fig. 7G). This architecture is primarily composed of the channel-lobe transition zone facies association (Fig. 6). Concave depressions, which are spoon-shaped and metre scale in width can be seen on bed tops and bed bases and are associated with undulations at bed-scale (Fig. 7G). Overall the geometry is slightly concave up, with the centre of each deposit thinning slightly on either side at the scale of the outcrop (Fig. 7G).	The dominance of channel lobe transition zone facies associations leads to an interpretation of a stacked, scoured, broad channel-lobe transition zone where erosional and depositional processes were active (Vicente Bravo and Robles 1991; Robles et al. 1995; Brooks et al. 2018). Spoon-shaped depressions are representative of mega flutes and scours (Robles et al. 1995). These cause a variable depositional topography which influenced subsequent flows, resulting in slight compensational stacking.	Channel lobe transition zone (Fig. 5A, 6)